Temperature Uniformity Measurements and Studies of Bunch Parameter Variations for the Advanced Wakefield Experiment, AWAKE

by

Nicolas Savard
B.Sc., McGill University, 2014

A Thesis Submitted in Partial Fulfillment of the
Requirements for the Degree of

MASTER OF SCIENCE

in the Department of Physics and Astronomy

Temperature Uniformity Measurements and Studies of Bunch Parameter Variations for the Advanced Wakefield Experiment, AWAKE

by

Nicolas Savard
B.Sc., McGill University, 2014

Supervisory Committee

Dr. Dean Karlen, Supervisor
(Department of Physics and Astronomy)

Dr. Lia Merminga, Supervisor
(Department of Physics and Astronomy)

Supervisory Committee

Dr. Dean Karlen, Supervisor
(Department of Physics and Astronomy)

Dr. Lia Merminga, Supervisor
(Department of Physics and Astronomy)

ABSTRACT

The Advanced Wakefield Experiment, or AWAKE, is an experiment based at CERN (European Organization for Nuclear Research) whose purpose is to demonstrate the acceleration of electrons using plasma wakefields driven by a charged particle bunch. As a proof-of-principle experiment, AWAKE will be propagating a high-energy proton bunch through 10 meters of plasma to drive the wakefields for electron acceleration. To accelerate the electrons, we want to inject them into regions of both focusing and acceleration within these wakefields behind the proton bunch. In order for the electrons to stay within this optimal accelerating/focusing region, we need to maintain uniform plasma density within 0.2%, and we need to inject when the wakefield phase-velocity is constant. To preserve uniform plasma density, we use a liquid heat-exchanging pipe which can maintain stable temperatures, and therefore uniform rubidium vapor/plasma densities, to within 0.2%. We show that this is possible using Galden HT270 as a heat-exchanging liquid. We also show that additional components required for this system will need external heating to prevent heat-loss, and therefore temperature non-uniformity. Furthermore, using the PIC simulation OSIRIS, we study how changing size parameters of the initial proton bunch by $\pm 5\%$ affects the phase-velocity of the wakefield. It is seen that these parameter variations will not significantly affect the optimal region size and energy gain of injected electrons; so long as the electrons are injected at regions of ξ near σ_{zb} of the proton bunch and after 4 m of bunch propagation length in the plasma.

List of Acronyms

AWAKE (Advanced Wakefield Experiment) Plasma-wakefield experiment described within this thesis.

CERN (European Laboratory for Particle Physics) Research Laboratory in Geneva, Switzerland.

MPP (Max-Planck Institute for Physics) Research Laboratory in Munich, Germany.

PIC (Particle-in-Cell) Simulation technique for many-particle systems.

PID (Proportional-Integral-Derivative) Control loop feedback mechanism.

Rb (Rubidium) Type of alkali metal.

RF (Radio-Frequency) Commonly used electromagnetic frequency.

SLAC (Stanford Linear Accelerator) US National Laboratory operated by Stanford University.

SPS (Super Proton Synchrotron) Proton bunch accelerator at CERN.

SMI (Self-Modulation Instability) Modulation of particle bunch within a plasma.

WDL (Wright Design Ltd) Engineering company based in Cambridge, UK.

Contents

List of Tables

List of Figures

ACKNOWLEDGEMENTS

Firstly, I would like to thank my UVic supervisors; for without them I would never have been able to even start working towards a Master. Dean Karlen was the first professor who offered to become my supervisor at the University of Victoria. Over these past two years, he has been enormously helpful with making sure I do everything required to eventually get a Master of Science. Thanks also to my other supervisor Lia Merminga, who was the first to get me involved with the AWAKE project when I was at TRIUMF. It is because of her that I got the chance to be able to eventually make my way to Munich to work on the project directly. I would also like to mention Victor Verzilov, a supervisor I had at TRIUMF who is also a member of the AWAKE collaboration. He has offered support and advice whenever I needed it, and that has been appreciated.

While at the Max-Planck Institute for Physics, my mentor was Patric Muggli, the rare type of person who can explain advanced physical concepts in visually simple ways. He was my main motivator, and was actively involved in all my projects. He always made sure that I understood my work and would always question everything I did to make sure of it. He believes in my capabilities as a scientist even when I have doubts, and has a great sense of humor, which certainly made my time at MPP more enjoyable. For these reasons, I would like to thank him.

When working on the temperature measurements, I was helped often by Erdem Oz, Fabian Batsch, and Daniel Eaton of WDL. While working with OSIRIS, I was given support by Jorge Viera. He gave me the initial input deck for the simulation, and answered my (many) emails concerning these simulations. Thanks to these smart people for all their help.

Thanks to the University of Victoria and TRIUMF for providing funding. These institutions, along with the Max-Planck Institute for Physics, also offered valuable experience during my studies.

And finally, thanks to my parents, Guy and Carole, who offer encouragement not just in my work, but in making sure that I am happy. They will always support me, and I understand how lucky I am to have that. And thanks to my younger siblings Claire, Lea, and Emile, who never hesitate to send their love while I'm away; and their brother appreciates that more than they could possibly know.

Don't cry because it's over, smile because it happened.

Dr. Suess

DEDICATION

To the advancement of science and technology. I hope this small contribution will in some way have a positive impact on the future.

Chapter 1

Introduction

1.1 Electron Acceleration

The world's largest particle accelerator is the Large-Hadron-Collider (LHC), which can collide protons up to TeV energies in order to study the fundamental laws of particle physics. Physicists want to further probe these high-energy collisions with lepton-lepton colliders in the future. Due to the high energy loss of charged leptons (such as electrons) in circular accelerators, we currently require the use of linear accelerators to accelerate leptons to high-energies.

Modern linear accelerators are composed of metallic cavities with coupled RF (radio-frequency) electric fields. The electric fields within the cavities are used to 'push' the electrons to higher velocities and therefore energies. Unfortunately, these accelerators have a limit in their accelerating capabilites, for they reach maximum electric fields on the order of 100 MV/m [1]. This means that reaching TeV energies for electrons would require many kilometers of such an accelerating structure which, as a consequence, would be unaffordable. It would be ideal to make an accelerator for electrons with higher accelerating gradients in order to potentially reduce the length and cost of such a structure.

A potential solution is to use a plasma as a generator of electric fields, due to their ability to sustain large electric fields on the scale of GV/m [2]. Past experiments have demonstrated the feasibility of this type of accelerator by driving electric fields within a plasma. Laboratories such as SLAC [3] have specifically used beam driven plasma-wakefield-acceleration, which is the generation of accelerating fields in plasma using charged-particle bunches. These experiments showed the capability to

essentially transfer the energy from one electron bunch to a 'witness' electron bunch behind it within a plasma. Using this technique, SLAC researchers were able to reach accelerating fields of roughly 52 GV/m, allowing for a 42 GeV electron bunch to approximately double its energy.

1.2 AWAKE

The current goal of AWAKE is to use the principle of plasma-wakefield acceleration to accelerate electrons to high-energies. Since the plasma in this case can act as an energy transformer [3], one can transfer more energy to electrons if the energy of the driving bunch is increased. Proton synchrotrons at CERN can produce bunches from 400 GeV up to a few TeV per proton. As a result, these are desired as a driver of plasma wakefields to achieve the highest possible accelerating gradients. AWAKE will be the first experiment to use a proton bunch as a plasma-wakefield driver.

The proton driving bunch will propagate through a 10 m column of plasma and excite wakefields to accelerate a witness bunch of electrons. Using such a system, we should be able to achieve accelerating gradients on the order of a few GV/m. If this is accomplished, then proton-driven wakefield accelerators may become an option for lepton accelerators in the future.

Chapter 2

Theoretical Concepts

2.1 Plasma Wakefields Linear Theory

2.1.1 1D Wakefield Theory

We define a neutral plasma as a state of matter which is composed of ionized electrons and their respective ions. Within this plasma, if one applies a push to an electron in one direction, it will be pulled back by the positive 'hole' of the ion it has left behind, overshoot this hole, and then get pulled back again. This process describes an oscillation of the electron centered about the hole. The frequency of oscillation turns out to be fixed by the density of the plasma, following the equation (assuming non-relativistic electrons)[4]

$$\omega_{pe} = \sqrt{\frac{n_e e^2}{m_e \epsilon_0}} \tag{2.1}$$

where ω_{pe} is the electron plasma angular frequency, n_e the plasma electron density, e the elementary charge, ϵ_0 the permittivity of free space, and m_e the mass of the electron.

The idea behind plasma wakefields is the following: A linearly moving charged particle bunch, which for this example will be of negative charge, propagates close to the speed of light in an overall neutral plasma (see Figure 2.1). As a result, the bunch pushes out plasma electrons through its transverse Coulomb force, causing them to be expelled outwards from the propagation axis of the bunch. Afterwards, they are pulled back towards the propagation axis due to the net positive charges left behind in the plasma, end up overshooting the propagation axis, and so oscillate transversely

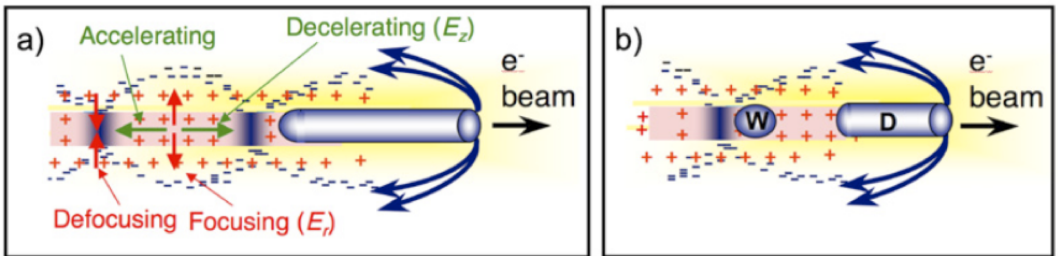

Figure 2.1: In **a)** we see the accelerating/decelerating and focusing/defocusing fields for a negatively charged particle produced by a wakefield initiated by an electron bunch. In **b)** we see the ideal placement of a witness bunch of electrons in order for it to be accelerated and focused. (from [5])

about this axis. This creates fluctuations in charge density along the propagation axis, which generates electric and magnetic fields which we call the plasma wakefields.

Note that in this case, it is assumed that the positive charges in the plasma (which are ions) are heavy enough with respect to the electrons that they can be considered stationary. One can see this is a valid assumption by using equation 2.1 and replacing the electron mass with the ion mass. Since $\omega_p \propto m^{-1/2}$, the frequency of an electron will be much higher than that of its respective ion. This includes hydrogen where the ion is just a proton, as the proton mass is roughly 1836 times that of an electron. The electron period is therefore much shorter than that of the ion, making the ion stationary relative to the electron.

The plasma wakefields generate forces in the transverse and longitudinal directions, as shown in Figure 2.1, which corresponds to varying charge densities on these axes. Those in the longitudinal direction can be used to accelerate/decelerate charged particles and those in the transverse direction can be used to focus/defocus these particles, depending on the particle's charge and location in the wakefield bubble. The wakefield bubble is what we call the oval region of expelled electrons shown in Figure 2.1.

The same idea can be applied to a propagating proton bunch instead of an electron bunch. In this case, the proton bunch initiates plasma oscillations by pulling in plasma electrons towards the propagation axis. The generated wakefields act as an energy transfer between the driving bunch and the witness bunch. So the higher the energy of the initial propagating bunch, the more energy the witness bunch can gain. It is for this reason that we prefer using proton bunches as a generator of wakefields, since we currently find higher energy proton bunches (produced at CERN for example) than

electron bunches.

One can imagine the 'node' of the charge density wave to be where the plasma electrons are bunched along the axis due to the proton bunch pulling in electrons behind it. Since the node is traveling right behind the proton bunch, it necessarily follows the proton bunch velocity. Let's say the proton bunch is moving close to the speed of light, c. The wavelength of the plasma wakefield is therefore:

$$\lambda_{pe} = \frac{c}{f_p} = \frac{2\pi c}{\omega_{pe}}$$

The longitudinal wakefield, otherwise known as the electric field E_z, has an upper limit at which the plasma wave breaks. This is [6]:

$$E_0 = \frac{m_e \; c \; \omega_{pe}}{e} \tag{2.2}$$

otherwise called the wave-breaking field. We can derive this using Gauss's law, by assuming the change in local charge density along the axis of propagation (z) goes from 0 (neutral plasma) to n_e when all the local electrons have been expelled, which is:

$$\nabla \cdot \mathbf{E} = \frac{\rho_z}{\epsilon_0} = \frac{e\delta n_e}{\epsilon_0}$$

where δn_e is the local change in electron density and ρ_z is the charge density along the propagation axis. We can use the wave number $k_{pe} = \frac{\omega_{pe}}{c}$ to get a simple equation for harmonic oscillations of δn_e about the z axis

$$\begin{aligned}
\rho_z = e\delta n_e = e n_e e^{ik_{pe}z} \\
\Rightarrow \nabla \cdot \mathbf{E} = \partial_z E_z = \frac{e n_e e^{ik_{pe}z}}{\epsilon_0} \\
\Rightarrow E_z = \frac{ie n_e e^{ik_{pe}z}}{k_{pe}\epsilon_0} \\
\Rightarrow |E_z| = E_0 = \frac{m_e c \omega_{pe}}{e}
\end{aligned}$$

In order to reach the maximum electric fields possible, it has been shown that the ideal rms (root-mean-square) bunch length, σ_{zb}, along $z - ct$ of the particle bunch should be on the order of $\sigma_{zb} \approx \frac{\lambda_{pe}}{\sqrt{2\pi}}$ [7]. For this case, the maximum electric field is approximated to be [7]

$$E_{max}[MV/m] = 244 \times \frac{N_b}{2 \times 10^{10}} \left(\frac{600}{\sigma_z[\mu m]} \right)^2 \tag{2.3}$$

where N_b is the number of particles in the bunch. A higher number of particles and smaller longitudinal rms bunch length of a driving bunch has the potential to create very large electric fields. Assuming we have the ideal bunch length σ_{zb} for some λ_{pe} of plasma at density n_e, we can solve the electric field equation as a function of n_e. As an example, for $n_e \approx 10^{14}$ cm^{-3}, electric fields of about 1 $\frac{GV}{m}$ can be reached; whereas current accelerating RF cavities have upper limits of about 100 $\frac{MV}{m}$. It is for this reason that plasma wakefield accelerators are so appealing, as they can be made more compact for electron acceleration than current linacs (linear accelerators).

2.1.2 Linear Wakefields in 2D

When the density of the charged particle bunch generating the plasma wakefield is much less than the electron plasma density, or $n_b << n_e$, the linear regime of plasma-wakefield theory is applicable. In linear theory, the longitudinal and transverse wakefields are given by [8]

$$W_z(\xi, r) = \frac{e}{\epsilon_0} \int_{-\infty}^{\xi} n_{b\parallel}(\xi') \cos(k_{pe}(\xi - \xi'))d\xi' \cdot R(r) \propto E_z \tag{2.4}$$

and

$$W_r(\xi, r) = \frac{e}{\epsilon_0 k_{pe}} \int_{-\infty}^{\xi} n_{b\parallel}(\xi') \sin(k_{pe}(\xi - \xi'))d\xi' \cdot \frac{dR(r)}{dr} \propto (E_r - B_\theta) \tag{2.5}$$

where

$$R(r) = k_{pe}^2 \int_0^r r'dr' n_{b\perp}(r') I_0(k_{pe}r') K_0(k_{pe}r) + k_{pe}^2 \int_r^\infty r'dr' n_{b\perp}(r') I_0(k_{pe}r) K_0(k_{pe}r') \tag{2.6}$$

is the dimensionless transverse dependency of the wakefield.

In these equations, $\xi = ct - z$, $n_{b\parallel}$ is the longitudinal component of the bunch

density, $n_{b\perp}$ the perpendicular component of the bunch density, E_z is the longitudinal electric field, E_r the radial electrical field, and B_θ is the azimuthal magnetic field.

Let us consider a simple case of a cylindrical beam, as seen in Figure 2.1. In this case, $n_{b\parallel} = n_{b0}\Theta(L-\xi)$ where L is the length of the beam, $n_{b0} << n_e$, and Θ the Heaviside function which is 1 when $0 < \xi < L$, and 0 otherwise. In this case, it can be shown that the wakefields for $\xi > L$ (looking behind the beam) are: [5]

$$W_z(\xi, r) = \frac{en_{b0}}{\epsilon_0 k_{pe}}[sin(k_{pe}\xi) - sin(k_{pe}(\xi - L))] \cdot R(r)$$
$$W_r(\xi, r) = \frac{en_{b0}}{\epsilon_0 {k_{pe}}^2}[cos(k_{pe}(\xi - L)) - cos(k_{pe}\xi)] \cdot \frac{dR(r)}{dr}$$

We see that W_z and W_r are $\frac{\pi}{2}$ out of phase in ξ. This means that there is a quarter of the wakefield wavelength, λ_{pe}, where a witness bunch of electrons can be placed to experience both focusing and accelerating fields. Figure 2.1 shows a picture of this case, giving the location of the witness electron bunch in the wakefield to experience focusing and acceleration.

When using proton bunches instead of electrons as a wakefield driver, there is a change in wakefield phase from the electron case since the protons pull plasma electrons towards the propagation axis instead of pushing them outwards. The transverse and longitudinal fields are still $\frac{\pi}{2}$ out of phase though, so this phase change is only with respect to the drive bunch. It can also be shown through simulations [9] that the transverse/longitudinal fields are indeed out of phase by $\frac{\pi}{2}$, allowing the witness electron bunch to be placed in an area of simultaneous focusing and acceleration.

2.2 Problems Beyond Linear Theory

2.2.1 Proton Bunch Length

As stated in section 2.1.1, in order to maximize E_z, the rms value of the longitudinal bunch length, σ_{zb}, should be on the order of the wakefield wavelength which is related to the plasma density via $\lambda_{pe} \propto {n_e}^{-1/2}$. As we increase the plasma density, λ_{pe} gets smaller, meaning σ_{zb} also has to be smaller to maximize E_z (see equation 2.3). This means we might be required to lower σ_{zb} to the appropriate size by bunch compression. We also do not want n_e to be too low, as it translates to a higher optimal σ_{zb} which corresponds to lower wakefield amplitudes.

Plasma wakefields essentially act as an energy transformer between the drive and witness bunch. In order to have a larger energy gain for the witness bunch of electrons, we need to use protons since they are currently produced at higher overall energies than electron bunches. Such proton bunches are produced at the SPS (Super-Proton Synchrotron) at CERN with energies of about 400 GeV per proton and 3×10^{11} protons in each bunch.

The problem with using SPS proton bunches comes from the large rms bunch length, which is about 12 cm, corresponding to a maximum E_z of only 0.13 MV/m (see equation 2.3). In order to drive larger wakefields, the bunch is broken up into a 'train' of smaller bunches spaced λ_{pe} apart to resonantly drive the wakefields; basically like driving an harmonic oscillator at its resonant frequency to increase the amplitude of oscillation.

The way to get a multi-bunch train of protons naturally from an SPS bunch is through instabilities produced by the proton bunch propagation through a plasma. This is called the self-modulation instability (SMI). This is a mode of the transverse two-stream (TTS) instability [10], and is essentially the result of radial modulation along the proton bunch from its generated plasma wakefield. The initial wakefields created by the proton bunch, or the 'seed perturbation', proceed to radially focus and defocus certain areas of the rest of the bunch. For this process to occur, we assume the plasma density to be constant, in order for the wakefield wavelength λ_{pe} to be constant. Eventually, this process forms micro-bunches within the focusing regions separated by λ_{pe}, which together generate constructively interfering wakefields resulting in large wakefield amplitudes. This is shown in Figure 2.2.

The defocused protons are expelled radially outwards inside the plasma and form a 'halo' ring of protons. The loss of these protons means they do not contribute to driving the wakefields, making the method of using SMI energy-inefficient. However, it is more cost-effective and easier to implement than using an RF compressor to reduce σ_{zb} [11], so it is sufficient for initial proof-of-principle experiments.

Theoretically, the SMI should work for all plasma densities, so we could resonantly drive plasma wakefields with micro-bunches at any plasma density with an SPS bunch. For example, we could use high plasma densities to have shorter λ_{pe}, and therefore generate higher amplitude wakefields.

The limiting factor in the plasma density is the proton bunch's radial rms value, σ_{rb}, of about 200 μm. The proton bunch is affected by instabilities in r if its beam radius is larger than the plasma skin depth, $\frac{c}{\omega_{pe}} = \frac{\lambda_{pe}}{2\pi}$. The skin depth determines the

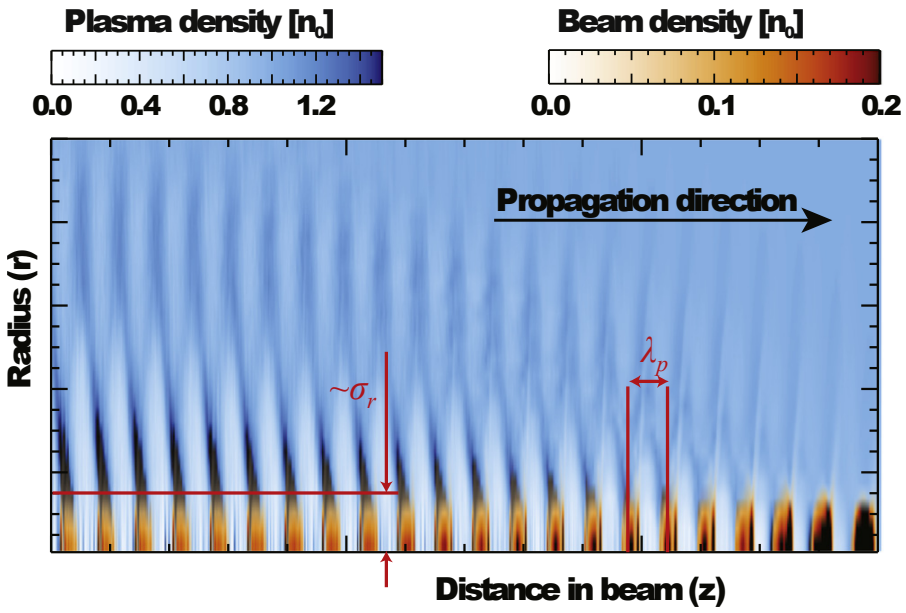

Figure 2.2: Representation of self-modulated proton bunch which drives plasma wakefields. The red/black scale is the density of protons, whereas the blue scale is the density of plasma electrons. We can see that the proton bunch separates into several micro-bunches λ_{pe} apart. (from [11])

length scale of electromagnetic interactions, and if σ_{rb} is greater than $\frac{\lambda_{pe}}{2\pi}$, the bunch no longer fits inside the wakefield 'bubble' and breaks up in the radial direction as well. Therefore, the upper limit of plasma density is in making sure the plasma wavelength is on the order of or greater than σ_{rb} of the proton bunch. The optimal density of plasma electrons for the given parameters of the SPS proton bunch is about $n_e = 7 \times 10^{14}$ cm^{-3} [12], which corresponds to $\lambda_{pe} = 1.26$ mm.

The SMI has been studied theoretically through simulations. This process has to be initiated by a 'seed perturbation' [9], essentially a perturbation at the front of the bunch which generates a wakefield that modulates the rest of the bunch. This seed perturbation allows for amplification of the desired wakefield mode for the SMI to create micro-bunches. Without it, simulations show the SMI may may be influenced by other wakefield modes, which halt the development of the micro-bunches.

The seed perturbation can be initiated with a short electron bunch, a laser pulse, or a sharp cut in the beam profile. In the case of AWAKE, a short laser pulse will be co-propagating along with the proton bunch. This laser pulse will ionize an alkali vapor into plasma, while at the same time creating a sharp cut in the proton bunch

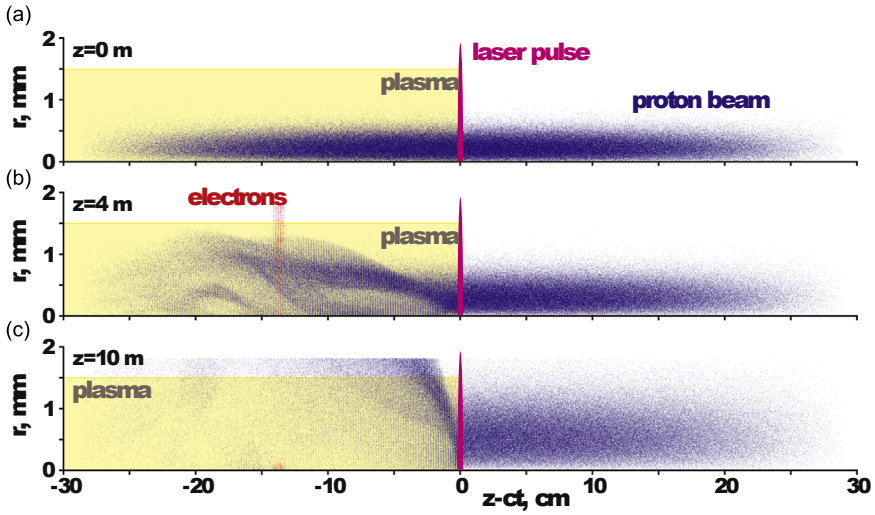

Figure 2.3: Proton beam shown as a function of ξ and radius at different stages: **a)** the entrance of the plasma, **b)** after 4 m of propagation in the plasma, and **c)** after exiting a plasma at 10 m. At 4 m, electrons are injected to show the capture of these electrons within the wakefields. (from [11])

profile capable of seeding the SMI. Consequently, we will essentially have half of the proton bunch propagating through the plasma, whereas the other half will be freely propagating through the neutral vapor without interactions. This is shown in Figure 2.3.

2.2.2 Plasma Uniformity

If the proton bunch self-modulates as it is supposed to, creating micro-bunches every plasma wavelength, then the number of micro-bunches created will be on the order of $N \approx \frac{\sigma_{zb}}{\lambda_{pe}} \approx 100$ for the optimized plasma density ($\lambda_{pe} \approx 1.2$ mm) and SPS proton bunch ($\sigma_{zb} \approx 12$ cm). When dealing with multiple bunches, it is important that the density of the plasma stays uniform. Otherwise, the plasma wavelength will change as the bunch propagates through various densities, causing destructive interference. It is found using simulations [13] that the limiting factor in allowed plasma density perturbations is not with the protons, but with the witness electrons within the wakefields following the proton bunch.

Looking at Figure 2.4 we can see how changes in plasma density affects the witness bunch of electrons. We first assume that we can inject the electrons in the middle of the focusing and accelerating region of the wakefields. If the initial density of the

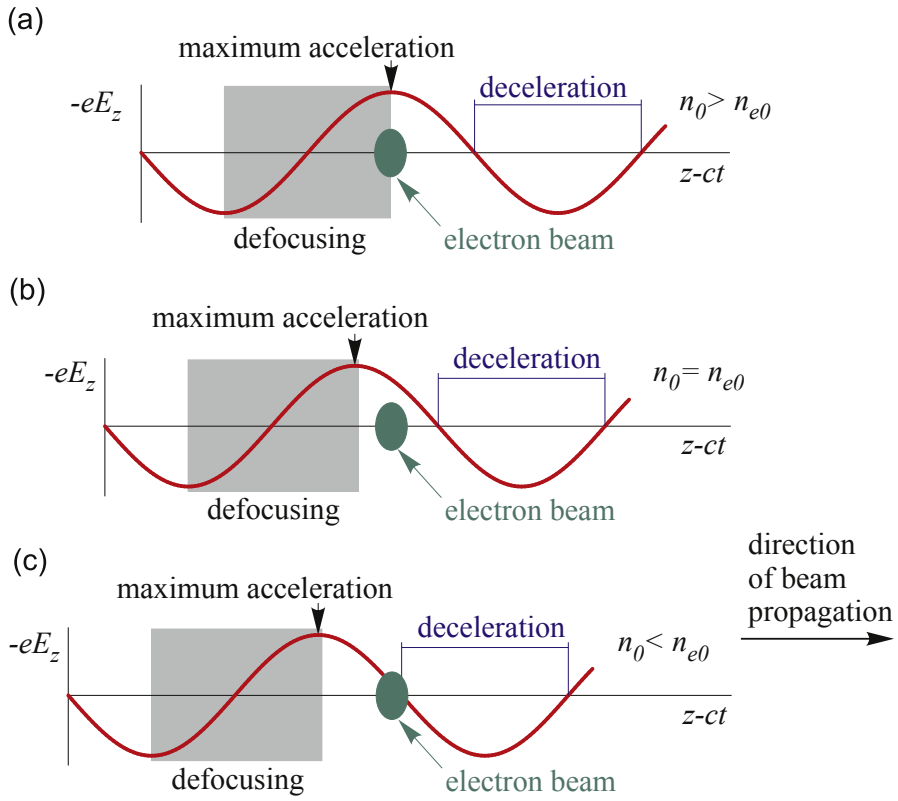

Figure 2.4: Position of witness electron bunch for different density changes, assuming the witness electron bunch is injected into the middle of the focusing/accelerating region at nominal density n_0: **a)** for a sudden increase, **b)** at the normal density, and **c)** for a decreased density. (from [11])

plasma increases, then the plasma wavelength decreases since $\lambda_{pe} \propto {n_e}^{-1/2}$. In this case, the defocusing region of the wakefield catches up to the witness bunch causing it to become defocused. If the density decreases, then the wavelength increases, and the electrons enter into the decelerating portion of the wakefield.

At approximately σ_{zb} behind the cut-off of the proton bunch after undergoing SMI, the longitudinal wakefield reaches a maximum value (see Figure A.15). It is for this reason that we plan to place witness electrons at around σ_{zb} of the proton bunch. We can form a simple way to evaluate the amount of variation allowed in the plasma density at this point. We already know that at the optimal density proposed, the number of micro-bunches is $N \approx 100$ at σ_{zb}. Using the relationship $\lambda_{pe} \propto {n_e}^{-1/2}$, we

can differentiate to get

$$\delta\lambda_{pe} = -\frac{\delta n_e}{2{n_e}^{3/2}}$$
$$\rightarrow \frac{\delta\lambda_{pe}}{\lambda_{pe}} = -\frac{\delta n_e}{2n_e}$$

If we assume the witness bunch is in the center of the focusing/accelerating region of the wakefield (see Figure 2.4b), then the maximum allowed distance the witness bunch can move within the wakefield is $\frac{\delta\lambda_{pe}}{\lambda_{pe}} = \frac{1}{8}$. Any higher and the witness bunch will end up in either the decelerating or defocusing region. We also must account for the fact that the witness bunch is N$\times\lambda_{pe}$ behind the front of the proton bunch. Therefore, we have $\frac{\delta\lambda_{pe}}{\lambda_{pe}} = -\frac{\delta n_e}{2n_e} \times N = \frac{1}{8}$ and so

$$\frac{\delta n_e}{n_e} = \frac{0.25}{N} \tag{2.7}$$

Therefore, for $N \approx 100$ as expected, the maximum allowed density perturbation is a about 0.25%. This is in agreement with simulations studies done on the topic [13].

2.2.3 Phase Velocity

Another issue is that the relative phase velocity between the wakefield and the driving proton bunch is not always constant. It has been shown in simulations [9] that due to the changes in the proton bunch during the growth of the SMI, the phase velocity of the driven wakefield will not match the proton bunch velocity initially. Within the first 4 m of propagation in plasma especially, the wakefield phase velocity will be slower than the bunch velocity. This can be seen in Figure 2.5. As a result, the wakefield travels backwards along the witness bunch, creating problems with either deceleration or defocusing, like in the non-constant plasma density case (section 2.2.2). It is for this reason that any electron injection will have to be done after the SMI development, which is at propagation lengths of about 4 m. After this point, the wakefield phase velocity is approximately the same as that of the driving proton bunch. The plan is for injected electrons to have energies of roughly 50 MeV, so that the velocity of the electron bunch is similar to the proton bunch, and therefore the wakefield phase velocity. Assuming this is the case, then the witness bunch will not move outside of the region it is injected in.

AWAKE plans to contain its plasma within a pipe, through which the proton

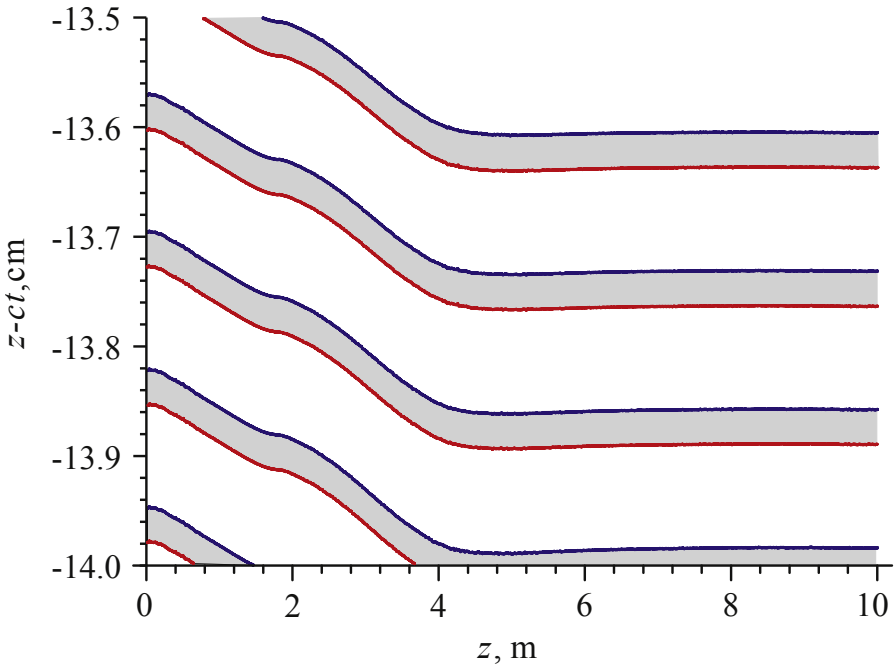

Figure 2.5: Positions along the proton bunch where wakefields are focusing and accelerating (in grey) for a witness electron bunch, as a function of propagation length through the plasma (z). Phase velocity of the wakefields is seen to catch up to the proton bunch, traveling at about c, after 4 m. (from [11])

bunch will propagate. To inject the electrons after 4 m propagation length, the current idea is to inject the electrons at an angle to the z-axis, the axis of proton bunch propagation along the center of the pipe. The angle at which they are injected would be so that the electrons reach the axis after 4 m of proton bunch propagation within the plasma.

2.3 Rubidium Vapor Source

Alkali vapors are typically used as a plasma source due to their generally low ionization potentials, allowing them to be ionized with a laser pulse. We want to limit the plasma density to within the bounds of $\frac{\delta n_e}{n_e} < 0.2\%$ (lower than 0.25% to be safe). Assuming the vapor becomes 100% ionized, the plasma density is the same as the neutral vapor density. Therefore, if one can keep the vapor density constant along a pipe, then the plasma density along this same pipe produced by the laser pulse will also be constant. In the case of AWAKE, rubidium is chosen as the alkali vapor due to its low ionization potential, high atomic mass so that it stays stationary compared to the plasma electrons, and for its low melting point making it easy to vaporize at relatively low temperatures.

One can estimate the neutral rubidium vapor to act as an ideal gas which follows the ideal gas law

$$p = nk_BT \tag{2.8}$$

where p is the pressure, n the density, T the temperature, and k_B the Boltzmann constant. Assuming constant pressure, we can easily derive the relationship between temperature and density perturbations

$$\begin{aligned} n &= \frac{p}{k_BT} \\ \rightarrow \delta n &= -\frac{p}{k_B}\frac{\delta T}{T^2} \\ \rightarrow |\frac{\delta n}{n}| &= \frac{p}{k_B}\frac{\delta T}{T^2} \times \frac{k_BT}{p} = \frac{\delta T}{T} \end{aligned}$$

As a result, if we can keep the rubidium vapor at a temperature with fluctuations of $\frac{\delta T}{T} < 0.2\%$, then we will be able to keep the plasma density within 0.2% as well.

A practical use of rubidium is that it requires relatively low temperatures to get to the desired vapor densities in comparison to other alkali metals. It has a low melting

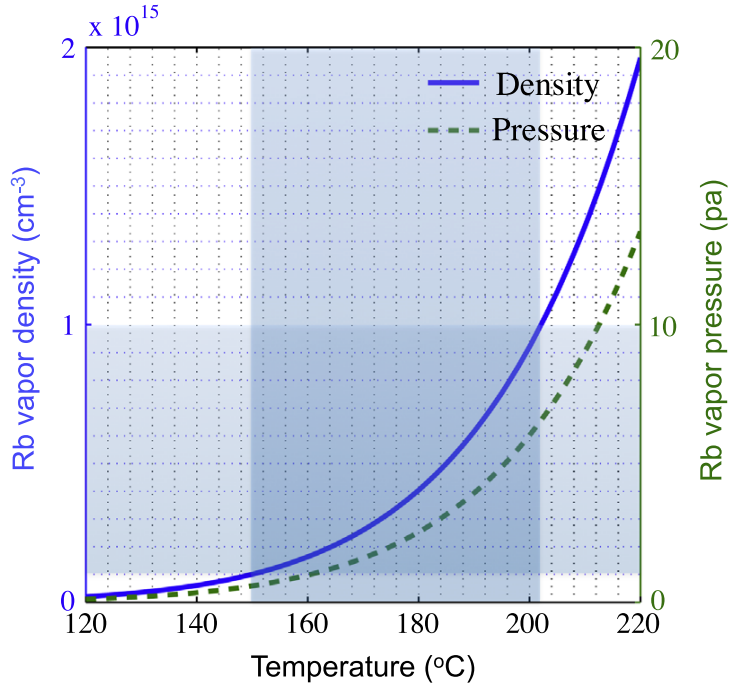

Figure 2.6: Rubidium vapor density (blue line) and pressure (green line) curves as function of temperature. Blue-shaded areas shows the general region of interest for AWAKE experiments.(from [15])

point at 38.5°C, and the temperature to reach densities on the order of 10^{14}-10^{15} cm^{-3} is between 180 and 220°C [14]. This can be seen from the vapor pressure curve of rubidium in Figure 2.6.

To avoid perturbations of less than 0.2%, the temperature of rubidium should be within an interval of 0.85 K at 150°C. If we use this as a baseline, we have to construct a system that can maintain a temperature with a precision of about ± 0.425 K. The best way to maintain a constant temperature is by using stirred liquid baths [16], which have been able to maintain liquid temperatures with precision in the mK range, orders of magnitude better than required.

We want to contain the rubidium vapor in a pipe of standard DN40 size (2 cm radius) and 10 m long to allow the SMI to form micro-bunches out of the proton bunch. An example of what the source would look like is given in Figure 2.7. This shows a pipe surrounded by a heater, which is connected to liquid Rubidium reservoirs at its ends. In this setup, the liquid reservoirs could be heated to some desired temperature to produce a certain density of rubidium vapor. The pipe could then be heated to a slightly higher temperature, that way any rubidium would preferably condense into

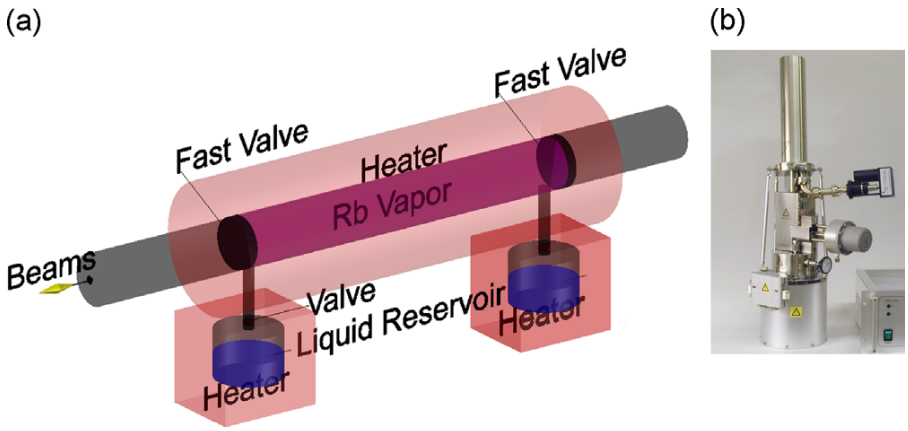

Figure 2.7: **a)** Representation of simple vapor source for rubidium. **b)** Example of a possible rubidium reservoir. (from [15])

the local cold spot of the reservoir. The figure also shows where the proton bunch and laser pulse would go through the pipe. Also shown are potential areas to put fast-valves at the ends, which would open when the bunch passes through and then shut off to keep the vapor from flowing out. It is shown later that this solution is not good enough for our purposes, as it lets out too much vapor at the ends.

One way to measure the rubidium density is through interferometry, specifically called the 'Hook' method [17]. This uses white-light interferometry, in which the rubidium density to be measured is along one of the interferometer arms. The vapor has a ground-state absorption line at 780 nm, which causes the interference patterns to change significantly in this region. These changes can be analyzed to find the density of the rubidium vapor along the interferometer arm.

2.4 Feasibility of Vapor Source

An idea used by AWAKE to keep the pipe temperature constant is to use a stirred temperature bath. We flow hot oil from such a bath around the pipe which confines the rubidium vapor. To do this, we have a concentric cylinder outside the pipe through which oil flows at a high enough volumetric velocity that it becomes laminar flow (meaning the particles essentially travel in a straight line), which acts as a heat resevoir at the temperature of the oil. Consequently, we pump the oil from the bath to one end of this system at the pipe entrance, and then pump it along the outside of

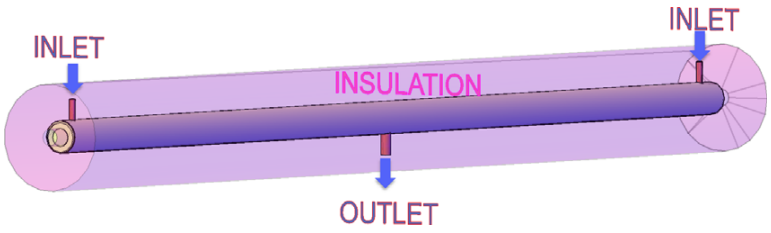

Figure 2.8: Example of oil heat exchanger system. (from [15])

the pipe and out again to the liquid bath. A schematic of such an oil heat exchanger system is shown in Figure 2.8 [15]. In this figure, we can either pump the liquid all the way through from one inlet to the other inlet, or pump through both inlets and outlet the oil in the middle to attempt to minimize temperature losses along the pipe.

Using the calculations shown in section A.5.1, we estimate that the heat-exchanger system as described will have a longitudinal temperature gradient between both ends (ΔT) of approximately 0.23 K for Galden liquid HT270 at 180°C, a middle value of the expected operating temperature range. Galden is a heat-exchanging liquid that is considered for use with AWAKE. ΔT along the pipe is smaller than the required 0.91 K (0.2% of 180°C) interval of temperatures. Even if we halve our estimated volumetric flow rate, change the liquid temperature to 200°C and increase the outside air convection by a factor of 2, we get $\Delta T \approx 0.5$ K; still within the requirements of the experiment.

2.5 Vapor Density Transition Region

At some point along the beamline, the density of the plasma will have to drop off to zero. The ramp from null to the desired density n_e can be particularly harmful to the witness electron bunch. The plasma wakefields generated by the driving proton bunch in a plasma density ramp are generally defocusing for electrons and focusing for protons. The electrons are capable of overcoming the defocusing only in slowly varying plasma densities [11]. If the density ramp is sharp, then the radial force applied to the electrons oscillates as it moves through different plasma densities, and the average of the radial force on the electrons is always defocusing [18].

We call the overall length over which the plasma density goes from 0 to n_e as the transition length L_0 [18]. Another parameter of importance is the defocusing length

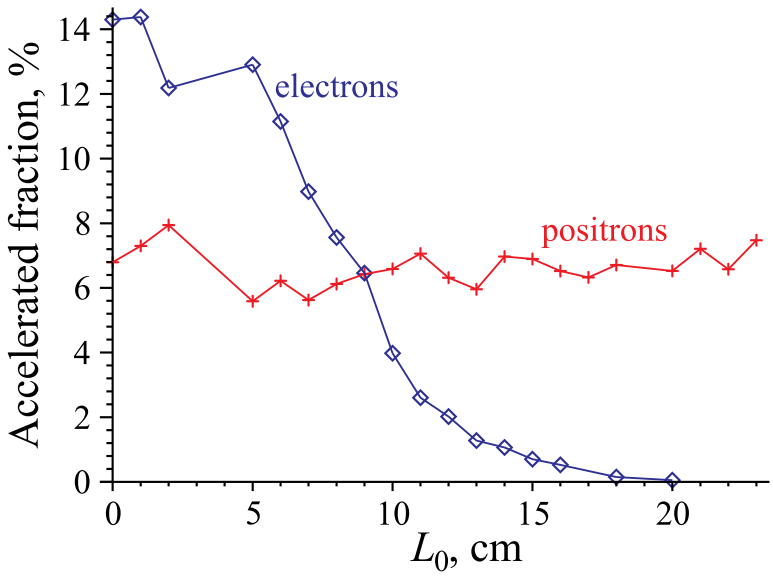

Figure 2.9: Percentage of trapped witness electrons and positrons as a function of transition length (from [18])

L_d, which is the length scale for the density ramp over which radial forces from wakefields defocus the electrons. Ideally, $L_0 < L_d \approx 4.6$ cm [18]; beyond that value, the electrons will be significantly defocused. Simulations have shown the percentage of electrons in the witness bunch, which has a longitudinal rms bunch length σ_{ze} on the order of λ_{pe} for plasma density n_e, that can be accelerated in the experiment as a function of transition length (see Figure 2.9). An acceptable transition length for the first phase of experiments has been deemed to be less than 10 cm, which means about 4% or more of injected electrons would be trapped and accelerated.

As seen in Figure 2.7, the initial idea to solve this density ramp issue was to have fast valves with 10 ms open/shut times. Flow simulations showed that these fast valves would create a transition length of about 1 m, which is far too long to get any reasonable percentage of trapped electrons. The proposed solution is to instead have small orifices at the ends of the vapor source, which would allow for a flow of rubidium vapor into expansion chambers, as seen in Figure 2.10.

It is necessary in this configuration (see Figure 2.10) to make the pipes through which the rubidium vapor flows from their reservoirs as close to the orifice as possible. This way the vapor flows directly out to the chambers without perturbing the density within the vapor source. The general idea is that the vapor can originate from the

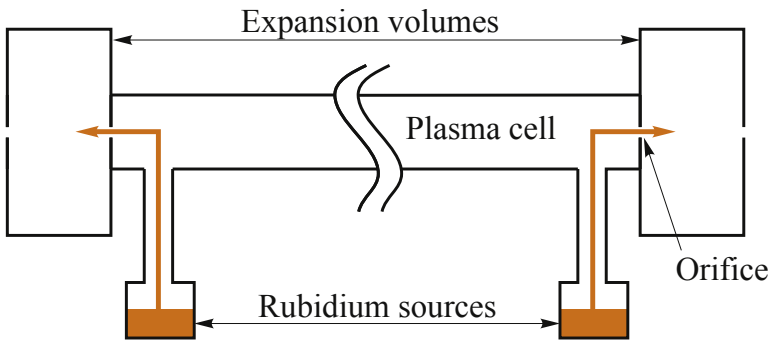

Figure 2.10: Simple schematic of vapor flow solution for vapor source (from [11]).

reservoirs and fill up the vapor source as previously planned. After the vapor source has been filled, most of the vapor will then be forced to flow through the orifice to the expansion chamber. The expansion chamber would ideally be cold enough to condense any rubidium vapor that flows through the orifice. This means the walls would have to be cooler than the melting point of rubidium (38.5°C [14]). The ideal situation would be to have the expansion chamber cooled to room temperature as close to the orifice as possible, to prevent residual vapor from wall temperatures greater than the melting point.

Simulations characterizing the flow of rubidium vapor through such a schematic was done using DSMC (Direct Simulation Monte Carlo) [19] and COMSOL Multiphysics (a general-purpose software for physics simulations) for orifice diameter of 10 mm. These codes showed that the on-axis transition length can be made on the order of a few centimeters (Figure 2.11). An approximation for the on-axis density of gas flow through in the expansion chamber can be found from the equation [19]

$$n_0 = \frac{n_{e0}}{2}\left(1 - \frac{\delta z/D}{\sqrt{(\delta z/D)^2 + 0.25}}\right) \tag{2.9}$$

where D is the orifice diameter, n_0 the on-axis density, and δz the distance to the orifice. This approximation is in good agreement with the DSMC results, which show that the density transition length could theoretically be made smaller than 10 cm.

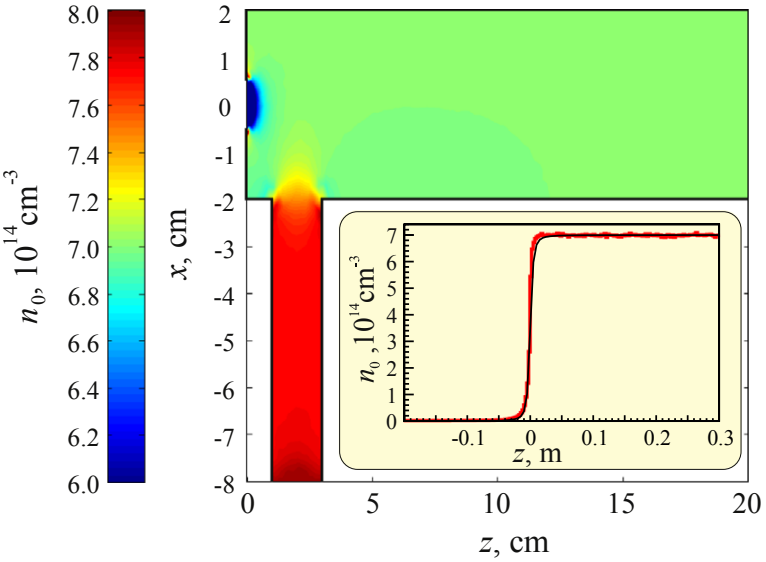

Figure 2.11: Rubidium density in simple schematic near the orifice. Graph shows on-axis density as a function of distance from the orifice. Red line is from DSMC simulation, and black line from theoretical approximations. (from [11])

Chapter 3

Temperature Experiments

As discussed in section 2.3, uniform rubidium vapor density, and therefore plasma density, can be established with temperature uniformity. For this purpose, a method to keep a stainless-steel vacuum pipe at uniform temperature was proposed using oil circulation around the pipe, as discussed in section 2.4. This is called the heat exchanger, and the primary goal is to make sure that the temperature stays uniform along the entire pipe.

3.1 3m Source

The AWAKE group initially worked with the engineering company Grant Instruments from Cambridge to produce a prototype of the heat exchanger. This prototype is 3 m long and uses the oil circulation method described previously to maintain uniform temperature within the pipe. Essentially, a liquid bath is equipped with an electrical heater operated under proportional-integral-derivative (PID) control, as well as a stirrer, basically a small rotating fan. Inside this bath, a liquid can be poured and heated up to 250°C. This bath is also equipped with a pump which can flow the liquid through hoses to either end of the pipe, and then through the cylindrical shell surrounding the pipe. The oil then flows back out either through the center (if initially pumped into both sides) or the other end (if initially pumped into one end) back into the heat bath. The overall schematic is shown in Figure 3.1. The design schematic for the 3 m heat exchanger, which we also call the 3m source for short, is shown in Figure A.18. These components are currently found at the Max-Planck Institute for Physics in Munich (MPP).

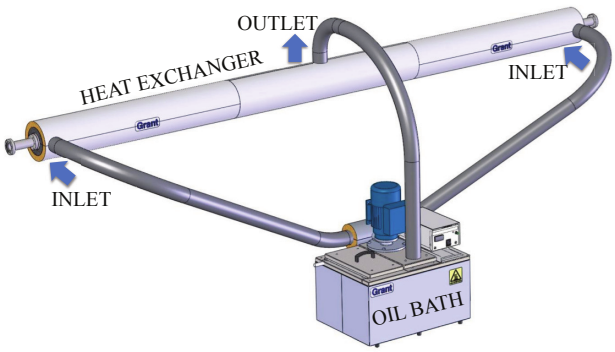

Figure 3.1: General setup of heat exchanger and liquid bath for operation. The liquid is pumped from the bath to the inlets, and goes back to the bath through the outlet in this schematic. (From [15]).

The typical candidates for heat-exchanging liquid are oils. Silicone oil, for example, is commonly used as a heat exchanger liquid due to its good heat transfer characteristics and temperature stability. It is for this reason it was considered a good initial candidate for the heat exchanger. The specific name of this oil is the Hoesch Silicon Oil 50cSt.

It was previously shown that temperatures within the pipe of the heat-exchanger could be kept within an interval of 0.2% using this oil [15]. The success of this heat exchanger prototype has led to the creation and testing of a 10 m heat-exchanger system that will be used for the final plasma column in AWAKE.

To perform temperature measurements on the 3m source, temperature sensors with relative accuracy within ± 0.05 K are desired. As a result, Pt111 (platinum resistance) temperature probes were relatively calibrated using the stirred oil bath filled with Silicone Oil (see section A.1). Fifteen probes were calibrated to within ± 0.05 K for temperatures between 20 and 220 °C, except for one which was slightly problematic and more on the order of ± 0.1 K. To validate the use of these probes, they were tested on the 3m source using Silicone Oil, and showed that the temperature inside is maintained within an interval of 0.18 K for oil temperature of 180°C (see section A.2), which is similar to previous tests [15].

3.2 Galden Liquid

One of the problems with Silicone Oil is having to pump out the Formaldehyde it produces at high temperatures. Another problem is that the flash point is at 250°C, which we consider too close to the maximum operating temperature of 230°C. If something were to happen and the oil temperature suddenly rose above 250°C, a fire could start creating a potentially dangerous situation for nearby workers, as well as ruining the experiment. It is for this reason that another liquid was found with a higher flash point.

The primary candidate for the new liquid was Galden HT270, which does not have a listed flash point. This liquid has a higher viscosity and lower specific heat than the silicone oil, but according to simple calculations it is still satisfactory as a heat exchanging fluid (see section A.5.1). Another issue is that the boiling point is at 270°C, meaning that even at temperatures lower than 200°C, the liquid will start to vaporize considerably, causing us to lose a bit of the liquid in the process.

3.2.1 Galden Tests

We repeated the same temperature experiments with the 3m source as before, but using Galden Liquid instead of Silicone Oil to see if it can maintain the temperature uniformity standards. As a result, the Silicone Oil was poured out of the bath and the 3m source, which were then cleaned with oil cleaners and Isopropyl alcohol.

The experimental setup remained generally the same as for the Silicone Oil run but with Galden Liquid as a replacement. A schematic of the setup is shown in Figure 3.2. The probe rod in this figure is a thin aluminum rod with probes placed every 18 cm to measure the inside of the pipe. The bath was covered with a plastic box, so that any Galden vapor would condense on the walls and drip down into the container instead of the floor. An exhaust pump was also used to pump the vapor outside (see Figure 3.3).

The experiment was run for a couple hours, with the same bath temperature of 180°C as before. In an attempt to get more data points, the rod with the probes was moved back an additional 9 cm after the first measurements in order to get twice the amount of probe position measurements. The tabulated results (Table A.3) and graphical results (Figure 3.4) are shown.

First one should notice that there are three position points missing in Table A.3 at positions 163, 172, and 199 cm. When soldering the probes, since the wires and leads

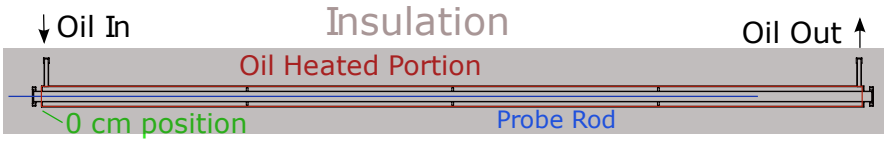

Figure 3.2: Simplified drawing of the experiment. Everything was covered in rock-wool insulation, and the probe rod was placed inside the 3m source. The hot oil was inlet from one side and outlet the other. Also shown is the 0 cm point for probe position at the beginning of the oil heated section, with positive positions going into the 3m source.

are so thin, it was very difficult to apply a thick layer of solder when soldering the leads and wires. The probes would work initially when the experiment was not running, but during the experiment, the pump caused enough vibrations to potentially create loose connections in the probes, creating random fluctuations in temperatures of the probes. Those with such fluctuations were deemed 'faulty' probes and the points were therefore ignored.

In Figure 3.4b, a strange dip in temperature around the middle of the 3m source happens at 145 and 154 cm. These two measurements were made by the same probe. It will be discussed later (see Section 3.3.1), but it turns out that the dip is most likely due to a poorly calibrated probe. Even including this measurement and the previously discussed issues, the mean temperatures for the probes along the uniform section is within 0.54 K, which is in the 0.91 K interval that we desire. Without the unusual dip, the measurements stay within a 0.32 K interval. This shows that using the liquid heat exchanger with Galden HT270 is sufficient for keeping temperature, and therefore rubidium vapor density, within 0.2% along a 3 m pipe. Since no longitudinal temperature gradient is seen, likely due to the radial mixing of the liquid around the pipe, we assume that this liquid will also be adequate for use with the 10 m heat exchanger at CERN.

3.3 The Vapor Source Ends

At the Vapor Source Ends there will be an expansion chamber for rubidium condensation (see section 2.5) and a window for rubidium vapor density measurements using interferometry techniques. This means we need an extension of uniform heating past the heat exchanger, as it does not currently have a window for such measurements.

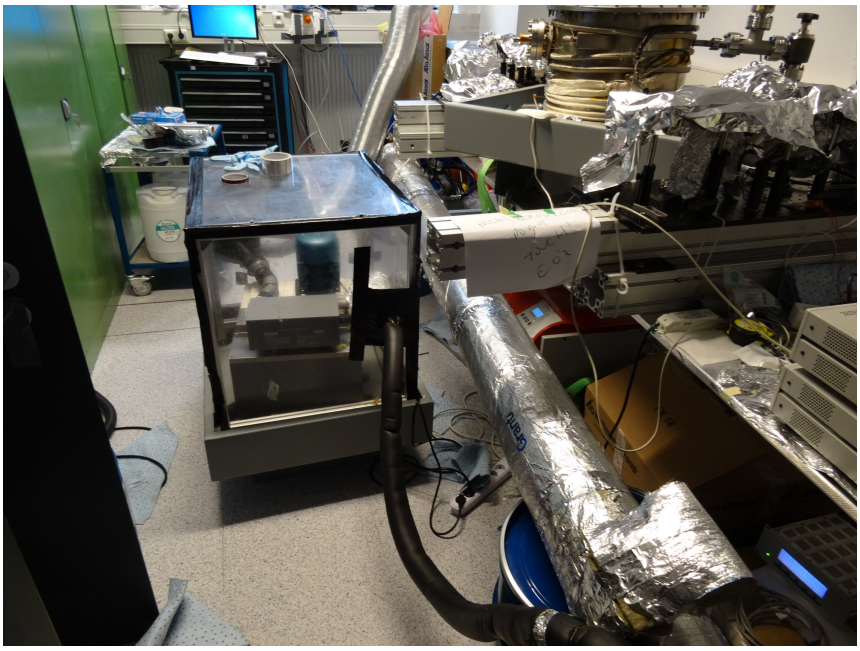

Figure 3.3: Example setup where we can see the liquid bath covered with a plastic box on top of a container for vapor condensation. Exhaust pump also attached to get rid of vapor to the outside. Also see insulated covered (black) pipes connecting to the 3m source, also covered in rock wool insulation (silver).

Since the liquid heat exchanger system has already shown a desirable temperature uniformity, the natural next step is to extend this system further. For the development of this system, we are working with an engineering company from Cambridge, UK called Wright Design Ltd (WDL). In collaboration with this group, a preliminary design for the Vapor Source Ends was proposed. The general cross-section of this design is shown in Figure 3.5.

Looking at the cross-sectional design, the additional piece that is added is composed of two parts. The 'manifold' portion is essentially an extension of the liquid heating, and is bolted onto the heat-exchanger. This includes any portions that are contained within the liquid-heated section that is not part of the main heat exchanger. There is also an aperture and an expansion volume, which is eventually what we want the rubidium vapor to be flowing through and condensing on. Proof-of-principle tests of this sort of system were desired, and so components that could be quickly manufactured were designed for use in experiments with the 3m source at MPP.

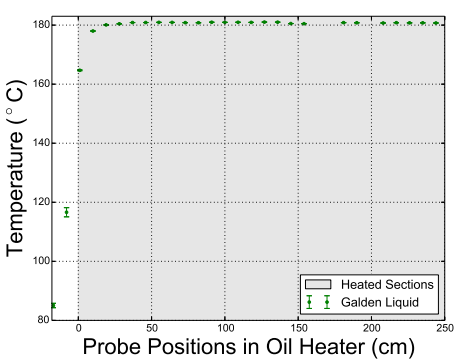

(a) Overall temperature profile

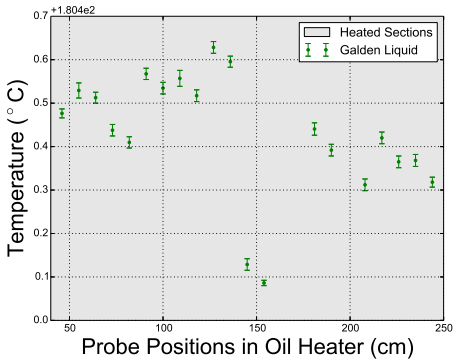

(b) Temperature profile inside the uniform section

Figure 3.4: Result for 3m source run with Galden Liquid at 180°C bath temperature. Shows mean temperature and σ_T of each probe as a function of probe position. Each probe has two measurements associated with it.

3.3.1 The Manifold

One additional piece that was designed is the manifold, which is essentially like a miniature heat exchanger. The overall design schematic is shown in Figure A.19.

The manifold works just like the heat exchanger: Galden liquid is pumped into one port and comes out at the other side. In this case, the manifold can be bolted onto the 3m source either by flange-to-flange connection, or directly onto the 3m source flange on the other side, which for reference, will be called the bolt-on side. For the secondary option, the assumption was that the smaller distance between the Galden heated sections of the manifold and 3m source, in addition to the surrounding rock-wool insulation, would prevent enough conductive heat loss that the temperature dip between them would be negligible.

A simple calculation for the heat loss between the 3m source and the manifold for the flange-to-flange scheme can be done for a liquid temperature of 180°C (see section A.5.2). The temperature dip between the two is calculated to be about ΔT = -2.40 K. So even in a simplified model, the dip in temperature is too large to maintain the temperature uniformity standards.

3.3.2 Manifold-to-3m Source Experiments

To test the temperature drop between the manifold and 3m source, the manifold piece was bolted to the 3m source to minimize heat loss. The same aluminum rod used in

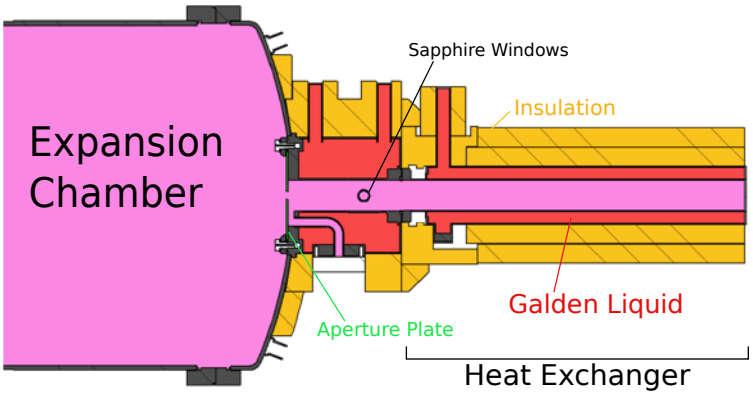

Figure 3.5: Cross-sectional design from WDL of the Vapor Source End. Composed of extended liquid heating with sapphire window, an aperture plate, and an expansion volume. It is shown bolted onto the heat-exchanger.

previous experiments with probes 18 cm apart was placed in the system. One change is the 0 cm probe position is now where the inner pipe-line starts at the manifold flange (see Figure 3.6). Galden Liquid is now pumped through the system first into the manifold, where it flows in and out, and then in again to the 3m source and back out to the bath.

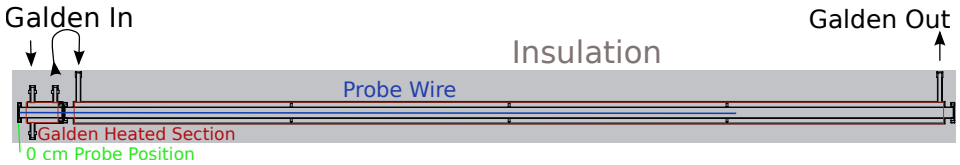

Figure 3.6: Drawing of manifold-to-3m source experimental setup. Shown is the direction of Galden flow, as well as the new 0 cm position for the probes in the system.

The bath temperature was set to 180°C again for consistency with previous experiments. The system was completely covered in insulation, though the insulation covering the end near the manifold had a small hole so that the probe-rod could be pulled out during the experiment. After the probes reached stable temperatures, the probe rod was pulled out (outside the manifold portion) at distances of 1, 2, 3, 4, 6, 9, 12, 15, and 18 cm. Consequently, the last measurement for a probe has positional overlap with the previous probe since they are placed 18 cm apart. This was the best way to get several measurements in between the two oil heated sections of the manifold and 3m source, allowing for good relative temperature measurements by using the same probe pulled through this region of interest. This also allowed us to get a

better idea of how different the temperatures recorded by different probes are inside the uniform section of the 3m source, and better resolve the region with the dip seen in the previous experiment with Galden. For each pull, sufficient time was allowed for the probes to reach a stable temperature before pulling the probes further.

The temperature profiles for each probe are shown in Figure 3.7. It should be noted that different colors represent different probes, which have several measurements due to the probe rod being pulled up to 18 cm. One should also notice that two probes were deemed faulty, and so are not shown.

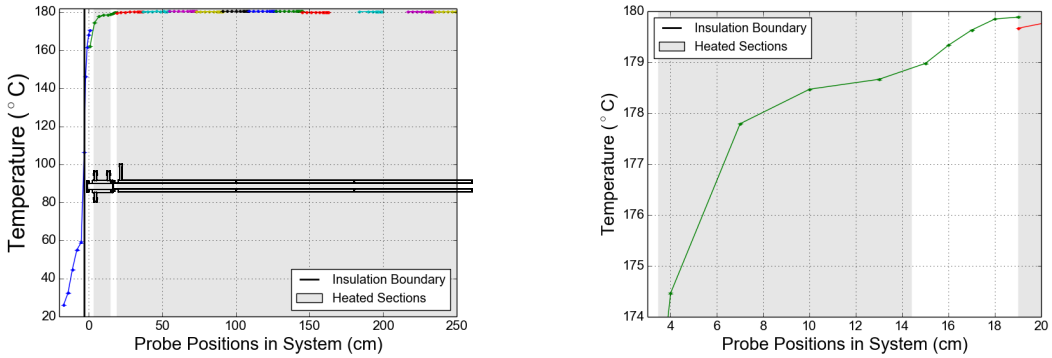

(a) Overall temperature profile measured, with manifold and 3m source drawn over top.

(b) Temperature profile between the manifold and 3m source.

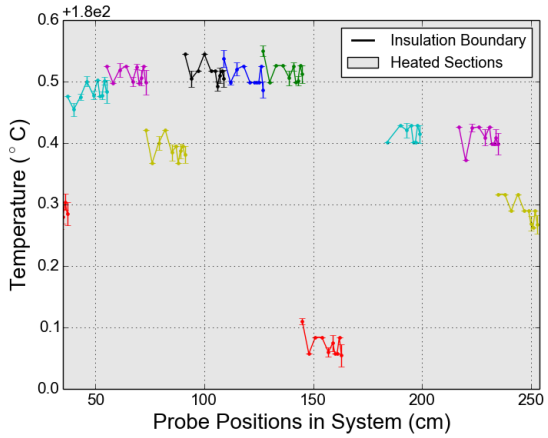

(c) Temperature profile of several probes inside the 3m source.

Figure 3.7: Temperature profiles of probes for the manifold attached to the 3m source experiment. Different color data points represent different probes measured over several positions. Error bars are standard deviations of temperature.

Taking a look at Figure 3.7a, we now have a known boundary for the insulation

covering the manifold, which has a small hole in it for probe pulling. The aluminum rod eventually gets exposed to air, which results in another source of heat loss. We can also see that measurements close to 0 cm for the leftmost green probe are lower than the first few points (rightmost) on the blue probe which crosses the insulation boundary. The lower temperatures for the green probe are likely due to the loss of heat through the aluminum rod which is exposed outside during these measurements. It is for this reason, and the time needed to wait for equilibrium after each pull, that future tests do not implement the probe pulling method.

Looking at Figure 3.7b, we see that the temperature from the Galden heated section in the 3m source to the heated section in the manifold drops by about -1.22 K, which is larger than the 0.2% temperature deviation allowed. We also see that the assumption of the temperature at the heated sections being the same as the liquid temperature is invalid. This is the case as the temperature inside the manifold is smaller than that within the 3m source, meaning the heat loss through the ends and the manifold-3m source connection extends to inside the manifold heated portion. It is clear from these measurements that simply reducing the distance between the liquid-heated sections will not be adequate for maintaining temperature uniformity.

Looking at Figure 3.7c, the temperature profiles of each probe as it is pulled over 18 cm is shown; where each color represents a different probe on the rod. Each probe measures its own mean temperature within 0.06 K or less over an 18 cm distance. At the same time, there is a large temperature difference of about 0.4 K between overlapping measurements for the probe in red and green at 145 cm. Other overlapping probe measurements also have temperature differences on the order of 0.1 K. This implies that the probes are not relatively calibrated to the ± 0.05 K precision that was given in Section A.1. However, since all the probes stay quite uniform within 18 cm, the overall temperature uniformity is likely better than the 0.52 K shown in Section 3.2. This reconfirms that the heat exchanger using Galden liquid maintains temperature uniformity within 0.2%. In addition, we see that the red probe doesn't have any significant dip in temperature around 150 cm as seen in Figure 3.4b. This also means that the dip seen in Figure 3.4 is a result of an offset between probe measurements due to poor calibration, and is not a physical dip in temperature in the center of the 3m source.

3.4 Disc Measurements

It had become obvious that an extension of Galden heating alone will not be enough to keep a uniform temperature to the ends of the Vapor Source. Additional electrical heating applied to the unheated portions will be necessary to keep the temperature uniform all the way to the aperture/expansion chamber (see Figure 3.5). To test this idea, a representation of the expansion chamber is needed for our current system at MPP. For this, a 5 mm thick, 400 mm diameter disk was manufactured. This is supposed to represent the initial, radially outward extension of the expansion chamber shown in Figure 3.8.

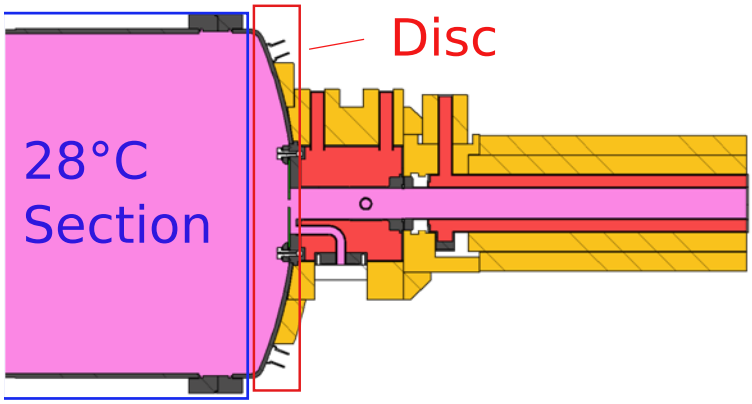

Figure 3.8: WDL Ends design with expansion chamber and disc representation shown.

To better represent what we hope to be the final design, we will want to attach the disc directly to the bolt-on end of the manifold to minimize the distance to the Galden heated section.

3.4.1 Disc Experiments without Additional Heating

A proof-of-principle experiment was setup to represent the Vapor Source Ends. In this case, we have the 3m source bolted onto the manifold by flange-to-flange connection. The disc was consequently attached via the bolt-on side of the manifold, that way the Galden liquid heated section is closer to the disc (like in the prototype design). The general setup is shown in Figure 3.9. Once again, the liquid is pumped first through the manifold, and then through the 3m source.

Insulation was applied only to the outside surface of the disc, as we should not have any convection inside the expansion chamber (as it is under vacuum). We do, however, want to keep the rest of the disc exposed to air since air convection is useful

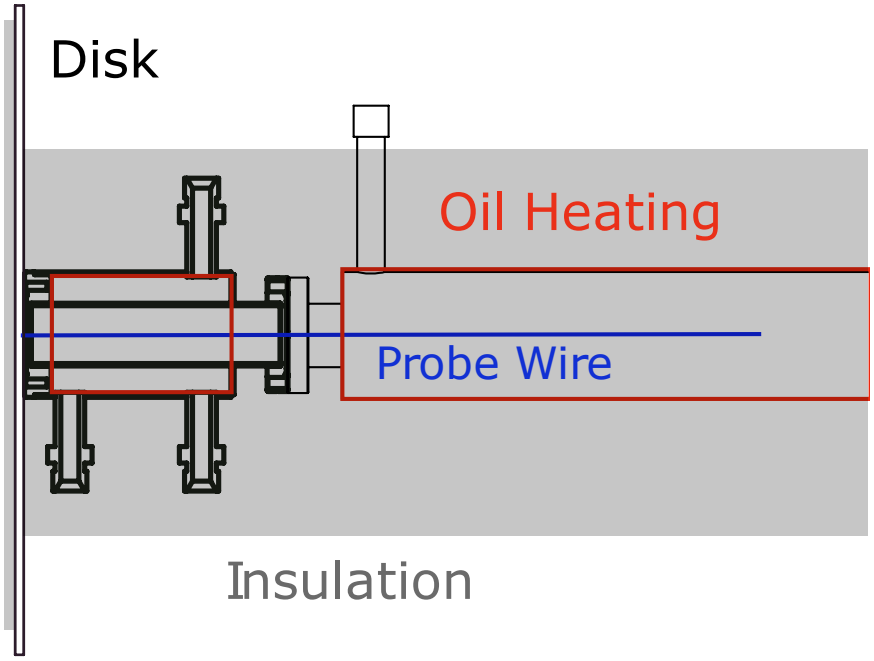

Figure 3.9: Sketch of experimental setup with disc, manifold, and 3m source.

for cooling the disc, and therefore the expansion chamber. As mentioned previously, we want the expansion chamber to be cooled enough so that rubidium condenses on the expansion chamber walls. For this, we deem an appropriate temperature of the chamber walls to be 28°C (or less), which is roughly 10°C less than the melting point of rubidium.

For this experiment, the same probe arrangement was used as in the flipped-manifold experiment in Section A.3. This covers a distance of 34 cm to probe temperatures along the manifold and part-way into the 3m source. The experiment was again run at 180°C bath temperature, and the Galden was circulated in and out of the manifold, and then in and out of the 3m source as usual. The results are shown in Table 3.1 and Figure 3.10.

Looking at Figure 3.10 and Table 3.1, we see the expected dip in temperature between the manifold and 3m source Galden heated portions. We also see a greater drop in temperature at the end than in the previous experiment because of the additional heat loss through the disc. The temperature at the very end near the disc is 163.30°C, which is less than the 167°C calculated in Section A.5.3. All of the calculations made (see section A.5.3) are too simple, as they continually underestimate the

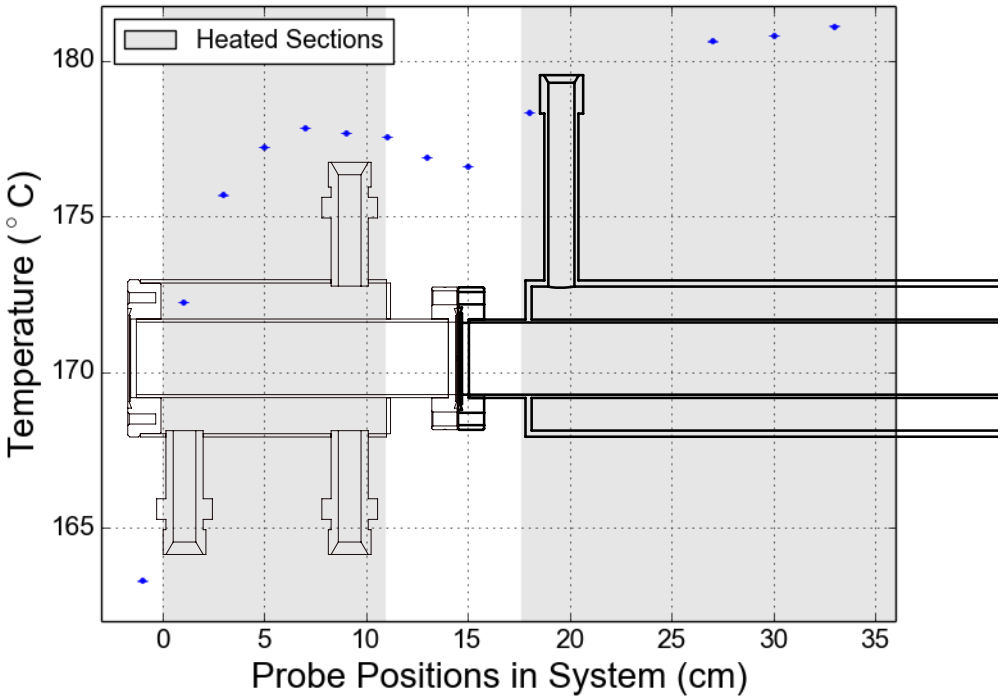

Figure 3.10: Temperature profile as function of probe position within the system. Since σ_T is so small in this case, we set the measurement error for each temperature to be $\pm$ 0.05°C, the previously expected uncertainty for a single measurement.

heat loss from within the Galden heated sections, so the real measured results will always be worse than what is calculated. Through these measurements, we essentially show that rock-wool insulation is not enough to prevent significant heat loss through the unheated components in the system, which disrupts the temperature uniformity.

3.4.2 Additional Heat Added

In order to get a uniform temperature until the disc end of the manifold, we will need additional heating applied to the system. For the purpose of simple tests, we use heating tapes, which are long-band flexible electrical heaters with glass-insulated fabric coatings.

We applied heating tapes around the bolt-end of the manifold with the disc attached and around the flange-to-flange connection, and controlled these tapes using PID control, which required a thermal sensor (called the control probe) between the tapes and the surface of the heated components. We select the set point for the tem-

Table 3.1: Temperature for each probe as a function of probe position for the experiment with disc attached.

Probe location (cm ± 0.5)	**Temperature (°C ± 0.05)**
0	163.30
2	172.23
4	175.69
6	177.24
8	177.85
10	177.69
12	177.57
14	176.91
16	176.6
19	178.32
28	180.61
31	180.80
34	181.11

perature of the sensor, and the PID controller sets varying power outputs through the tape until the temperature is reached and stable over time.

We also monitor the radial temperature of the disc, specifically to see how hot the disc gets at the end to see whether additional cooling will be needed for the expansion chamber to reach 28°C. For this purpose we use Pt100 probes, another platinum resistance probe. The Pt100 probes measure temperature based on the standard curve for Pt100 probes, which is only accurate to about ±1 K. This poor precision is not considered a drawback in this case since we only want to observe if the temperature at the end of the disc falls close to 28°C.

The general setup of the final experiment is shown below in Figure 3.11. In this setup, we have the bolt and disc covered with heating tape, as well as part of the flange-to-flange connection between the manifold and 3m source. An estimate of the heating tape power needed near the disk had to be tested before implementing this configuration (see section A.4). Some pictures of the system are shown in Figure 3.12.

As shown in Figure 3.12a, the heating tapes were wrapped around the manifold end attached to the disc, and around the manifold flange. Each heating tape had a thermal sensor (Pt100 probes) between the tapes and the steel surface. Both the heating tapes and their respective sensors were connected to Omega CN7800 series temperature controllers, which uses PID control to heat the tape at varying output

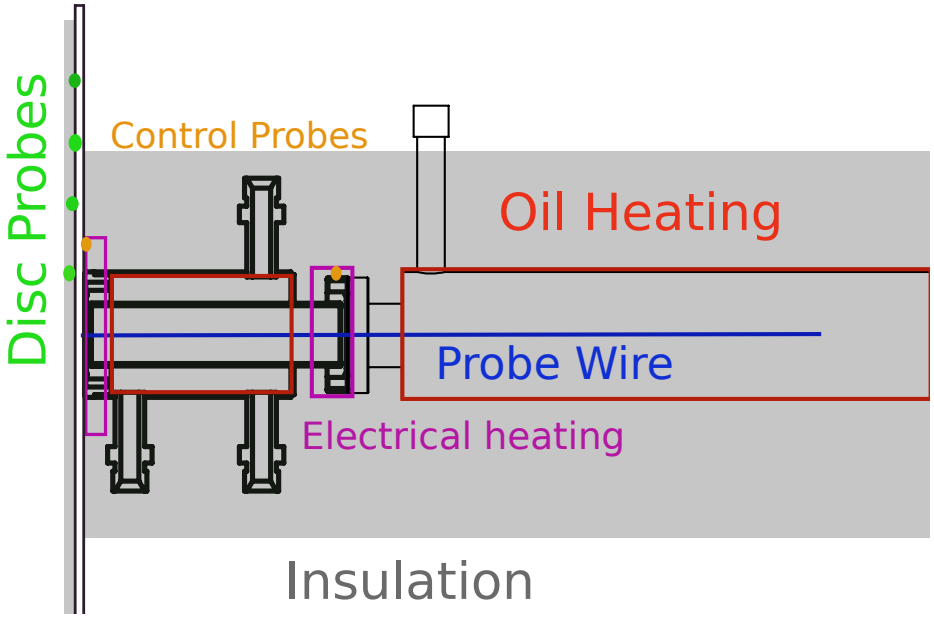

Figure 3.11: Sketch of experimental setup with disc, manifold, and heating tapes. Parts color coded for simplicity.

power to keep a stable set temperature of the probe.

The Pt100 probes were taped radially along the disc in order to measure the radial temperature profile of the disc. We can see this without added insulation in Figure 3.12c. Once again, the Pt111 probes were placed on the aluminum wire within the system at the same positions as in the previous experiment.

In general, the set temperature of the sensors for each tape were selected via trial and error. For the high-powered tape at the disc, the set temperature was 270°C; whereas for the tape at the flange-to-flange connection, the set temperature was 183.5°C. The results are shown in tabulated (Table 3.2) and graphical (Figure 3.13) form.

Looking at Figure 3.13, we see that overall, the mean temperatures are within 0.6 K which satisfies the temperature interval of 0.91 K. The larger issue that we see are the large fluctuations in temperature near the disc, with σ_T going up to 0.2°C. This might be due to the fluctuations in power of the disc heating tape due to PID control. When the sensor was at its set temperature, the heating tape would operate at almost maximum power output (≈200W). The PID controls the heating tape power output, and lowers the output after the sensor temperature goes above its set value. These swings in power results in the relatively large swings in temperature within the

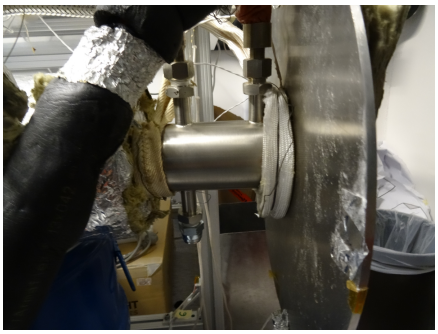

(a) Disc setup with electrical heating tapes and no insulation.

(b) Disc setup with electrical heating tapes after insulation applied.

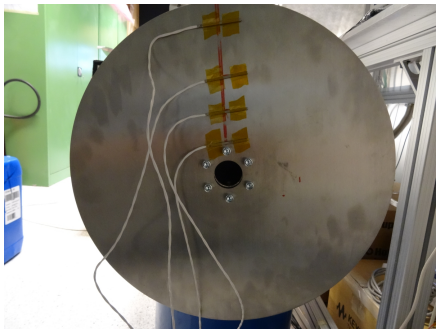

(c) Probe placement on disc before applying insulation.

Figure 3.12: Pictures from the setup of the experiment with the heat-exchanger, manifold, and stainless steel disc. Additional heating tapes applied to unheated portions of the flange-to-flange connection and around the end of the manifold in contact with the disc.

manifold pipeline. If the system had been allowed to run over a period of about 24 hours, it is more likely that the deviation in temperature would have decreased; as PID control maintains a more stable temperature over time.

The radial temperatures of the disc measured by Pt100 probes are shown in Figure 3.14. It is first interesting to note that the temperature of the disc at 0.04 cm radius is 195.8°C, so a higher temperature on the disc than the Galden liquid is needed to offset the temperature dip near the disc. Also, the trend shows that the temperature will not fall close to 28°C at its end. This means that for the expansion chamber, additional cooling will be necessary to cool the chamber down to 28°C for rubidium condensation.

As a result of these tests, we determined that the final design will need additional heating at the connection point between the heat exchanger and the ends, as well as on the disc of the expansion chamber to offset the heat loss through these components.

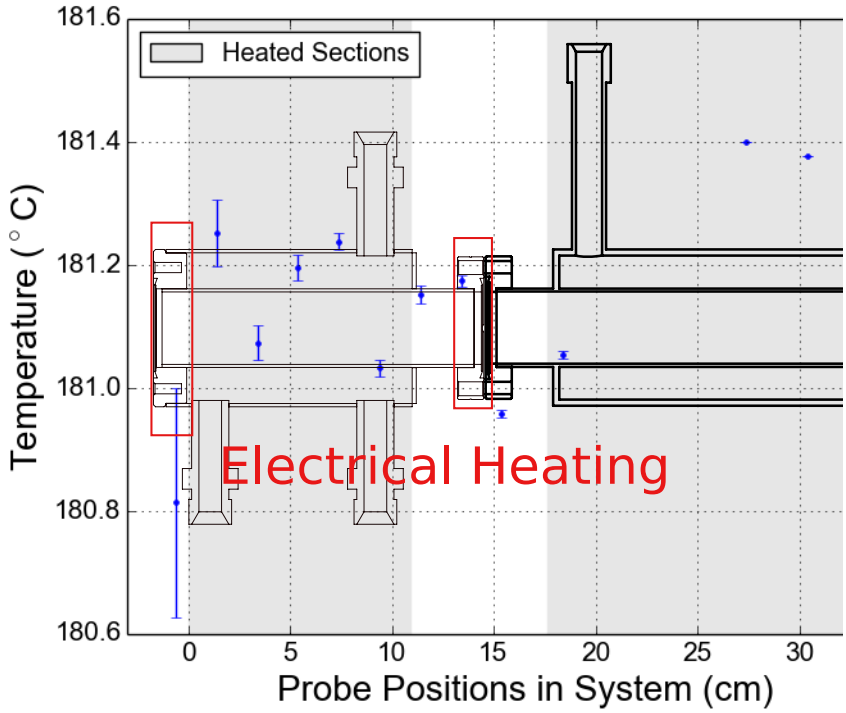

Figure 3.13: Temperature of probes vs position for setup with disc, manifold, and 3m source with electrical heating tapes added. Error bars are σ_T.

Assuming we find more reliable electrical heating components than heating tapes, we should be able to maintain the temperature uniformity standard of 0.2% along the pipe-line and up to the expansion chamber with these additions. Furthermore, cooling will be required at the outer radius of the expansion chamber disc to keep the rest of the chamber at 28°C for rubidium condensation. This will allow us to have the sharp ramp in rubidium vapor density required for AWAKE.

Table 3.2: Temperature and standard deviations for each probe as a function of probe position for two heating tapes test.

Probe Position (cm ±0.5)	**Probe Temperature(°C)**	σ_T **(°C)**
-0.6	180.8	0.2
1.4	181.25	0.05
3.4	181.07	0.03
5.4	181.20	0.02
7.4	181.24	0.01
9.4	181.03	0.01
11.4	181.15	0.01
13.4	181.174	0.009
15.4	180.958	0.007
18.4	181.053	0.006
27.4	181.400	9e-13
30.4	181.377	2e-12
33.4	181.58	0.01

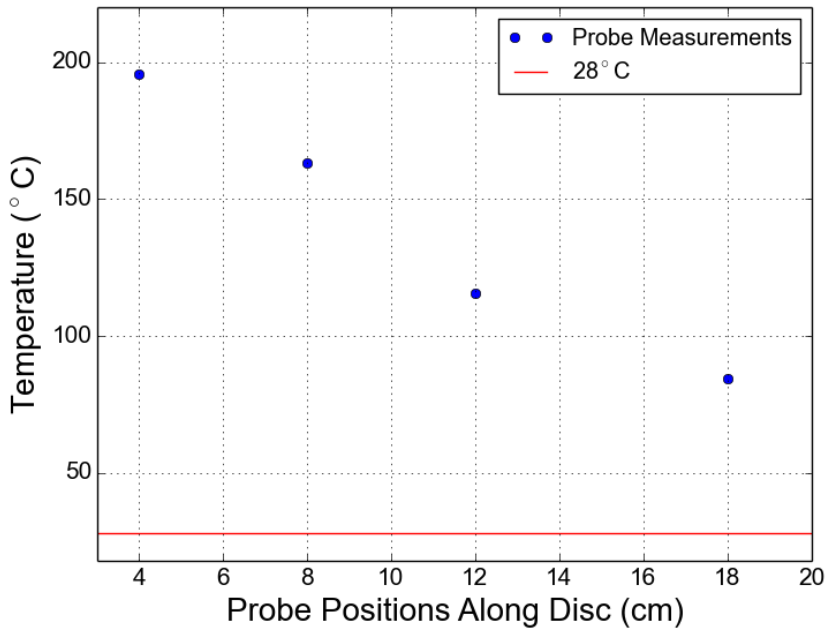

Figure 3.14: Radial temperature profile of the disc when two heating tapes are added to the system.

Chapter 4

OSIRIS Simulations

As discussed in section 2.2.3, the phase velocity of the wakefield does not reach that of the proton bunch until the bunch has propagated a few meters within the plasma. For the purposes of the AWAKE experiment, we want to inject test electrons within the accelerating and focusing region of the wakefield to test its capabilities. There is little room for error in the injection of electrons since this accelerating/focusing region is within $0.25\lambda_{pe}$ in ξ according to linear theory. As a result, we need to inject after the wakefield phase velocity stabilizes so the electrons, which we assume to be moving at the velocity of the proton bunch, do not move out into regions of defocusing/deceleration due to the phase variation. According to previous studies done with LCODE (a code specifically created to simulate particle-driven plasma wakefield experiments), the self-modulation instability (SMI) process and therefore wakefield phase-velocity stabilizes after about 4 m bunch propagation [9].

For the experiment, we will be using proton bunches from the SPS at CERN, which have a given set of initial parameters. We want to account for how differences within the given parameters of the proton bunch will change the wakefield phase stabilization. For this reason, it is useful to find the necessary tolerances on the initial parameters in which electron injection experiments will not be significantly impacted. An insignificant impact is considered to be if the changes to the location of injection for accelerating/focusing electrons, and the resultant energy gain of these electrons, is small. We deem a good starting point for these tolerance studies to be variations in the initial bunch parameters by $\pm 5\%$. As a result, in this Chapter we study how a variation of $\pm 5\%$ in these parameters will affect the phase of the generated wakefield. To study this, we use a plasma simulation software called OSIRIS, developed at the Instituto Superior Tecnico in Lisbon and at UCLA [20].

4.1 PIC Software

An accurate model of the experiment needs to include effects beyond linear wakefield theory. The system is inherently complex, as the many particles within the plasma (electrons and their respective ions) interact with the many protons in the driving bunch. In order to simulate such a system, Particle-in-Cell codes are used. These codes use Maxwell's Electromagnetic equations in order to solve the time-dependent interaction between all these charged particles. In order to do this, particles are represented by overall particle densities and currents within a set grid in the simulation. These particles are then influenced by electromagnetic interactions of nearby charge densities/currents via Maxwell's equations; consequently giving the particles new positions and momentum within the simulation grid over some integrated time step.

OSIRIS is an example of such a PIC code, which was developed in Fortran 90 and uses object-oriented programming to divide the code into various objects which work coherently to complete the simulation. It also utilizes parallel computing techniques to divide several processes within the simulation to different CPUs simultaneously for increased computation speed.

4.1.1 Particle Meshing

Calculating all the interactions between particles within the plasma and proton driver would require large supercomputers, even with the use of parallel computing [20]. In order to reduce the computation time of the simulation code, one can use the particle-mesh method, whose methodology is as follows. Firstly, in order to decrease the amount of particles used for interactions, each particle in the simulation is actually representative of several particles within the plasma. We call this simulation particle a superparticle. The lack of complete individuality between particles is not so important, as we want to observe the general response of the plasma to external forces which should dominate more than individual particle interactions.

The forces of interaction between the particles also have to be implemented in this mesh. So the simulation is represented by an array of mesh points, in which fields act upon particles within a small time step Δt. First, the charge densities of the particles within this mesh-grid are collected at each point in the array. We can then solve Gauss's law to find the electric field and therefore the force on nearby particles. The forces then move the particles within the grid, creating charged currents. These

currents create magnetic fields, which also act on other particles. Over several time steps, these collective particles move due to self-consistent fields within the system, and their evolution over a certain amount of time steps, as well as the resultant electric and magnetic fields, can be observed.

4.1.2 PIC Equations

The basic Lorentz equation which generates force (and therefore movement) on the particles within the plasma is (in cgs units):

$$\dot{\mathbf{p}} = q\left(\mathbf{E} + \beta \times \mathbf{B}\right) \tag{4.1}$$

where $\mathbf{p}$ is momentum of the particle, $\beta = \frac{\mathbf{v}}{c}$ is the ratio of the velocity to the speed of light, q the charge of the particle, and $\mathbf{E}/\mathbf{B}$ is the electric/magnetic field acting on the particle.

Maxwell's equations are given below in cgs units

$$\nabla \cdot \mathbf{E} = 4\pi\rho \tag{4.2}$$

$$\nabla \times \mathbf{B} = \frac{1}{c}\frac{\partial \mathbf{E}}{\partial t} + \frac{4\pi}{c}\mathbf{j} \tag{4.3}$$

$$\nabla \times \mathbf{E} = -\frac{1}{c}\frac{\partial \mathbf{B}}{\partial t} \tag{4.4}$$

$$\nabla \cdot \mathbf{B} = 0 \tag{4.5}$$

with ρ and $\mathbf{j}$ the charge and current density. In order to update the fields within the simulation over some time steps, we only need to integrate Ampere's (equation 4.3) and Faraday's (equation 4.4) law. In this case, only the current density is required in order to advance these fields over time. By using these simple equations, integrating over many small time-steps, and implementing superparticles (the number of which is on the order of magnitude of 10^6) to represent the proton bunch and plasma electrons/ions, we can simulate the AWAKE experiment with OSIRIS.

4.2 Initial Parameters

The OSIRIS simulation version we use operates in a 2D coordinate system; with the coordinates being z the propagation axis, and r the radius normal to this axis. We assume that the plasma and proton bunch, which is roughly Gaussian in $\xi = z - ct$ and r, are cylindrically symmetric in the azimuth coordinate θ. The setup of the simulation is that the back-half of the proton bunch propagates through a plasma of ionized rubidium vapor. We simulate only half of the bunch because the ionizing laser will co-propagate along the middle of the bunch, creating a sharp cut-off which seeds the SMI. The other half moves through neutral vapor without interactions. The total propagation distance of the bunch is about 10 m of plasma, which will be at the constant density that we hope to achieve using the vapor source. The basic initial parameters of the simulation is listed in Table 4.1.

Table 4.1: Initial Parameters of the system.

Parameter, notation	**Value**
Plasma density, n_0	7×10^{14} cm^{-3}
Plasma ion atomic weight, M_i	85.5
Plasma length, L_{max}	10 m
Proton bunch length, σ_{zb}	12.6 cm
Proton bunch radius, σ_{rb}	0.2 mm
Proton bunch energy, W_b	400 GeV
Proton maximum density, n_{b0}	4×10^{12} cm^{-3}
Proton bunch population, N_b	1.5×10^{11}

The initial proton bunch density profile is represented by the equation

$$n_b = n_{b0} \times 0.5 \left[1 + cos\left(\sqrt{\frac{\pi}{2}}\frac{\xi}{\sigma_{zb}}\right)\right] \times e^{-\frac{r^2}{2{\sigma_{rb}}^2}} \tag{4.6}$$

$$-\sigma_{zb}\sqrt{2\pi} < \xi < 0,\ n_{b0} = \frac{N_b}{(2\pi)^{3/2}\sigma_{rb}^2\sigma_{zb}} \tag{4.7}$$

where the cosine term is supposed to be representative of a Gaussian function in ξ, and is used because it is computationally easier for simulations. It should be noted that σ_{zb} in this cosine function is not the same as the longitudinal rms bunch length. The rms value is initially about 11.4 cm.

OSIRIS uses normalized units for its simulations, and the units for distance is in $\frac{c}{\omega_{pe}}$. The size of the simulation grid, in which Maxwell's equations are calculated,

is chosen to fit the proton bunch within it. The appropriate size for this case was chosen to be 29.9892 cm in ξ and 0.1608 cm in r, which are multiples of $\frac{c}{\omega_{pe}}$. This grid is what moves through the plasma as the time increases within the simulations. For this bunch, the sharp cut-off is at $\xi = 0$ cm, whereas the rest of the bunch is at negative values in ξ.

Typically, a single simulation takes a bit more than 48 hours to run, and outputs file dumps every set interval in simulation time t. Due to the large amount of data given in such a file dump, the simulations were initially set to output about 50 file dumps, which is 50 propagation lengths of the proton bunch in the plasma. For each file dump, data such as the charge density of the simulated particles (protons, plasma electrons and ions) and electric/magnetic fields (in r, z, and θ) are given for values in r and ξ in the simulation grid.

4.3 Phase Analysis

We initially check the ORISIS code to make sure that it produces the expected results seen from other simulations ([18], [9], [13]). The simulation with the initial parameters in Table 4.1 shows the proton bunch undergoes SMI which produces micro-bunches near the propagation axis as it propagates through the plasma (see section A.6.1). Also, the on-axis longitudinal and perpendicular wakefields are approximately $\frac{\pi}{2}$ out of phase after the SMI process has stabilized at the end of the plasma (see section A.6.1). In addition, we observe similar results to previous simulations for peak E_z as a function of the propagation distance of the proton bunch (z), as seen in Figure 4.1, where E_z reaches peak value around 4 m, and then decreases afterward. These results show that the OSIRIS simulation generates expected outcomes when compared to previous simulations.

Our primary focus is on the wakefield phase velocity which varies during bunch propagation, until it stabilizes approximately after 4 m (see section 2.2.3). The regions of maximum $|E_z|$ in ξ after full SMI development is in the region of σ_{zb} (see Figure A.15). It is for this reason that we consider injecting the electron within this region in the AWAKE experiment. In Figure 4.2, we show the longitudinal and transverse wakefields in the region of ξ = -12 cm, about σ_{zb}, for various proton propagation lengths (z) into the plasma. We see that within this window in ξ, the wakefields shift backwards and then stabilize after about 4m of propagation as expected [18].

The wakefields interpreted in this thesis were averaged over $r = 0.03$ to 0.189 mm

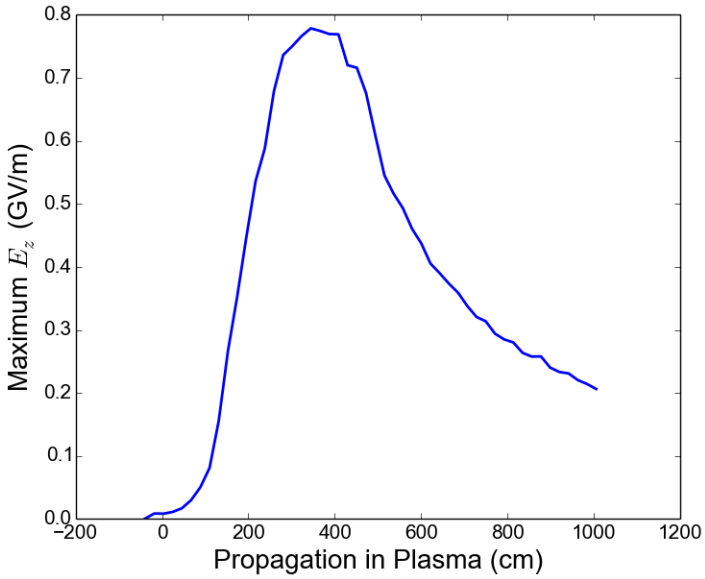

Figure 4.1: Peak accelerating $|E_z|$ for electrons as a function of propagation distance of the proton bunch within the plasma.

(within $\frac{c}{\omega_{pe}}$) in the simulation grid in order to get smoother wakefields as a function of ξ. This averaging is valid for our purposes since E_z does not vary much within this region of r, and we are still near enough to the z-axis to be considered on-axis. The transverse wakefields do vary within this averaging region, but in this chapter we only use the transverse fields to determine focusing/defocusing regions. Overall, we neglect fields at values less than $r = 0.03$ mm because they are especially noisy in this region.

To analyze the phase shift of these wakefields, we can fit a cosine function to E_z at a particular window in ξ. As E_z shifts in this window, the corresponding phase in the cosine fit also shifts. We select E_z for fitting because it remains more sinusoidal and symmetric about the z-axis than the transverse fields, especially near $z = 4$ m.

We fit E_z based on the equation $E_z = A\cos(k_p\xi + \phi)$, where $k_p = \frac{2\pi}{\lambda_{pe}}$ is the wavenumber and ϕ the phase offset. The fit allows for λ_{pe}, A, and ϕ to be variable parameters. The total phase, $k_p\xi + \phi$, is then recorded and translated to a phase shift starting at 0. One can also do the same by keeping λ_{pe} constant and allowing only the ϕ phase term to vary; which assumes λ_{pe} is roughly the constant theoretical value. The results for both vary by less than 0.01 rad (see section A.6.2), and so for generality, λ_{pe} is allowed to vary. Figure 4.3 shows examples of the phase shift of E_z

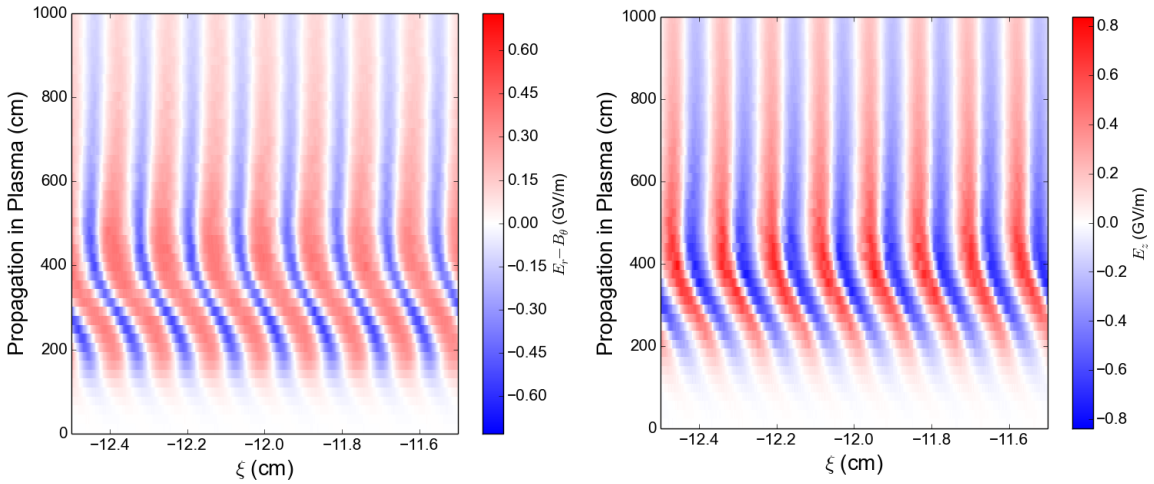

(a) Perpendicular Wakefield $E_r - B_\theta$

(b) Longitudinal Wakefield E_z

Figure 4.2: Plasma wakefields at regions around ξ = -12 cm for different propagation lengths of the proton bunch in the plasma.

as a function of z for different regions of ξ.

From Figure 4.3, we see that the phase shift of E_z has different curvature depending on which region in ξ we look at. It appears the best region for electron injection is around ξ = -12 cm not only because the magnitude of E_z is largest, but also because the slope in phase shift after 4 m of propagation is minimized and closest to 0.

We also see from Figure 4.3 that the phase shift of E_z has occasional little positive spikes in phase, which corresponds to a back-shift in the overall waveform in ξ. It also turns out that this happens periodically every 6-7 file dumps, regardless of the propagation distance between file dumps. Therefore, these spikes are independent of the actual propagation length within the plasma and consequently independent of the number of time-steps in the simulation. In addition, this phase spike corresponds to a shift in the smallest increment of ξ in the simulation grid, which corresponds to $0.013\lambda_{pe}$. The problem is not with the phase fitting routine (see section A.6.3). We do not yet know why this happens in the simulation, so to keep simulations consistent for comparison, we keep the total file dump number at 50, and will later gauge the effect of having more file dumps (see section 4.7).

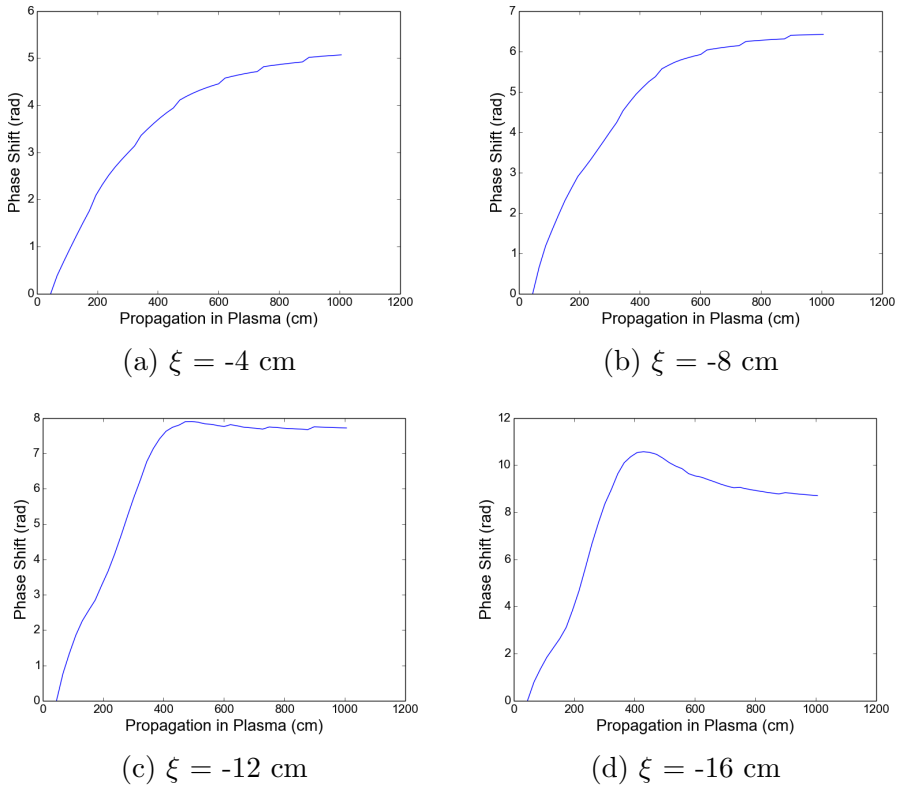

(a) ξ = -4 cm (b) ξ = -8 cm

(c) ξ = -12 cm (d) ξ = -16 cm

Figure 4.3: E_z phase shift about various ξ values as a function of propagation length of the proton bunch in plasma.

4.4 Changing Total Number of Protons

Simulations were run with the same parameters as in the initial case, but this time with the total number of protons in the bunch, N_b, changed by $\pm 5\%$. For this, we change the maximal charge density n_{b0} by $\pm 5\%$ in equation 4.6.

4.4.1 Wakefield Phase Difference

The respective phase shift of E_z for the region of ξ = -12 cm is shown in Figure 4.4 for simulations with the initial parameters and $N_b \pm 5\%$. We can see from this figure that the increase/decrease of N_b directly correlates with an increase/decrease in phase shift compared to the initial parameters case after $z \approx 3.5$ m. We also see that the difference in phase between $N_b \pm 5\%$ and the initial parameters is greater in the region of maximum E_z between 3.5 and 5 m. This phase difference gets smaller after the bunch has undergone SMI at the end of the plasma cell (which is also where

E_z decreases).

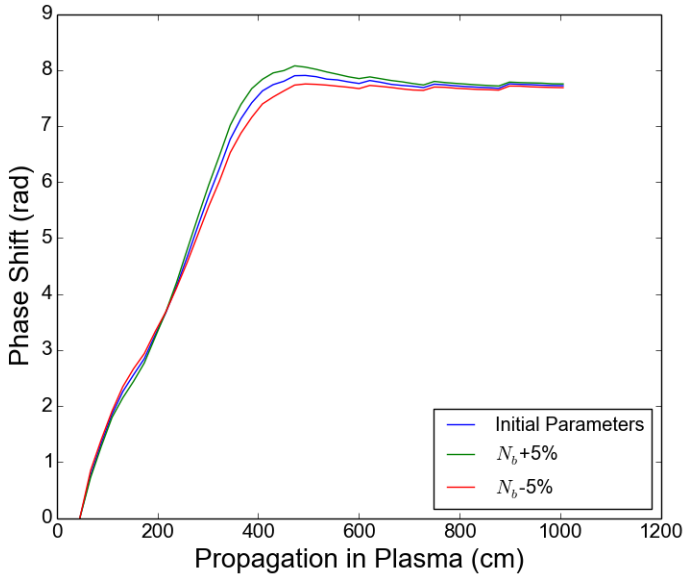

Figure 4.4: Phase of E_z for simulations with initial and N_b±5% parameters as a function of propagation length at ξ = -12 cm.

We can see how the SMI develops in Figure 4.5. The wakefields modulate the bunch density (which in this case is plotted as the density averaged within the skin depth $\frac{c}{\omega_{pe}}$), which results in further shifting of the wakefields. Looking at Figure 4.5a, we see that even initially, the front half of the bumps in density are within defocusing regions, whereas the back half is within focusing regions. As the bunch propagates within the plasma, the wakefields continually defocus and focus different regions of the bunch, leaving behind spikes in density within $\frac{c}{\omega_{pe}}$ which we call the micro-bunches. Looking at Figure 4.5b-d, we see that the front parts of these micro-bunches are in defocusing wakefields. This means that the peak density of the micro-bunches starts to move back in ξ as the front part is radially defocused, resulting in the generated wakefields, which are integrated over the bunch density, also shifting backwards in ξ. Consequently, the wakefields shift back in ξ during SMI development, until eventually they stabilize because the micro-bunches are contained in the focusing regions of the wakefields (at $z > 4$ m, not shown here).

We can imagine then that if N_b, and hence n_b, is increased, the wakefield magnitudes are also increased as they are proportional to n_b. This means that some micro-bunch around ξ = -12 cm for $z < 4$ m (still within SMI development) has the

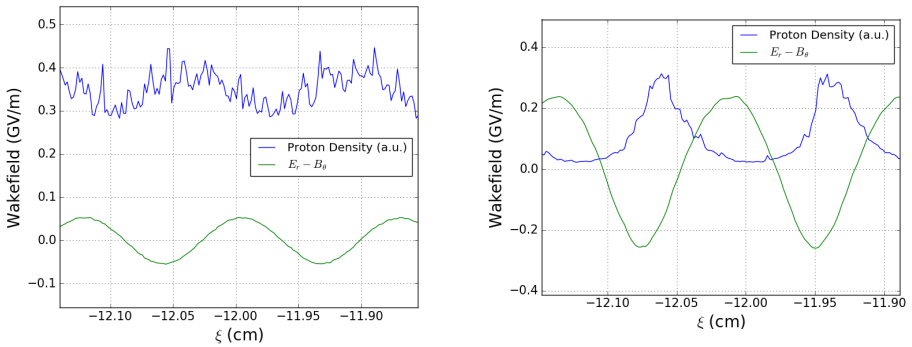

(a) z = 89 cm

(b) z = 153 cm

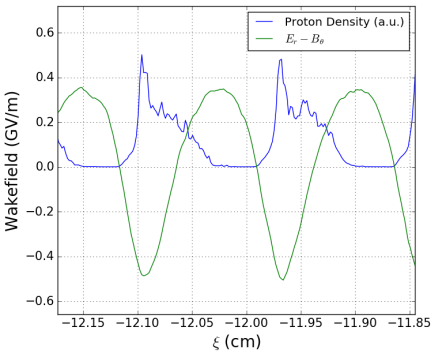

(c) z = 217 cm

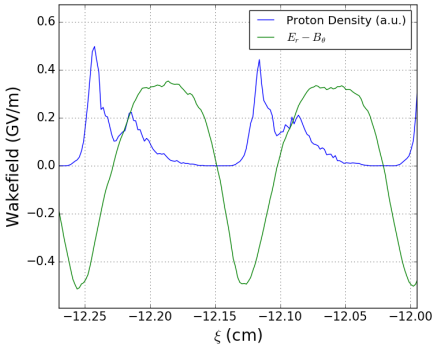

(d) z = 281 cm

Figure 4.5: The longitudinal wakefield and proton bunch density (in arbitrary units) for various propagation distances near ξ = -12 cm. Positive values of $E_r - B_\theta$ are defocusing for the protons.

front portion within larger defocusing regions, and the back portion within larger focusing, compared to the initial parameters case. As a result, the peak density of these micro-bunches move further back in ξ in a shorter propagation distance, thus moving the generated wakefields further back as well. This is why the wakefields move further back in ξ (which means a positive phase difference) for N_b+5% than in the initial case. The wakefields for N_b-5% are therefore relatively shifted forward in comparison by the same reasoning.

For future experiments, we want to make sure that the electrons can be injected into regions of focusing/acceleration. This region is typically within a quarter wavelength of E_z, or $0.25\lambda_{pe}$ (see section 2.2.2). For z between 4-5 m, the average difference in phase for N_b±5% compared to initial parameters is about ±0.19 rad. This corresponds to a shift of $0.03\lambda_{pe}$. If we assume the electron will be injected in the center of the focusing/accelerating region, then we have a $0.125\lambda_{pe}$ leeway on the position

of the electron bunch about this point. Therefore, for total proton bunch number within N_b±5%, the phase will not differ significantly enough for electrons to drift outside of some focusing/accelerating region. In addition, between 6-10 m the average phase difference reduces to $\pm 0.008\lambda_{pe}$, as the bunch has formed into evenly-spaced micro-bunch trains within this region. So this bunch stabilization after about 6 m of propagation causes the phase of E_z to converge to that of the initial parameters.

We also gauge the phase difference between N_b±5% and the initial parameters run at other regions in ξ for z between 4-5 and 6-10 m. The same analysis as previously described is done, but this time at different regions in ξ, while also taking note the standard deviation in phase difference for these regions. The plot of the mean phase differences, in terms of fraction of λ_{pe}, as a function of ξ are shown in Figure 4.6, where the error bars are the standard deviation in phase difference. We use fraction of λ_{pe} for simplicity as we want to make sure the difference is within $0.125\lambda_{pe}$, or half the optimal (focusing/accelerating) region for an electron.

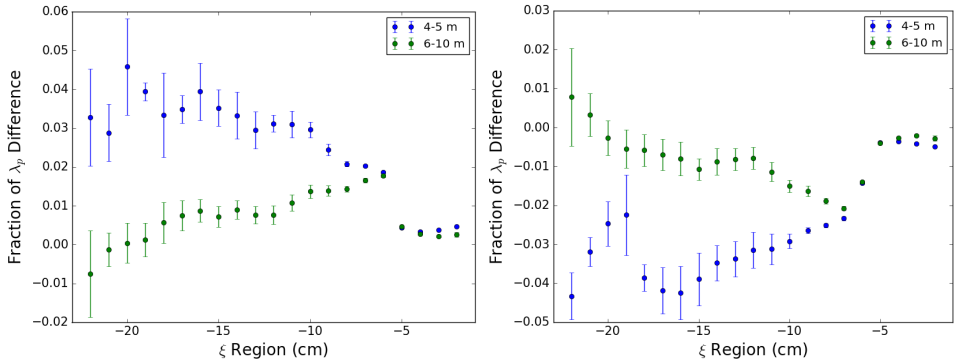

(a) For N_b+5% (b) For N_b-5%

Figure 4.6: Mean phase difference (in fraction of λ_{pe}) as a function of ξ between simulations of N_b±5% and initial parameters for z of 4-5 and 6-10 m. Error bars are standard deviations of phase difference.

For propagation lengths of 4-5 m, the region of peak E_z, the phase difference is greater than 6-10 m regardless of region in ξ. This means that for changes in N_b considered, the phase of E_z will regardless tend to converge to that of the initial parameters case for $z > 6$ m. As a consequence, the effect of N_b±5% on the phase difference in the region of 4-5 m is more important for all ξ values.

Near ξ = -12 cm, the phase difference at 4-5 m is still well within $0.125\lambda_{pe}$. For all other ξ regions, the phase difference is less than $0.05\lambda_{pe}$. As a result, for a tolerance

of $N_b \pm 5\%$, we could inject electrons in the middle of any focusing/accelerating region in ξ, and not worry about them shifting to defocusing/decelerating regions.

4.4.2 Energy Gain of Injected Electrons

Regardless of N_b, the phase of E_z is not constant for $z > 4$ m, even at ξ = -12 cm. This means that the optimal region for electron injection may be reduced as the electron propagates with the proton bunch. It is useful then to find, for some region in ξ near -12 cm, at what injection point in z an electron will be focused/accelerated until $z = 10$ m. We call this the minimum injection point. We then want to see how varying $N_b \pm 5\%$ will affect the minimum injection point.

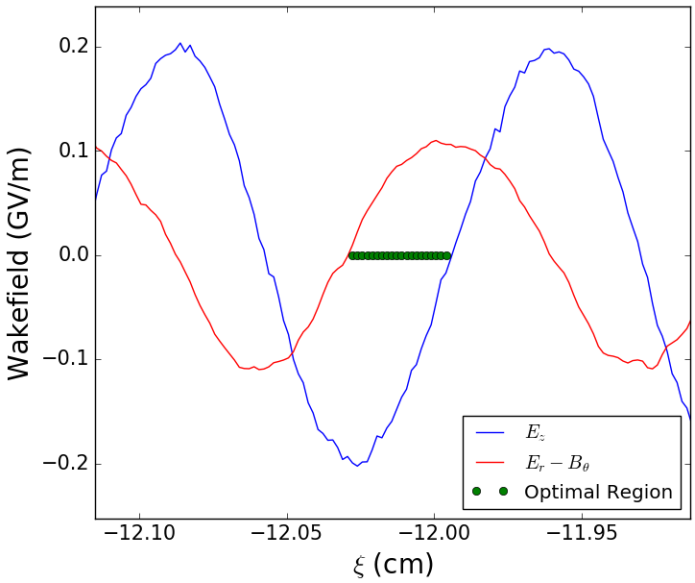

Figure 4.7: Shown are the longitudinal (E_z) and perpendicular ($E_r - B_\theta$) wakefields, as well as an optimal region of focusing/accelerating for electrons at $z = 10$ m.

We first find a region of focusing/acceleration at $z = 10$ m for the initial parameter case, which is shown in Figure 4.7. The optimal region is about $0.25\lambda_{pe}$ at this point, as expected. This shows that after the SMI has fully broken up the proton bunch, E_z and $E_r - B_\theta$ will more closely follow linear theory (see section 2.1.2), and so are more sinusoidal and $\frac{\pi}{2}$ out of phase. However, the focusing portion of the transverse wakefield is still a bit larger than the defocusing portion. This is especially true for regions of SMI development, where the transverse fields have much larger regions of focusing than defocusing for electrons (see Figure 4.2a).

For each ξ point in the optimal region, we find the minimum injection point, so that an electron stays within focusing/accelerating fields for z greater than this minimum injection point. We then repeat for the same optimal region in ξ with N_b±5%. The minimum injection length for each ξ in the optimal region is shown in Figure 4.8, for the initial and N_b±5% parameter runs.

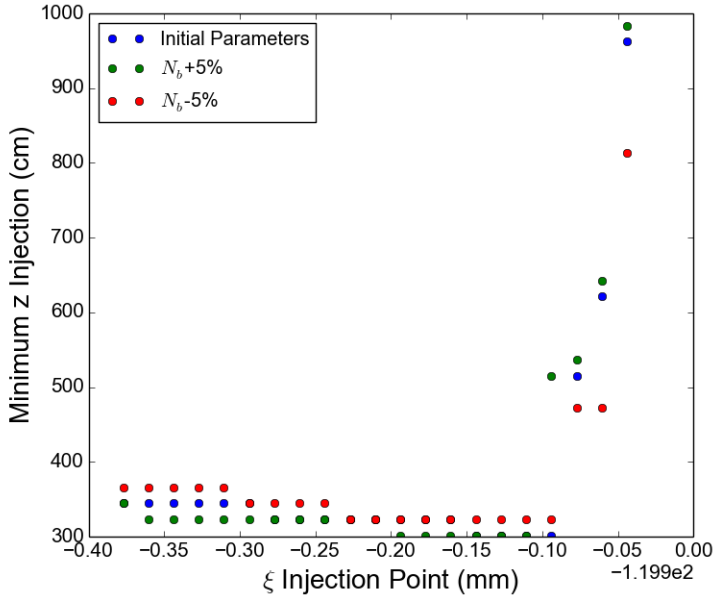

Figure 4.8: Minimum injection point of electrons so they remain in focusing/accelerating fields until z = 10m. Shown for focusing/accelerating region nearest ξ = -12 cm at z = 10 m

Looking at Figure 4.8, a good injection point which includes the majority of the minimum injection points is about 4 m. By choosing to inject at around 4 m, the new optimal region in ξ at which we can get focusing/acceleration is limited to $0.21\lambda_{pe}$. If we compare the minimum injection point for the initial parameters and N_b±5%, only one ξ point is excluded for the optimal region at 4 m injection points. So overall, the dominant issue in remaining within the optimal region is the phase shift of E_z between 4-10 m, not the difference in phase from variations in N_b.

However, the change in N_b might affect the overall gain in energy for an electron injected at 4 m within this new optimal region in ξ, as $E_z \propto n_b \propto N_b$. The energy

gain of an electron in this case can be estimated by:

$$\text{Energy Gain} = \int_{4m}^{10m} eE_z dz$$

We would therefore expect that an increase/decrease in N_b results in an increase/decrease in energy gain.

In Figure 4.9, the energy gain of an electron injected at $z = 4$ m for the initial and N_b±5% cases in the new optimal region is shown. We see that in general, the energy gain is higher for lower values of ξ in this optimal region. This is because the peak accelerating fields are located near the back (left-most) part of the optimal region (see Figure 4.7). This is one of the advantages of wakefields shifting forward in ξ after 4 m; for as E_z shifts forward, an electron in the middle of the optimal region moves towards the peak accelerating field, creating a larger energy gain than in the constant case.

There is also a correlation between energy gain in the initial case, and difference in energy gain from this case due to a change of N_b±5%. At points in ξ near peak $|E_z|$, the interval of energy gain for N_b±5% is smaller than for regions of ξ near $E_z = 0$. This means that if one is able to precisely inject electrons near peak $|E_z|$, a small change in N_b will not result in a large change in energy gain. The maximum/minimum energy gains for the run with initial parameters are 2.11/0.64 GeV respectively. At minimum energy gain, the energy for N_b+5% is 0.57 GeV, whereas for N_b-5% it is 0.75 GeV. So the largest difference in energy gain between the initial and either N_b±5% cases is about 0.11 GeV, or 17%.

We also notice that for N_b-5%, the energy gain is generally higher, even though in linear theory the strength of E_z is directly proportional to N_b (see equation 2.3). By looking at Figure 4.4, we see the phase of E_z is generally lower for N_b-5% compared to the other cases. This means that E_z is relatively shifted forward in ξ in comparison, and thus the electron is closer to peak $|E_z|$ for N_b-5%. This further shows that the E_z phase change after $z = 4$ m in the initial case has more impact than N_b changing by ±5% on energy gain.

4.5 Changing the σ_{rb} and σ_{zb} Parameters

We want to extend the previous analysis for changes of σ_{rb}±5% and σ_{zb}±5% to the initial proton bunch. To make these variations independent of each other and N_b,

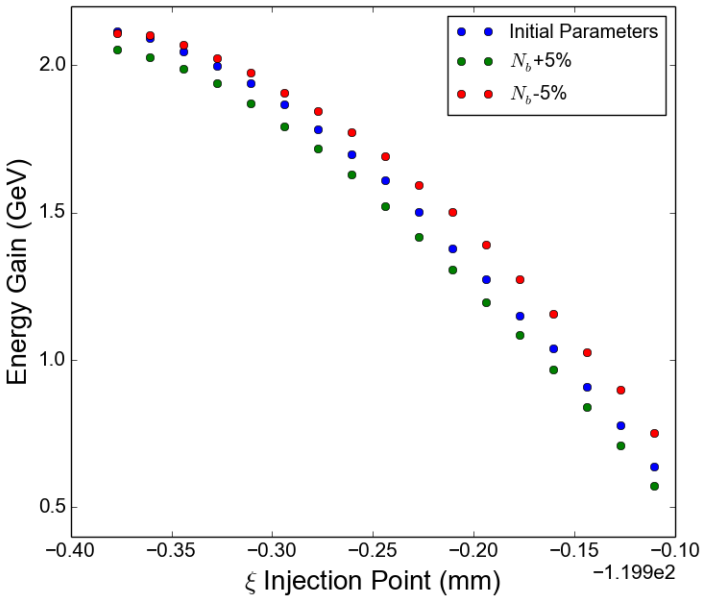

Figure 4.9: Energy gain of injected electrons for $z > 4$ m as a function of ξ in the optimal region for initial and N_b±5% runs. Shown for optimal region near ξ = -12 cm

we have to decrease n_{b0} when increasing these parameters by +5%, and respectively increase it when decreasing these parameters.

The phase of E_z vs z for these parameters are shown in Figure 4.10. In these cases, we see that an increase in either σ_{zb} or σ_{rb} corresponds to a negative phase difference, and a decrease corresponds to positive phase difference. This is the opposite effect than what we see with the N_b variations. This implies that the phase shift of the wakefields is directly correlated to the density of the proton bunch, since $n_b \propto \frac{N_b}{\sigma_{zb}\sigma_{rb}^2}$. As seen with the changes in N_b, the phase differences are still greatest at regions of z = 4-5 m, and is reduced as we go to 10 m.

In Figure 4.11, the phase differences (in terms of λ_{pe}) are plotted as a function of ξ for 4-5 and 6-10 m propagation lengths. Again, the maximum phase difference is in the region of 4-5 m for all ξ. The maximum mean phase difference (along with its standard deviation) at ξ = -12 for σ_{zb}±5% is 0.026±0.004 λ_{pe}. For σ_{rb}±5%, it is 0.019±0.006 λ_{pe}. So at ξ around -12 cm for variations in both σ_{rb} and σ_{zb}, the phase difference is below $0.03\lambda_{pe}$. The overall phase difference along all ξ still remains within $0.125\lambda_{pe}$, and so we can safely inject electrons in the middle of the optimal region assuming tolerances of ±5% in the initial bunch parameters. In general, the

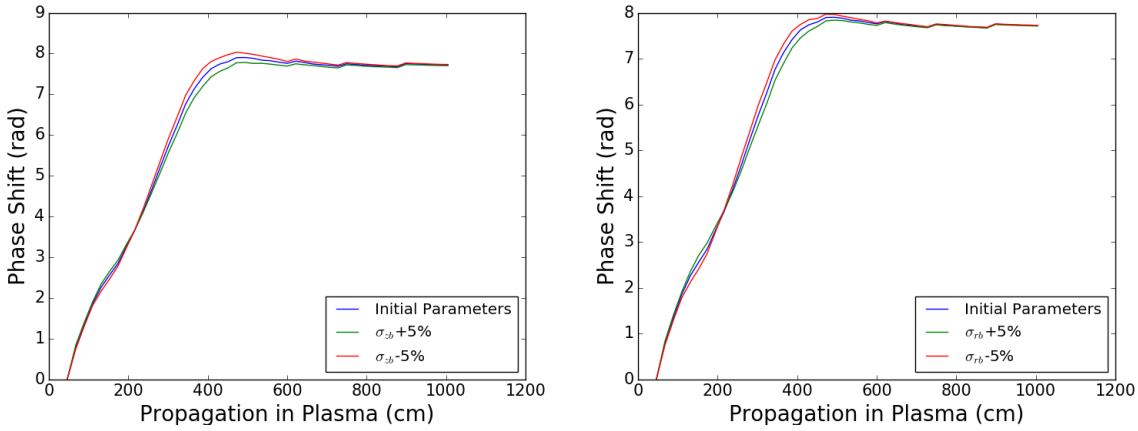

(a) With σ_{zb}±5%

(b) With σ_{rb}±5%

Figure 4.10: Phase of E_z vs propagation length for initial parameters, σ_{zb}±5%, and σ_{rb}±5% at ξ = -12 cm.

mean phase difference is at maximum for N_b±5%, and minimum for σ_{rb}±5%. So changing N_b has the most impact on the wakefield phase-velocity shift compared to other physical parameters of the proton bunch.

Figure 4.12 shows a plot of the minimum injection point for the cases of σ_{rb}±5% and σ_{zb}±5% in the optimal region of focusing/acceleration near ξ = -12 cm. The region of allowed injection at 4 m is again only changed by about one point in ξ between the initial and σ_b±5% (σ_b being either σ_{zb} or σ_{rb}) cases. This reaffirms that small changes in initial bunch parameters do not strongly affect the allowed region in which electrons need to be injected. For σ_{zb}±5%, the optimal region is within $0.21\lambda_{pe}$. For σ_{rb}±5%, the injection region is within $0.22\lambda_{pe}$, which also confirms that for the same percent tolerances on the physical parameters of the initial proton bunch, the change in σ_{rb} is the least significant near ξ = -12 cm.

The energy gain for electron injection at 4 m, when considering each σ_b±5%, are shown in Figure 4.13. We see that the highest energy gain between 4-10 m is generally when the σ_b parameters are increased by 5%. This is for the same reason as in the N_b-5% case, for when σ_b is increased, the phase of E_z after 4 m is reduced compared to the initial parameters case. This causes the electrons to shift towards regions of higher $|E_z|$.

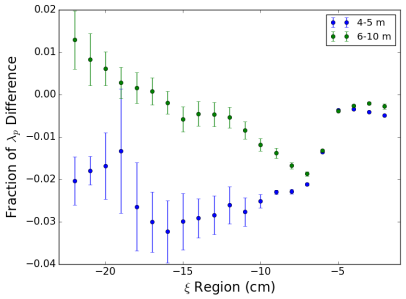

(a) σ_{zb}+5%

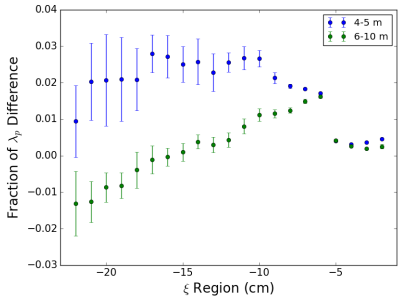

(b) σ_{zb}-5%

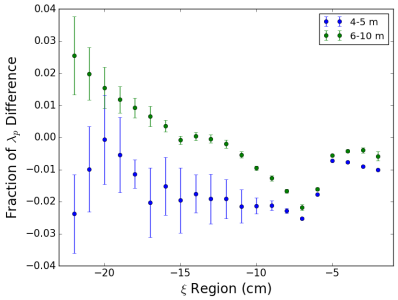

(c) σ_{rb}+5%

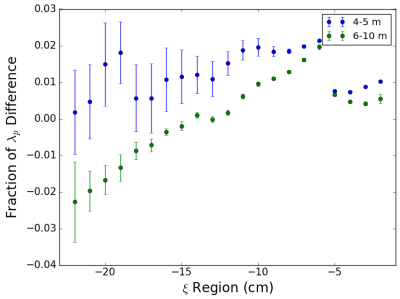

(d) σ_{rb}-5%

Figure 4.11: Phase difference (in fraction of λ_{pe}) as a function of ξ for σ_{zb} and σ_{rb} $\pm$5% compared to the initial parameters. Phase difference shown for z between 4-5 and 6-10 m. Error bars are standard deviations of phase difference within these propagation distances.

4.6 Overall Variation Effects at Nearby ξ Injection Points

As of now, analysis was done at ξ = -12 cm because at this value, we are near the maximum $|E_z|$ and in a region of relatively constant phase-velocity after 4 m propagation, both of which are desired for injection experiments. However, it may be that the best location in ξ for injection is rather broad. Therefore, it is interesting to look at two important variables for injection at other ξ values nearby: the size of the optimal (focusing/accelerating) region for electrons injected at 4 m, and the maximum energy gain of these electrons.

For each parameter variation tested (N_b, σ_{zb}, and σ_{rb}), we plot the size of the optimal regions (in terms of λ_{pe}) for various ξ injection points. This is shown in Figure 4.14. For all considered bunch variations, the largest optimal region is at ξ = -11.5 cm, which is near the actual longitudinal rms value of the bunch at -11.4

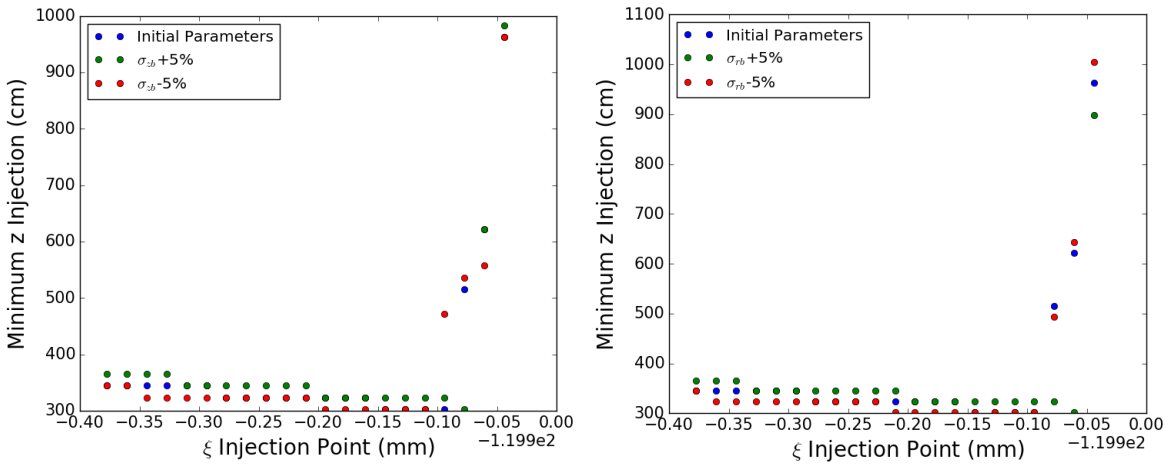

(a) With σ_{zb}±5%

(b) With σ_{rb}±5%

Figure 4.12: Minimum injection length of electrons so they remain in focusing/accelerating fields. Shown for optimal region near ξ = -12 cm with parameter changes in σ_{zb} and σ_{rb}.

cm. In general, the size of the optimal region for variations in N_b and σ_{zb} are similar, with the largest deviations coming from variations in σ_{rb}. We see that the size of the optimal region is reduced more significantly in the direction of $\xi = 0$ cm.

In Figure 4.15, we plot the maximum energy gain for the different parameter changes as a function of ξ injection points. Once again, this is for electrons injected at $z = 4$ m. We see that the best locations for maximum energy gain are also around ξ = -11.5 or -12 cm. The maximum energy gain falls fairly quickly towards $\xi = 0$ cm, whereas the drop-off is slower for lower values of ξ.

It is clear from Figures 4.14 and 4.15 that the best regions in ξ for electron injection, regardless of which parameter is changed by ±5%, is for -12 cm $\leq \xi \leq$ -11.5 cm. This is near σ_{zb} and the longitudinal rms bunch length as previously expected. So the best region in ξ in which to inject electrons remains unchanged for these parameter variations.

4.7 N_b Comparison with Different Number of Intermediate Steps

Due to the phase spikes produced by OSIRIS as seen in the phase plots of E_z vs z, it is important to test how simulation results change when the number of dumps is

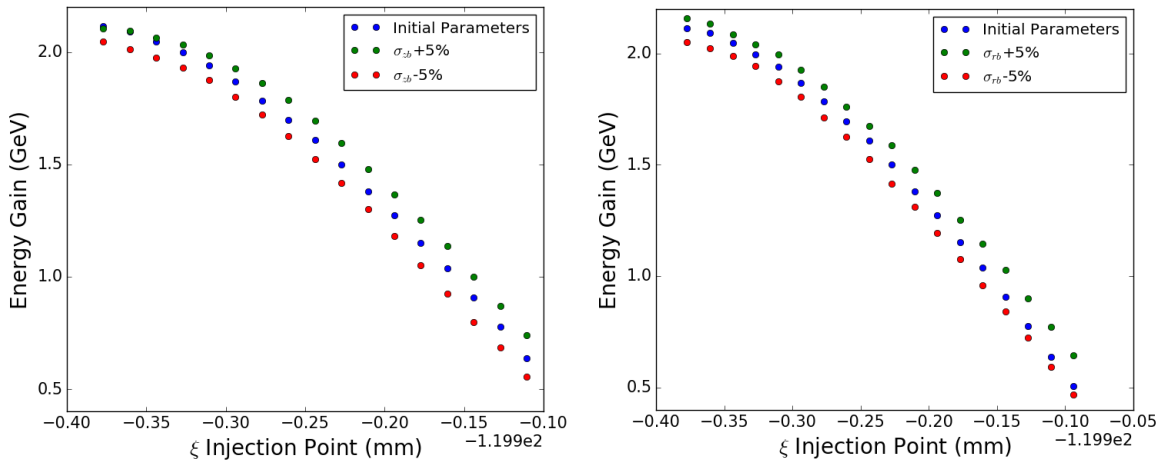

(a) With σ_{zb}±5%

(b) With σ_{rb}±5%

Figure 4.13: Energy gain of injected electrons injected at z = 4 m as a function of ξ in the optimal region for initial and σ_{zb}±5% and σ_{rb}±5% runs. Shown for optimal region near ξ = -12 cm

changed, and so the simulation was run for 99 file dumps instead of 50, using the N_b±5% case as an example. We show an example phase plot for the initial parameter runs with 50 and 99 file dumps in Figure 4.16, as well as the phase plots of N_b±5% for the 99 dump simulations. We see from Figure 4.16a that the phase spike happens at every 6-7 file dumps, regardless of how many file dumps are outputted. It seems that for the 99 file dump case, the slope of the points between phase spikes is nearly double that of the 50 dump case, suggesting an internal error which is independent of the dump size and is corrected every 6 -7 dumps. In Figure 4.16b, we see that the phase plots for each N_b parameter case follows the same trends as in the 50 dump simulations seen in Figure 4.4.

We want to make sure that phase difference between the initial and N_b±5% parameters remains unchanged. The mean phase differences in fraction of λ_{pe} are shown in Figure 4.17 for both the 50 and 99 dump simulations. We see that the phase differences for both dump sizes remains the same at smaller values of $|\xi|$, but starts to diverge at larger $|\xi|$. However, around ξ = -12 cm, we still see that the phase difference remains around $\pm 0.03\lambda_{pe}$ for both cases. As a result, regardless of the file dumps size, the phase difference is within the $0.125\lambda_{pe}$ allowed for an electron injected at the center of some focusing/accelerating region.

We also want to see if simulation dump size changes the best region in ξ for

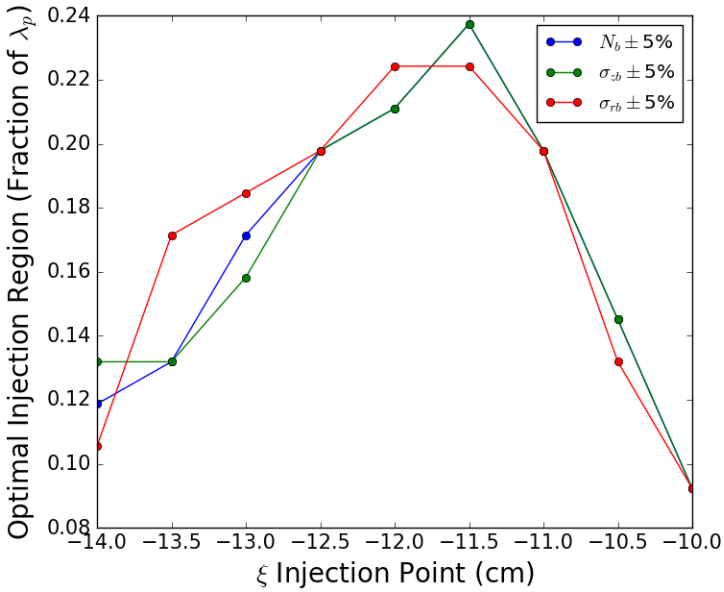

Figure 4.14: Size of optimal region, in fraction of λ_{pe}, for an electron injected at z=4 m for different locations in ξ. The size of the region is the maximized allowed for variations in N_b, σ_{zb}, or σ_{rb} by $\pm$5%.

injection of electrons at z = 4 m, while taking into consideration the variations of N_b. To determine this, we again plot the size of the optimal region and maximum energy gain for ξ values near -12 cm. As usual, these values are for electrons injected at z = 4 m. These are plotted for $N_b\pm$5% for the 50 and 99 file dump cases in order to compare how the dumping frequency might change these results. The plots are shown in Figure 4.18.

We see from Figure 4.18 that the maximum optimal region size and energy gain still occur at ξ = -11.5 cm, independent of dump size. For both Figure 4.18 a and b, the plots for 50 and 99 file dumps also follow the same trend. The reason that the maximum energies in Figure 4.18b are higher for the 99 dump case is likely because the phase E_z has larger negative slopes, as seen in Figure 4.16, resulting in more shifts towards peak $|E_z|$.

From these results, we conclude that regardless of the dumping frequency used in the simulations, we can still say that $N_b\pm$5% (and likely the same for the other parameters) variations in the initial parameters will not have a significant impact on future electron injection experiments. However, this problem in OSIRIS needs to be understood and fixed before doing further studies on this subject to get rid of any

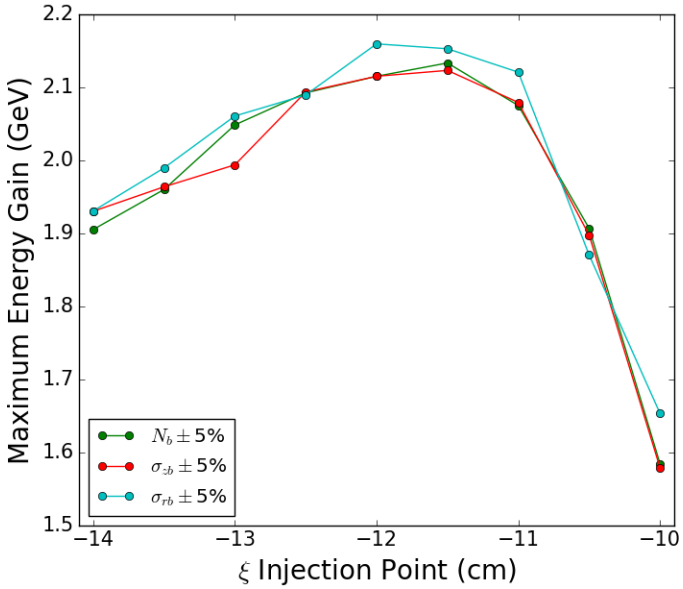

Figure 4.15: Maximum energy gain of electron injected at z=4 m for different locations in ξ. Maximum energy gains are shown for allowed variations in N_b, σ_{zb}, and σ_{rb} by $\pm 5\%$.

uncertainty.

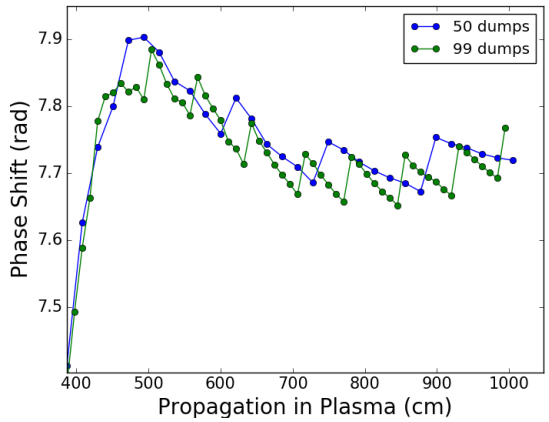

(a) Initial parameters case for 50 and 99 file dumps

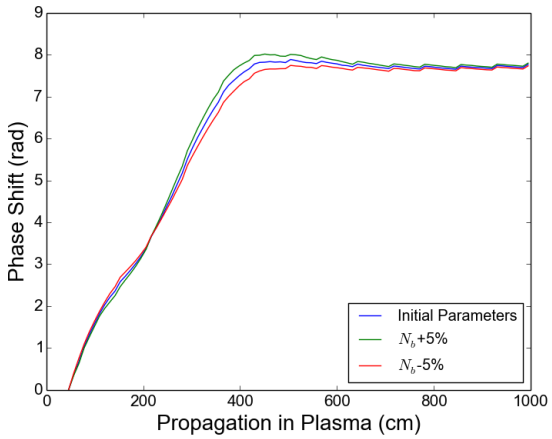

(b) Initial and $N_b \pm 5\%$ case for 99 file dumps

Figure 4.16: Phase of E_z as a function of propagation length. In **a)**, we see it for the initial parameters case with 50 and 99 file dumps. In **b)**, we see it for initial and $N_b \pm 5\%$ case for 99 file dumps.

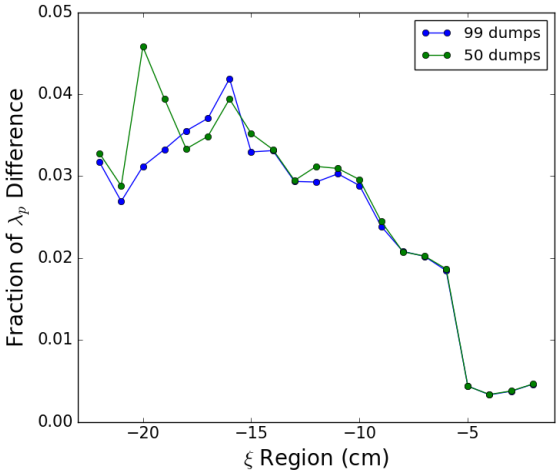

(a) Phase difference between N_b+5% and initial case

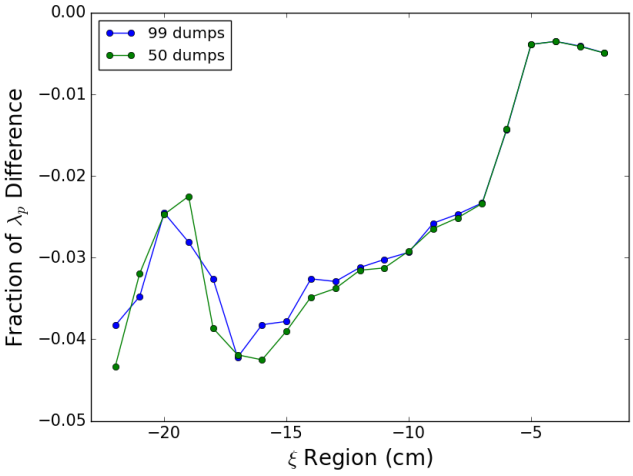

(b) Phase difference between N_b-5% and initial case

Figure 4.17: Phase difference of E_z as a function of ξ between $N_b \pm 5\%$ and initial parameters case. Shown for 50 and 99 file dump simulations.

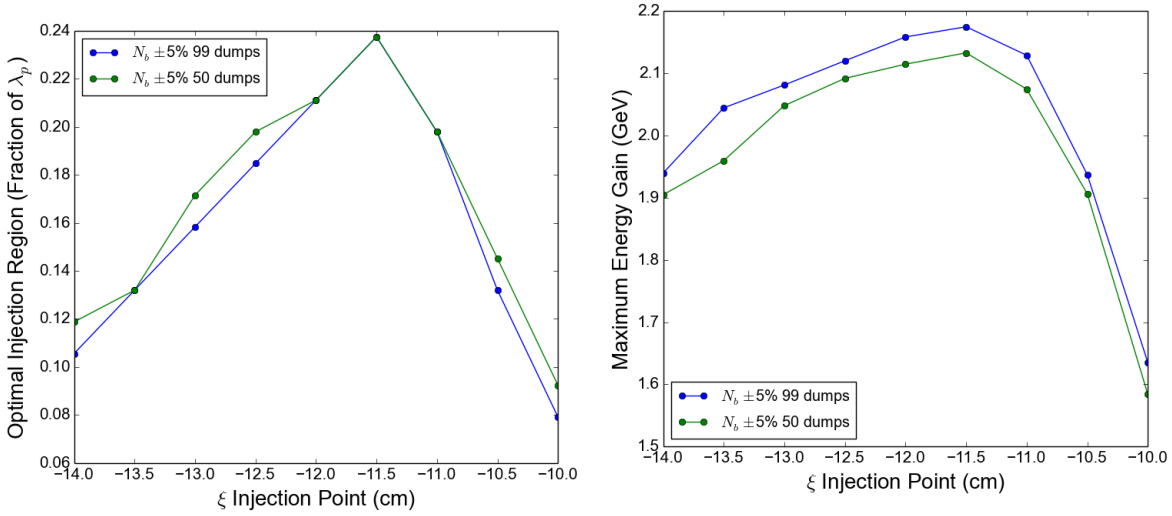

(a) Optimal region size for 50 and 99 dumps

(b) Maximum energy gain for 50 and 99 dumps

Figure 4.18: Optimal region size and maximum energy gain as a function of ξ for electrons injected at $z = 4$ m, taking into consideration variations of $N_b \pm 5\%$. Shown for simulations with 50 and 99 total file dumps.

Chapter 5

Conclusion

5.1 Thermal Uniformity

5.1.1 Vapor Source Results

A 3 m heat-exchanger (known as the 3m source) was tested using Galden HT270 as the heat-exchanging liquid. By using relatively calibrated Pt111 temperature probes, we measured the temperatures along the pipe to be within 0.2% for liquid temperatures of about 180°C. This meets the AWAKE requirement of keeping rubidium vapor density, and therefore also plasma density, within 0.2%.

In order to get a sharp drop-off in vapor density at the ends of the vapor source, we expect to attach another small heat-exchanging system and an expansion volume, in which rubidium vapor flows into from the pipe and condenses onto its walls. To represent the design co-created by the engineering company WDL and MPP, a smaller heat-exchanger and a steel disc were attached to the end of the 3m source. It was shown using temperature measurements within the pipe that these extra components generate sources of heat-loss which disrupts the temperature uniformity.

In order to fix this problem, it was determined that external electrical heating will have to be implemented to retain temperature uniformity. We showed using simple electrical heating tapes that external heat sources can offset the heat loss from the end pieces to maintain the desired temperature uniformity. We also showed that these external heat sources will increase the temperature of the disc, and therefore the expansion chamber, to temperatures above the rubidium melting point. Consequently, cooling will also have to be implemented to the expansion chamber design to lower the temperature sufficiently for rubidium condensation.

The largest issue with these experiments came from the unknown uncertainty in the probe measurements. The probes were not as well calibrated as intended, making the actual error in measurements between different probes hard to evaluate. In the future, it might be best to either use pre-calibrated probes, or include more temperature points and wait longer for equilibrium when performing the calibration. Also, due to the thin leads of the probes and the wires to which they were soldered, the soldering connections were easily detached by vibrations in the 3m source. This resulted in having to dismiss certain probe measurements due to their faultiness.

5.1.2 Goals for Vapor Source

With help from the experiments presented in this thesis, WDL has designed what we name the Vapor Source Ends, which will eventually be attached to the ends of the 10 m vapor source at CERN. The design includes the use of electrical heaters around the connection between the heat-exchanger and the Ends, as well as electrical heaters placed radially on the disc of the expansion chamber, to offset heat losses respectively through the flange-connections and expansion chamber. At the outer radius of the expansion chamber, circumferential liquid cooling is applied to cool the rest of the chamber to about 28°C for rubidium condensation.

With this design in mind, WDL hired a company to perform thermal simulations based off this design, which provided positive results in maintaining temperature uniformity along the axis of the pipe, along with a sharp drop-off at the expansion chamber. The ends include windows for white-light interferometry which will be used to measure the vapor density gradient between both ends of the vapor source. This will allow us to observe how stable the rubidium density is within the pipe.

5.2 OSIRIS Simulations

5.2.1 Results of Changing Initial Proton Bunch Parameters

As the proton bunch undergoes self-modulation within the plasma, the phase velocity of the generated wakefield changes until eventually reaching the velocity of the proton bunch after about 4 m of propagation. For AWAKE, in order to test the potential of these wakefields, electrons will be injected and accelerated at regions of both focusing and acceleration. To prevent the electrons from moving out of these regions, the

electrons will have to be injected after 4 m of propagation when the wakefield phase velocity remains roughly constant.

Using the PIC code OSIRIS, we simulated the AWAKE experiment by propagating a proton bunch through about 10 m of plasma at the optimal density. The initial proton bunch parameters used were representative of the SPS proton bunches that will be utilized in AWAKE. We also ran simulations with the bunch parameters N_b, σ_{zb}, and σ_{rb} changed by $\pm 5\%$ to observe how these potential changes would affect future electron injection experiments. We found that these variations do change the phase of E_z along ξ compared to the initial case. These phase differences compared to the initial case occur at or less than $0.03\lambda_{pe}$ at the region of ξ = -12 cm, the region considered for injection due to maximized $|E_z|$ and flat E_z phase after 4 m of propagation. This is well within the region of focusing/acceleration in ξ which is generally $0.25\lambda_{pe}$. We also find that the wakefield phase shift is correlated with the density of the proton bunch, which is itself related to the bunch parameters by $n_b \propto \frac{N_b}{\sigma_{zb}\sigma_{rb}^2}$. When n_b is increased, the phase of the wakefield shifts further back in ξ, whereas when it is decreased, the phase shifts further forward.

We also found that the optimal injection point for electrons after 4 m propagation length, after taking into consideration all parameter changes, is reduced to less than $0.22\lambda_{pe}$ due to the slight change of the E_z phase after 4 m propagation length. The energy gain of electrons within this optimal injection region does not change significantly for the studied variation in the bunch parameters. For portions of the optimal injection region in ξ that are in weaker $|E_z|$, the energy gain difference between varied parameters and the initial case is larger. As a result, if we can inject electrons near the peak $|E_z|$, variations in proton parameters would have smaller changes in electron energy gain, and we would get the higher energy gain desired. The best location for electron injection at $z = 4$ m, which maximizes energy gain and the size of the optimal region regardless of which parameters are changed, was shown to be -12 cm $\leq \xi \leq$ -11.5 cm. This means that the best injection point in ξ, considered to be around σ_{zb}, also remains independent for these parameter deviations.

5.2.2 Future OSIRIS Simulation Work

Looking ahead, the first thing that will have to be done is to fix the bug in OSIRIS which generates strange phase spikes in the wakefields every 6-7 file dumps. Secondly, it is possible that the parameters of the SPS bunch may change by more than $\pm 5\%$,

so one could continue these studies and see how more drastic changes in initial parameters would affect the wakefield phase. By doing this, we could eventually impose a maximum tolerance on the proton bunch parameters for the experiment. Lastly, we could account for changes in other bunch parameters, such as variations in the location of the co-propagating laser pulse along the proton bunch, or bunch emittance, and see what impact they would have on electron injection experiments.

Appendix A

Additional Calculations, Analysis, and Figures

A.1 Pt111 Temperature Probes

When making measurments for temperature uniformity for the 3m source, we need to measure potentially up to 250°C. Commonly used sensors which can be conveniently calibrated using stirred oil baths include platinum resistance probes. These rely on the intrinsic temperature vs resistance relationship in platinum. They are basically composed of a piece of platinum with a constant current running through them. By measuring the voltage across the platinum piece with a known current, we can get the resistance of the platinum piece. The resistance of this platinum piece and the ambient temperature of the platinum has a standard linear relationship up to 660°C. These can therefore be used for our purposes as we want to measure temperatures in the 150-230°C range [21].

Fifteen platinum resistance probes, called Pt111s, were bought and initially had to be soldered to approximately 3 m long, thin wires using two-lead connections. These were then connected via two 32-pin connectors to a Lakeshore Model 218 Temperature Monitor [22], which can read out the resistances of these sensors. Consequently, the resistances can be turned to temperature read-outs using the standard Temperature-Resistance relationship of platinum resistors.

Unfortunately, the temperature readings of each probe are only interchangeable within about ±0.4 K near 200° [21]. We can, however, do a relative calibration of the probes within the stirred-liquid bath, which means that we calibrate the probes to a

pre-defined temperature scale. This means the probes won't accurately read absolute temperature measurements, but at the moment we care more about keeping the temperature/density constant than having an absolute value of temperature/density.

A.1.1 Pt111 Relative Calibrations

The liquid bath itself has a thermal sensor which it uses to set the temperature of the Silicone Oil inside it. This sensor is independent of the Pt111 measurements, and is referred to as the bath temperature T_{bath}. In this case, bath temperatures were chosen between ambient temperature (24.4°C) and 220°C for calibrating the probes.

The Pt111 probes were placed in contact with each other within a copper cylinder so that they would, in principle, be at the same temperature. The copper cylinder containing the probes was placed within the Silicone Oil inside the bath. A Labview program was created which could take resistance read-outs from the Lakeshore Monitor, and record them as a function of time. While recording the resistances, the program also presented live updates of the resistance vs time measurements on a graph. The bath would be set to a certain temperature, after which the probe resistances were monitored until they reached equilibrium, or when resistances remained constant with time. After a stable equilibrium was reached, the bath temperature could be raised again, and the procedure repeated until a bath temperature of 220°C was reached. The initial temperature was at ambient temperature, after which it was set to $T_{bath} = 40$°C. The temperature was then raised by intervals of 20°C up to 160°C, then raised in intervals of 10°C up to 220°C. An example of the resistance vs time curves of the probes is shown in Figure A.1.

Minimizing density perturbations, and therefore temperature variations, is of greater importance than absolute measurements, and so we relatively calibrate the probes to measure temperatures within an interval of 0.1 K. To do this, we must first establish a standard temperature for each stable region in Figure A.1. It was decided that instead of using the bath temperature for this purpose, the temperature corresponding to the standard temperature vs resistance curve for Pt111 probes would be used. This was done since we do not know the accuracy of the bath sensor, whereas we at least know the general accuracy of a Pt111 probe using the standard curve. As a result, the average resistance of all the probes at each plateau was calculated, and then converted to temperature using the standard curve. We'll call this temperature scale the standard temperature, T_S. We can now calibrate each probe to this standard

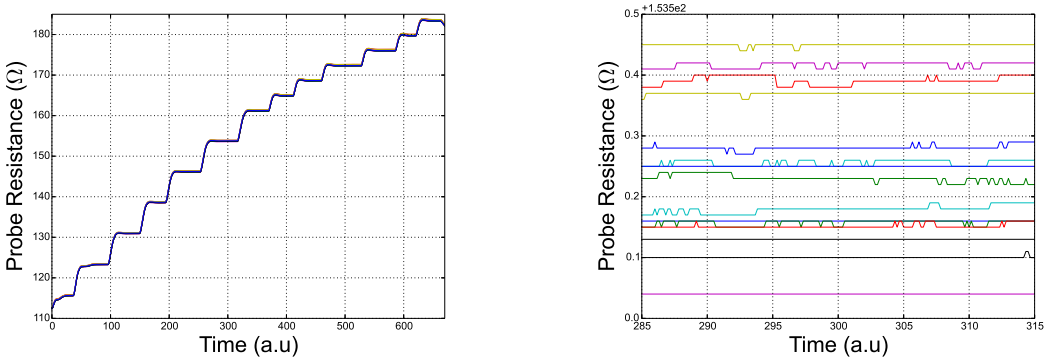

(a) Resistance vs time curve of probes (b) Equilibrium section at $T_{bath} = 100°C$.

Figure A.1: Resistance vs time curves of the Pt111 probes. Each plateau in resistance is the liquid bath reaching a stable temperature. Each curve of differing color represents a different probe.

temperature.

Most relative calibrations are done using some sort of polynomial fitting [21], in which a fit is made for the temperature of a probe with respect to its measured resistance at each temperature. Polynomial fits were applied for each probe which we number 0-14. We then have a probe's temperature as a function of its resistance, $T_p(R_p)$. We estimate the expected uncertainty for a single measurement of a probe by how far its temperature, $T_p(R_p)$, is from T_S, since we have a measured R_p for certain T_S (the plateau values in Figure A.1). An example residual plot is shown in Figure A.2 for $T_S = 180.494°C$ (corresponds to $T_{bath} = 180°C$), which is the range at which the oil will be tested.

We can see from Figure A.2 that probe #9 does not have a very good fit to within $\pm$ 0.05 K; and it turns out that it is not well calibrated for other temperatures as well. This will have to be taken into consideration when reading measurements from this probe. Otherwise, all other probes were relatively calibrated within $\pm$ 0.05 K of T_S for all temperatures used for calibration.

A.2 Silicone Oil Testing

Previous experiments were done on the 3m source with $T_{bath} = 180°C$ using Silicone Oil; in which temperatures were shown to stay within an interval of 0.2 K along the pipeline, which is within the allowed interval of 0.91 K at this temperature. Using these same parameters, the 3m source was tested again using Silicone, but this time

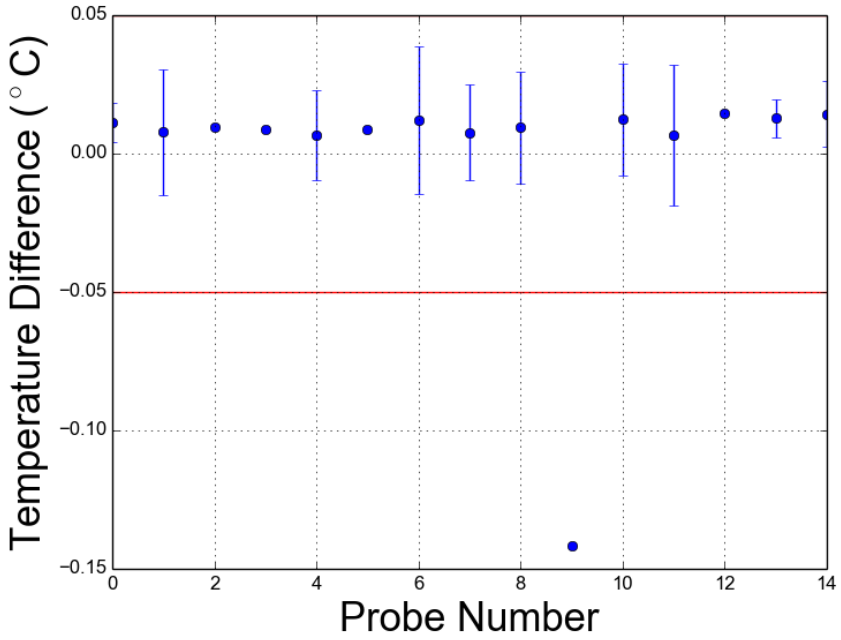

Figure A.2: Residual plot for each probe given by number 0-14 at $T_S = 180.494$°C or $T_{bath} = 180$°C. The error bars are standard deviations of temperature for each probe at equilibrium. Red lines are ± 0.05 K.

with the Pt111 probes to test their validity.

A.2.1 Experimental Setup

The 3m source was connected to the liquid bath via one hose to the inlet at one end, and one to the inlet at the other. With this setup, instead of having the oil flow from both sides and out the middle, the oil instead flows in to one side, and out the other. The experiment was set-up this way in order to test the worst case scenario in which there could be a larger heat loss from the oil traveling a greater distance.

We deemed an appropriate bath temperature to test as 180°C, since that is roughly in the middle of the temperature range we'd like (150 - 200 °C); and because it's the same temperature tested previously giving us a direct comparison to past experiments. This bath temperature corresponds to a 0.2% interval of 0.91 K.

Unfortunately, at high temperatures, Silicone Oil produces a bit of Formaldehyde, which is considered carcinogenic. As a result, the oil bath was covered in a plastic box, to decrease any risk of Formaldehyde exposure. Additionally, a large aluminum bellow with a fan inside was connected from a hole in the plastic box to a hole in the

room's window. This is to suction any fumes produced inside the box to the outside. A picture of this oil bath with the plastic box and bellow is shown in Figure A.3.

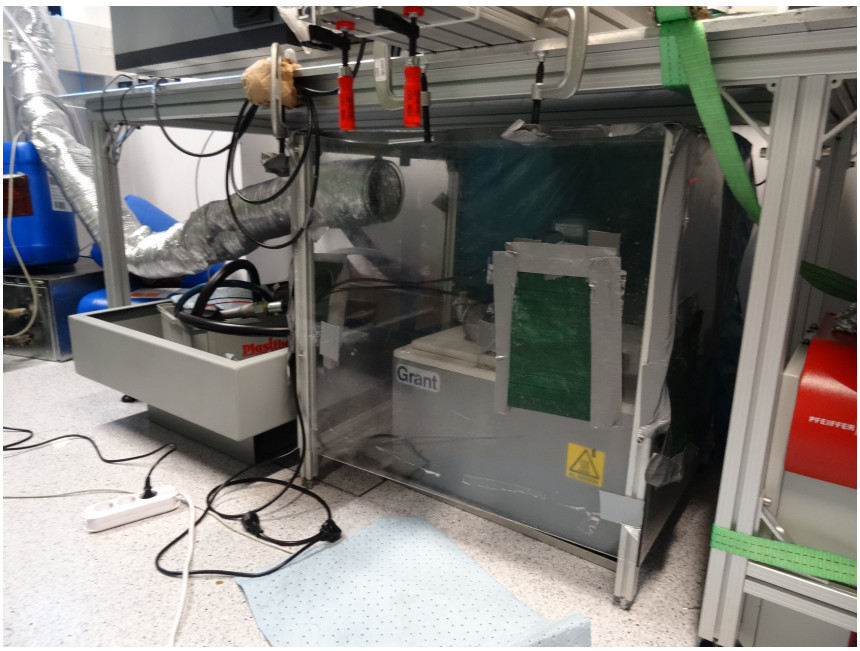

Figure A.3: Picture of oil bath covered with plastic box, and attached with aluminum bellow which suctions fumes to the outside.

The 3m source itself was mounted on an aluminum table, and oil bath was placed underneath this table. The 3m source was completely surrounded by rock wool insulation, and has a standard nipple bolted onto one end. The probes were taped along a thin, aluminum wire that could be pushed inside the pipe to make internal temperature measurements within the pipe. These probes were placed 18 cm apart so that we can measure a total distance of 252 cm within the pipe. A simplified drawing of the setup is shown in Figure A.5, as well as a sample picture (Figure A.4) of the 3m source with the probes already inside (and standard nipple not yet covered in insulation).

Looking at the Figure A.5, we see that probe position 0 cm is where the oil heating portion of the pipe begins; whereas positive probe positions are further inside along the direction of oil flow. Negative values of position in this case represent probes within the standard nipple bolted to the front end of the 3m source.

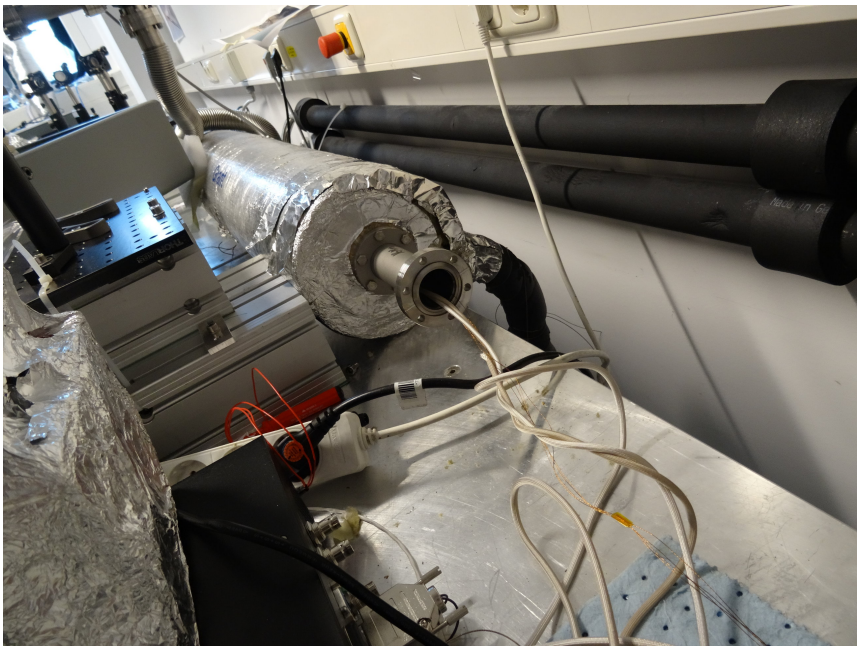

Figure A.4: Here we see the 3m heat exchanger covered with insulation, along with a bolted-on standard nipple. The probes were fed into it with the aluminum wire, and we see the probe wires coming out of the pipe.

A.2.2 Silicone Oil Results

The liquid oil bath temperature was raised to 180°C, and the liquid allowed to flow through the 3m source until the time-dependent temperatures of the probes remained stable, which took approximately 5-6 hours. Over a period of time in which the temperatures were deemed stable, the temperatures for each probe were averaged, and the standard deviation of temperature was also calculated. The mean temperatures for each probe are plotted as a function of probe position in Figure A.6, with the error bars being the standard deviation in temperature, σ_T. The results are also tabulated in Table A.1. It should be noted that the error in probe position was deemed to be about $\pm$ 0.5 cm, since the aluminum rod was put in by hand, and the distance between probes placed using a ruler. This remains true for all temperature experiments.

Looking at Figure A.6a and Table A.1, the temperature starts to drop off in the pipe while within the oil heated section. This shows the issue with maintaining temperature uniformity, as even with very good insulation there is still a large amount of heat loss through the ends of the system. From inside the heated section to within the standard nipple, there is a drop of about 42 K.

If we look at Figure A.6b, 30 cm within the heated section we start to see very

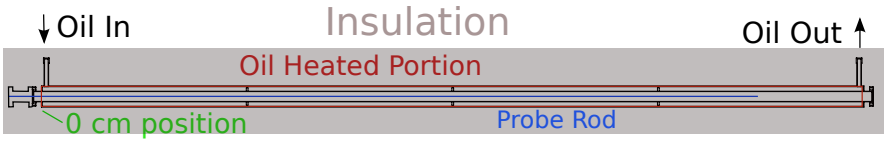

Figure A.5: Simplified drawing of the experiment. Everything was covered in rock-wool insulation, and the probe rod was placed inside the 3m source. The hot oil was inlet from one side and outlet the other. Also shown is the 0 cm point for probe position at the beginning of the oil heated section, with positive positions going into the 3m source.

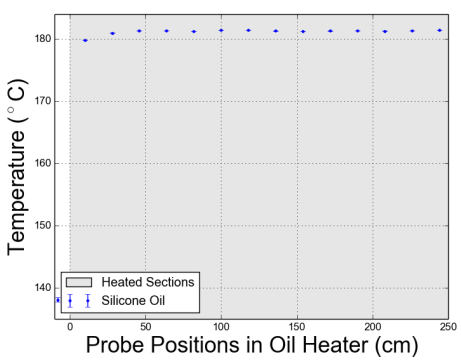

(a) Overall temperature profile

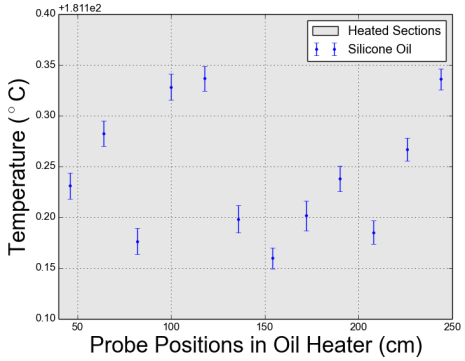

(b) Temperature profile within the uniform section

Figure A.6: Mean temperature and σ_T of each probe as a function of probe position within the oil heated portion of the 3m source. Grey shaded regions are regions of oil heating within the pipe.

uniform temperatures. The mean temperatures of the probes in this region are within 0.18 K, which is well within the required interval of 0.91 K. This is also comparable to the 0.2 K interval seen in previous experiments, showing that the probe measurements were reliable. It is also interesting to see that we don't see any clear gradient in temperature, which is also a result seen in previous experiments with Silicone Oil. Even at high pumping rates, one should see a small minor gradient (on the order of less than 1 K) if one were to assume perfectly laminar flow along the direction of the pipe. In the real world, the oil is also circulating radially around the pipe, causing a mixing of oil with slightly different temperatures. This mixing most likely is what eliminates the minor gradient, as the pipe is not long enough for there to be any significant longitudinal loss of heat comparable to the internal mixing of the oil.

Table A.1: Mean temperature measurements with their standard deviations as a function of probe position for Silicone Oil 3m source test.

Probe location (cm)	**Temperature (°C)**	σ_T
-8	138.1	0.4
10	179.83	0.01
28	180.98	0.01
46	181.33	0.01
64	181.38	0.01
82	181.28	0.01
100	181.43	0.01
118	181.44	0.01
136	181.30	0.01
154	181.26	0.01
172	181.30	0.01
190	181.34	0.01
208	181.29	0.01
226	181.37	0.01
244	181.44	0.01

A.3 Flipped Manifold Tests

Due to the flange extension of the manifold at the end, the heat loss is too significant to resolve the dip between the manifold and the 3m source. In order to see this dip, the manifold was flipped so that between the manifold and the 3m source, there is a flange-to-flange connection. This means there is less extension at the end of the manifold (the end where it is not connected), so the heat loss at the ends is reduced, while the heat loss between the manifold and 3m source heated sections is increased.

The setup is the same as in Figure 3.6, but with three main differences. First, the probes were re-soldered (in an attempt to fix the faulty probes), and then taped to the aluminum rod within a distance of 34 cm to get the temperature profile within the manifold and part-way into the 3m source. Even though it turns out that the probes are not calibrated to the precision intended, they were still deemed precise enough within orders of $\pm$ 0.1 K, so they could be used to resolve any dips that are seen. Also, the problematic probe #9 was put last (so within the 3m source), and was generally ignored.

Another difference is the 0 position was set to the beginning of the heated section

within the manifold. The final contrast is that the manifold itself was flipped, so it was attached to the 3m source via flange-to-flange connection. The results of the experiments are tabulated (see Table A.2) and plotted (see Figure A.7). Unfortunately, even with the probe re-soldering there were still faulty probes that had to be excluded from the results.

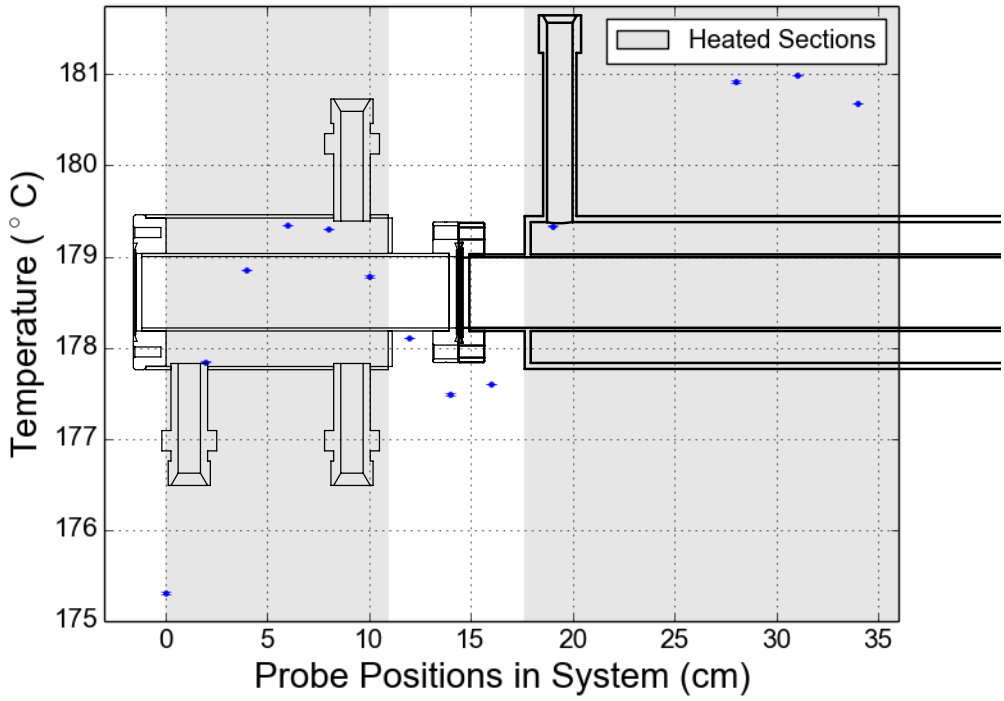

Figure A.7: Temperature profile as a function of probe position for flipped manifold attached to 3m source, run at $T_{bath} = 180°C$.

We see from Figure A.7 that by flipping the manifold, the heat loss from the end (through bolt-on portion and insulation) has been reduced with respect to the previous experiment; as the temperature drop is only about 6 K. This effect, combined with the increase in distance and material between the heated sections, creates a visible dip between the manifold and 3m source. Due to the aforementioned heat loss though, the temperature in the manifold (max. 179.34°C) does not reach the approximate temperature in the 3m source (about 181°C). The drop from the 3m source to the flange-connections is roughly -3.5 K, which is higher in magnitude than the calculated dip of -2.4 K. This is expected, as we still see there are dips in temperature within these heated sections; whereas calculations were done assuming

Table A.2: Temperature and standard deviations for each probe as a function of probe position for the flipped manifold experiment. Error bars are σ_T.

Probe location (cm ± 0.5)	**Temperature (°C)**	σ_T
0	175.31	0.01
2	177.85	0.003
4	178.85	7e-13
6	179.34	7e-13
8	179.31	5e-13
10	178.79	0.01
12	178.11	5e-13
14	177.49	0.01
16	177.60	9e-13
19	179.34	0.01
28	180.92	0.01
31	181.00	0
34	180.67	5e-13

the temperature in the heated sections was the same as the liquid temperature.

A.4 Heating Tape Power

We need to have enough power for each heating tape in Figure 3.11 to offset the heat loss in the disc and flange-to-flange connections. For the flange-to-flange connection, the power calculated for the dip (see Section A.5.2) was 0.824 W. So we can easily find heating tapes that can apply between 2-4 W of power maximum, and wrap it around one of the flanges.

For the disc, we estimate around 50 W (see Section A.5.3) in order to counter the heat loss through the disc. Past experience teaches us that this is an underestimate as we know there is additional heat loss through the insulation and near the Galden heated sections. We have a heating tape capable of providing 1250 W of power over 5m of tape, with width and thickness dimensions of 30 × 5 mm. So for 50 W, we would only need to wrap 0.2 m of this tape around the bolt-on portion of the manifold. This is assuming all the power would be directed against the flow of heat, but a lot of power will be radiated from the tape in the direction of the surrounding insulation. Also, the tape makes contact with the disk, and so there will also be an additional loss of heat through the disk as well. Furthermore, the heating tape itself has a layer

of insulating material, so after the first wrap of tape, the rest of the tape has to go through more insulating material in order to reach the disk and manifold bolt.

It is for this reason that we quadruple the amount of power needed to test whether the amount of tape is enough. In this case, we wrapped 0.8 m (200 W total) of heating tape around the manifold bolt. We connected the heating tape directly to the power outlet, and measured the voltage and current across the tape as well in order to monitor the power output. A Pt100 sensor, a larger type of platinum resistance probe, was placed between the tape and the disk (see Figure 3.11) in order to measure the temperature at this position. This temperature will be used for future PID control of the disc heating tape via a control probe. It should be noted that for this test, we did not have a heating tape on the flange-to-flange connection yet, as we also wanted to see how much the dip is affected by heating near the disc.

The Galden liquid was again run at bath temperature of 180°C, and other than the heating tape at the flange-to-flange connection (along with its control probe), the setup is the same as in Figure 3.11. The temperature profile is shown in Figure A.8, with the error bars represented by $\pm\sigma_T$.

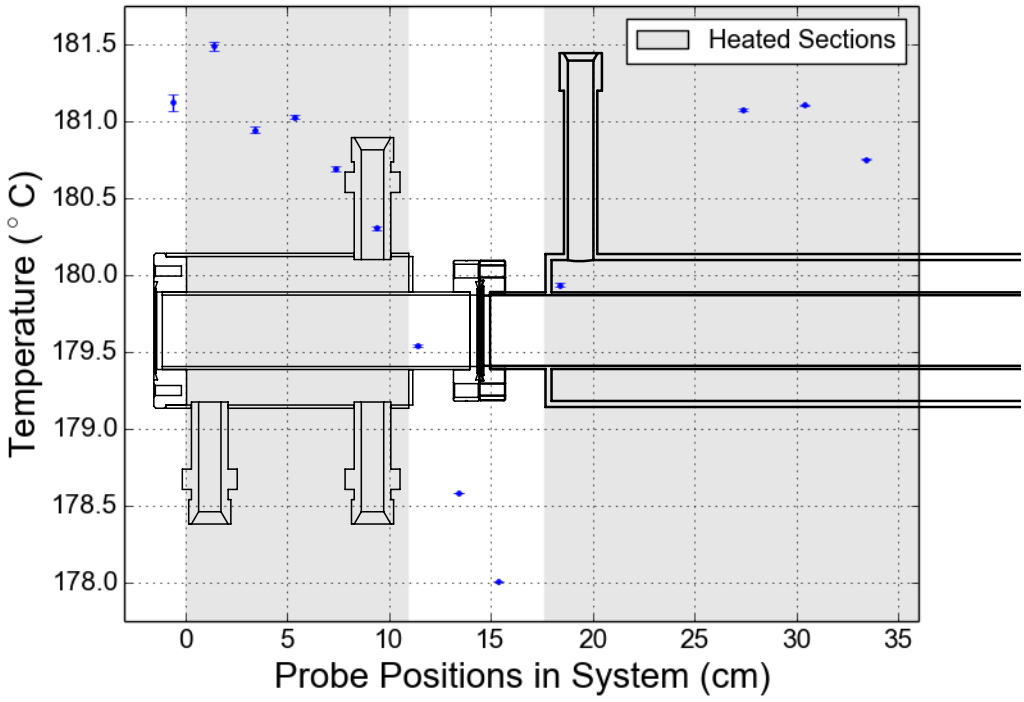

Figure A.8: Temperature profile vs position of probes for setup with Disc and 200W heating tape applied.

The total power of the heating tape applied was approximated by measuring the voltage and current across the tape a few times over a few minutes. The power applied to the system was 198 W with a standard deviation of 1 W. We see from looking at Figure A.8 that the heating tape outputted the appropriate amount of power, as the temperature within the manifold near the disc reaches a maximum of 181.5°C; whereas the maximum inside the 3m source is 181.11°C, a difference of only 0.39 K. This means that the overall heat loss through all components can be offset using additional electrical heating, as we have managed to prevent a drop in temperature at the end of the manifold. The temperature of the sensor between the tape and the disc measured 266°C, which is a reference for when PID control will be implemented.

A.5 Heat Transfer Calculations

A.5.1 Vapor Source Heat Exchanger Calculation using Galden

We can calculate the feasibility of the liquid circulation type of heater by gauging if the heat loss of the liquid along a 10m pipe would exceed the temperature requirement of 0.2%. We do this with a bit of help of "Heat Transfer" [23].

We first consider a cylindrical heat exchanger with liquid flowing cocentrically in the middle. The heat flow, Q, flows by convection to the inner wall of the cylinder, then radially by conduction through the cylindrical shell itself, and then to another fluid surrounding the cylinder (in this case air) through convection. A schematic of this system is shown in Figure A.9 [23] where T_i and T_o are the inside (liquid) and outside (air) temperatures respectively, h_i and h_o the respective heat transfer coefficients on the inside/outside, k the thermal conductivity of the material, r_i and r_o the inner/outer radius of the cylindrical material, and L the length of the material.

In this case, we assume the liquid is flowing through a concentric ring between the outer radius of the pipe ($r_{pipe} = 2$ cm) and the inner radius of cylindrical insulation ($r_i = 4$ cm). The cylindrical shell in this case represents the surrounding insulation. The liquid we use is Galden HT270, a proposed liquid to use for the heat exchanger. The parameters of this liquid can be found through its data sheet [24].

We first would like to find the transfer coefficient h_i between the galden and the insulation wall. We can estimate the mean transfer coefficient along the pipe of length L by assuming a strong enough flow rate which forces convection with laminar flow

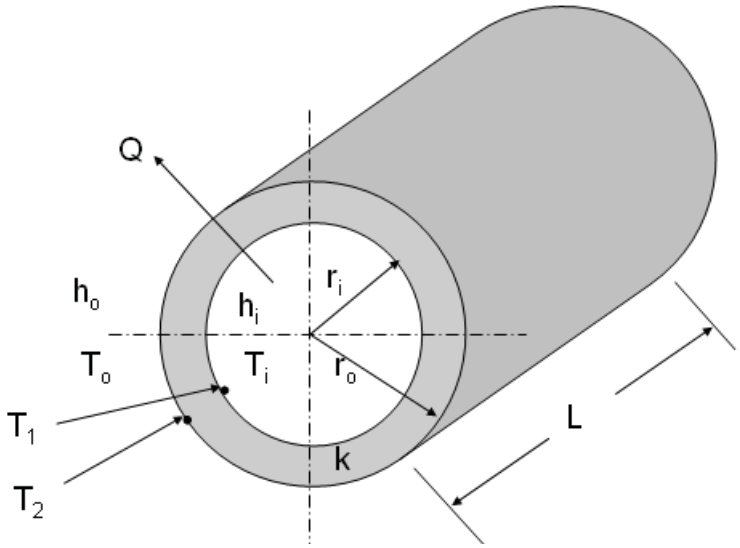

Figure A.9: Example of simple concentric heat exchanger. (from [23])

through the proper cross-sectional area of the ring of liquid, using the equation

$$h_L = 0.664 \frac{k}{L} Pr^{1/3} {Re_L}^{1/2} \tag{A.1}$$

where $Pr = \frac{\mu c_p}{k}$ and $Re_L = \frac{\rho u_\infty L}{\mu}$ are the dimensionless Prandtl and Reynolds numbers. They are calculated from the liquid parameters: viscosity μ, specific heat c_p, thermal conductivity k, density ρ, and initial flow velocity u_∞. The initial flow velocity is assumed to be about 50 liters/min, which is a readily available flow rate for liquid pumps. It should be made clear that the flow is through a cross sectional area of $\pi({r_i}^2 - {r_{pipe}}^2)$.

By inputting the proper parameters (from data sheet [24]) into the above equation, we find the heat transfer coefficient to be about 455230 $\frac{W}{m^2 K}$. We can estimate the heat transfer coefficient for the air outside the insulation, h_o, to be on the order of 10 $\frac{W}{m^2 K}$ based on typical values you might find in engineering databases online. It is also useful to know that the calculated Reynolds number is about 1.7×10^6 which is within the range of laminar flow; therefore the approximation of laminar flow should be quite good.

The total power lost over a length L for the simple system shown in Figure A.9

can be found through the equation

$$\frac{Q}{2\pi r_0 L} = \frac{(T_i - T_o)}{\left[\frac{r_o}{k_{ins}} ln(r_o/r_i) + \frac{r_o}{h_i r_i} + \frac{1}{h_o}\right]} = U_o(T_i - T_o) \tag{A.2}$$

with Q the power lost in units of watts, and U_o which is the overall heat transfer coefficient based on the outer area of the insulating tube with thermal conductivity $k_{ins} = 0.034\frac{W}{mK}$ (conductivity for wool insulation used at the lab at MPP). We assume an outer radius of about 10 cm for the insulation (r_o). An inner temperature of 180°C for the Galden is used since it is a middle temperature value for the rubidium source. The outer air temperature is set to 20°C, an approximate room temperature. Inputting the proper numbers, we find a total power loss of about 341 W through the insulation in the 10 m system.

We then calculate what this translates to in terms of longitudinal temperature loss of the liquid through the tube. We start with the typical equation for advection

$$Q = A_c u_\infty \rho c_p \Delta T \tag{A.3}$$

with A_c being the cross-sectional area of the liquid flow, and ΔT the difference in temperature at either end of the 10 m pipe. We know the heat loss is about 341 W at the steady-state equilibrium; when the inside of the pipe is in equilibrium and at the same temperature as the flowing liquid. So we use this to approximate ΔT which is calculated to be about 0.23 K. This is smaller than the required 0.91 K (0.2% of 180°C) range of temperatures.

Even if we halve the initial volumetric flow rate, change the inner temperature to 200°C and increase the h_o to $100\frac{W}{m^2K}$ we get $\Delta T \approx 0.5$ K; still within the set bounds of the experiment.

A.5.2 Manifold to 3m Source Flange-to-Flange connection Calculation

We can calculate the loss of heat for the flange-to-flange connection between the manifold and the 3 m source. For this case, we use two simplifying assumptions. We first assume that the Galden heated sections act as reservoirs of heat at 180°C. This should be a reasonable assumption due to the high mass flow of the liquid at 180°C, keeping the walls at the same temperature as the liquid. Another assumption is that

the air inside the inner pipe is completely stagnant, so there is not any convection and therefore at equilibrium, the air inside is at the same temperature as the pipe walls. The air of course will not be completely stagnant, but we assume that the system is closed off enough to prevent significant air convection within the pipe. A simple drawing of the flange-to-flange connection is shown in Figure A.10.

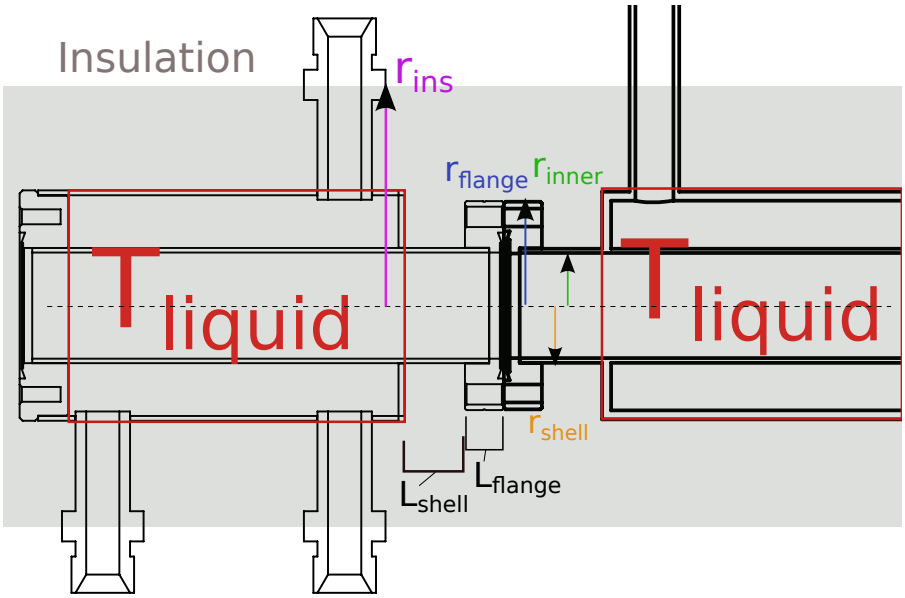

Figure A.10: Drawing of flange-to-flange connection between the manifold and heat exchanger. Shown are the respective radii and lengths used for the calculations. Note that due to symmetry, we assume the temperature dip from T_{liquid} to the flange connection is the same on either end.

We see from this drawing that the heat flow from each reservoir of temperature T_{liquid} to the flange-to-flange connection should be equal in this simple model due to symmetry. This means we can calculate the temperature loss from one reservoir to the flange-to-flange connection, then assume the temperature goes back up to T_{liquid} on the other side.

We say that at equilibrium, the pipe walls and flange lose heat radially through the surrounding insulation, and that this heat flow corresponds to the loss of heat longitudinally along the pipe's shell and flange. The heat loss from the inner side of the pipe shell to the outer insulation barrier is [23]

$$Q_r = \frac{2\pi L_{shell}(T_{inner} - T_{out})}{\frac{ln(r_{shell}/r_{inner})}{k_{steel}} + \frac{ln(r_{ins}/r_{shell})}{k_{ins}} + \frac{1}{r_{shell}h_{out}}} \tag{A.4}$$

where L_{shell} is the length of the pipe shell, T_{inner} the inner temperature of the pipe, T_{out} the temperature of the air outside the insulation, r_{shell} the outer radius of the pipe shell (where insulation starts), r_{ins} the outer radius of the insulation, r_{inner} the inner radius of the pipe, and k the thermal conductivity of the insulation (ins) and steel respectively.

It is important to note another assumption, which is that the overall temperature loss in the pipe is small enough that T_{inner} changes very little, so $T_{inner} - T_{out}$ remains roughly constant. We can then say the total power loss radially around the pipe shell driven by this temperature difference is equal to the loss of heat longitudinally along the z (beam propagation) axis of the steel pipe shell. We have for heat flow through pipe cross section area A_c:

$$\begin{aligned} Q_r = Q_z &= \frac{k_{steel} A_c (T_{liquid} - T_2)}{L} \\ Q_r &= \frac{k_{steel} \pi (r_{shell}^2 - r_{inner}^2)(T_{liquid} - T_2)}{L_{shell}} \\ \rightarrow T_2 &= T_{liquid} - \frac{Q_r L_{shell}}{k_{steel} \pi (r_{shell}^2 - r_{inner}^2)} \end{aligned}$$

where T_2 is the temperature a distance L_{shell} from the edge of the T_{liquid} reservoir along the z axis.

So we can find the loss of heat ΔT from the heated section at T_{liquid} to T_2 after length L_{shell} for the pipe shell component. Now we can do the same calculation for the flange component, replacing L_{shell} with L_{flange}, r_{shell} with r_{flange}, and the temperature drop now goes from T_2 to some arbitrary T_3 at the flange connections.

The temperature loss across the shell for $T_{liquid} = 180°$C is - 2.27 K, whereas across the flange is 0.13 K. The combined temperature loss across the shell and flange is ΔT = -2.40 K. The dip in temperature corresponds to a total power loss of 0.824 W from the liquid heated sections to the flange-to-flange connection.

A.5.3 Disc Calculation with Bolt

We can make a calculation of heat flow (in Watts) out of the disc by making simplifying assumptions. The first is that since heat transfer problems are boundary value problems, we need to know the set temperature at either end of the heat flow; therefore, we assume the temperature of the Galden heated sections and the room

temperature to be constant. The second is that compared to the heat flow through stainless steel, the heat loss through the insulation is very small since $\frac{k_{steel}}{k_{ins}} \approx 441$, so there is much less 'resistance' to heat flow through the steel. This means we ignore the heat flow through insulation and make a model where the heat flows purely through steel components. The third is that the air in the pipe is stagnant, and it also has a thermal conductivity of 0.024 $\frac{W}{mK}$, which makes it act like thermal insulation. So we ignore heat flow through the air in the pipe as well, and also assume anyway that at equilibrium, the temperature of the air is equal to the temperature of the inner walls of the pipe.

We have a simple drawing of the system in Figure A.11. Here we see the flow of heat from T_{liquid} in the manifold all the way to the outside air at temperature T_{out}. From this drawing, we can make a simple 1D model to get the temperature profile of the system. For reference, the radius from the center of the pipe to the manifold-insulation boundary is r_{bolt}, and the radius to the insulation-air boundary is r_{ins}.

We first need to know the general equations for the temperature as a function of radius in the disc. In the portion of the disc with heat flow Q_r, the general equation for temperature is [23]:

$$T(r_{bolt} \leq r \leq r_{ins}) = \frac{ln(r/r_{bolt})}{ln(r_{ins}/r_{bolt})}(T_{ins} - T_{bolt}) + T_{bolt} \tag{A.5}$$

where T_{ins} is the temperature of the disc at r_{ins}, and T_{bolt} is the temperature of the disc at r_{bolt}.

We also need to solve the temperature equation for the part of the disc that has one side exposed to air. In this case, we have a continuous loss of heat as the heat flows to the end of the disc. Let's consider a portion of the exposed disk, where we have the radial heat flow at some r is Q_r, and the heat flow after some $r+\delta r$ is $Q_{r+\delta r}$. The heat flow at radius r for the disc with thickness l is:

$$Q_r = -kA_c\frac{dT}{dr} = -k2\pi rl\frac{dT}{dr} \tag{A.6}$$

The heat flow for $r + \delta r$ is therefore

$$Q_{r+\delta r} \approx Q_r + \frac{dQ_r}{dr}\delta r = Q_r + \frac{d}{dr}(-k2\pi rl\frac{dT}{dr})\delta r$$

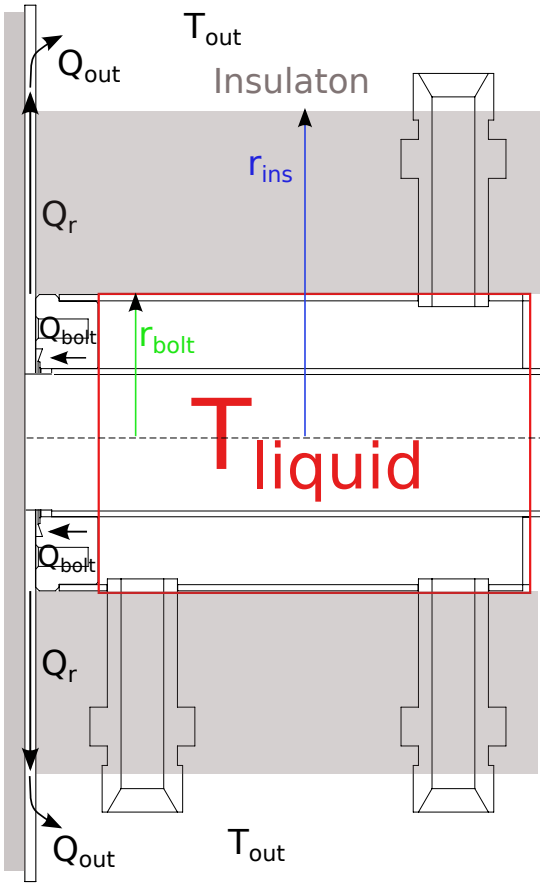

Figure A.11: Drawing of manifold and disc connection. Shown is the direction of the heat flow; starting from the liquid Galden, through the bolt connection to the disc, radially through the disc, and then with convection to the air. Also shown are the important radii needed for calculations.

We also know that the heat flow is lost by convection over some area δA_s, which is

the surface area of the ring in the disc between r and $r + \delta r$. So we have

$$\begin{aligned}
Q_r &= Q_{r+\delta r} + h_{out}\delta A_s(T - T_{out}) \\
\rightarrow Q_r &= Q_r + \frac{d}{dr}(-k2\pi rl\frac{dT}{dr})\delta r + h_{out}\delta A_s(T - T_{out}) \\
\rightarrow 0 &= -k2\pi l\left(\frac{d^2T}{dr^2}r + \frac{dT}{dr}\right)\delta r + h_{out}\delta A_s(T - T_{out}) \text{ divide by } \delta r \\
\rightarrow 0 &= -k2\pi l\left(\frac{d^2T}{dr^2}r + \frac{dT}{dr}\right) + h_{out}\frac{\delta A_s}{\delta r}(T - T_{out}) \text{ with } \delta A_s = 2\pi r\delta r \\
\rightarrow 0 &= -k2\pi l\left(\frac{d^2T}{dr^2}r + \frac{dT}{dr}\right) + h_{out}2\pi r(T - T_{out}) \\
\rightarrow 0 &= \frac{d^2T}{dr^2} + \frac{1}{r}\frac{dT}{dr} - \frac{h_{out}}{kl}(T - T_{out})
\end{aligned}$$

where the subscript *out* is for the surrounding air temperature.

The solution to the above differential equation is a linear combination of modified bessel functions of the 0^{th} order:

$$T(r_{ins} \leq r \leq r_{disc}) = c_1 I_0(\sqrt{\frac{h_{out}}{kl}}r) + c_2 K_0(\sqrt{\frac{h_{out}}{kl}}r) + T_{out} \tag{A.7}$$

where I_0 and K_0 are the modified 0^{th} order bessel functions of the first and second kind respectively, and r_{disc} is the radius of the disc.

It will be important to know afterwards that $\frac{dT}{dr}$ of this equation is then:

$$\frac{dT(r_{ins} \leq r \leq r_{disc})}{dr} = c_1\sqrt{\frac{h_{out}}{kl}}I_1(\sqrt{\frac{h_{out}}{kl}}r) - c_2\sqrt{\frac{h_{out}}{kl}}K_1(\sqrt{\frac{h_{out}}{kl}}r) \tag{A.8}$$

where I_1 and K_1 are the modified 1^{st} order bessel functions of the first and second kind respectively.

We first set equal the heat flow from the bolt to the disc, where A_{bolt} and L_{bolt} is the cross-sectional area and length of the manifold bolt.

$$\begin{aligned}
Q_{bolt} &= Q_r \\
-kA_{bolt}\frac{dT}{dx} &= -kA_r\frac{dT}{dr} \\
\frac{-kA_{bolt}(T_{bolt} - T_{liquid})}{L_{bolt}} &= \frac{-2\pi lk(T_{ins} - T_{bolt})}{ln(r_{ins}/r_{bolt})}
\end{aligned}$$

and so we end up with

$$\frac{A_{bolt}T_{liquid}}{L_{bolt}} = \left[\frac{2\pi l}{ln(r_{ins}/r_{bolt})} + \frac{A_{bolt}}{L_{bolt}}\right]T_{bolt} - \left[\frac{2\pi l}{ln(r_{ins}/r_{bolt})}\right]T_{ins} \tag{A.9}$$

We also have the radial heat flow from the disc, Q_r, and the initial heat flow from the disc when exposed to air, $Q_{out}(r_{ins})$, be equal to conserve heat flow.

$$\begin{aligned} Q_r &= Q_{out}(r_{ins}) \\ -kA_r\frac{dT}{dr} &= -kA_r\frac{dT_{ins}}{dr} \\ \frac{-2\pi lk(T_{ins}-T_{bolt})}{ln(r_{ins}/r_{bolt})} &= -2\pi klr_{ins}\left[c_1\sqrt{\frac{h_{out}}{kl}}I_1(\sqrt{\frac{h_{out}}{kl}}r_{ins}) - c_2\sqrt{\frac{h_{out}}{kl}}K_1(\sqrt{\frac{h_{out}}{kl}}r_{ins})\right] \end{aligned}$$

We rearrange the equation and get

$$0 = c_1\left[\sqrt{\frac{h_{out}}{kl}}I_1(\sqrt{\frac{h_{out}}{kl}}r_{ins})\right] - c_2\left[\sqrt{\frac{h_{out}}{kl}}K_1(\sqrt{\frac{h_{out}}{kl}}r_{ins})\right] + \left[\frac{1}{r_{ins}ln(r_{ins}/r_{bolt})}\right]T_{bolt} - \left[\frac{1}{r_{ins}ln(r_{ins}/r_{bolt})}\right]T_{ins} \tag{A.10}$$

We know that the temperature at r_{ins} on the disc is T_{ins} so input these into equation A.7

$$-T_{out} = c_1\left[I_0(\sqrt{\frac{h_{out}}{kl}}r_{ins})\right] + c_2\left[K_0(\sqrt{\frac{h_{out}}{kl}}r_{ins})\right] - T_{ins} \tag{A.11}$$

Also, the temperature at r_{disc} is what we call T_{end}, so also inputting into equation A.7 get

$$-T_{out} = c_1\left[I_0(\sqrt{\frac{h_{out}}{kl}}r_{disc})\right] + c_2\left[K_0(\sqrt{\frac{h_{out}}{kl}}r_{disc})\right] - T_{end} \tag{A.12}$$

Finally, we have a constant heat flow at the end of the disc. This heat flow is $Q_{out}(r_{disc})$, or Q_{out} evaluated at the very end of the disc. This is the same as the loss of heat due to air convection on the outer surface of the disc which we call Q_{end}. We call the outer surface area of the disc A_{end} and the temperature at the end T_{end}. So

we have:

$$Q_{out}(r_{disc}) = Q_{end}$$

$$-kA_{end}\left[c_1\sqrt{\frac{h_{out}}{kl}}I_1(\sqrt{\frac{h_{out}}{kl}}r_{disc}) - c_2\sqrt{\frac{h_{out}}{kl}}K_1(\sqrt{\frac{h_{out}}{kl}}r_{disc})\right] = h_{out}A_{end}(T_{end} - T_{out})$$

which becomes

$$-h_{out}T_{out} = -c_1\left[\sqrt{\frac{h_{out}}{kl}}I_1(\sqrt{\frac{h_{out}}{kl}}r_{disc})\right] + c_2\left[\sqrt{\frac{h_{out}}{kl}}K_1(\sqrt{\frac{h_{out}}{kl}}r_{disc})\right] - h_{out}T_{end} \tag{A.13}$$

We have five equations (A.9, A.10, A.11, A.12, and A.13) with five unknowns (c_1, c_2, T_{bolt}, T_{ins}, and T_{end}). We set the temperature of $T_{liquid} = 180°$C and the temperature outside $T_{out} = 20°$C. We take the air convection heat transfer coefficient to be 10 $\frac{W}{m^2K}$, which is a generally used transfer coefficient for free air convection [23]. We can solve this system of equations, and we end up with:

$$\begin{pmatrix} c_1 \\ c_2 \\ T_{bolt} \\ T_{ins} \\ T_{end} \end{pmatrix} = \begin{pmatrix} 0.967 \\ 169.931 \\ 166.566°C \\ 78.910°C \\ 36.054°C \end{pmatrix} \tag{A.14}$$

So we find that the temperature at the end of the manifold bolt will be around 167°C, and the heat flow out through the disk, Q_r is 42.8 W. This would be the power required to counteract the heat flow from the disc, and therefore keep the temperature within the pipe uniform until the end.

If we take the more extreme case, with $h_{out} = 100\frac{W}{m^2K}$ and the room temperature $T_{out} = 15°C$, then we get the temperature at the pipe end to be 161.995°C and the power loss through the disc is 57.375 W.

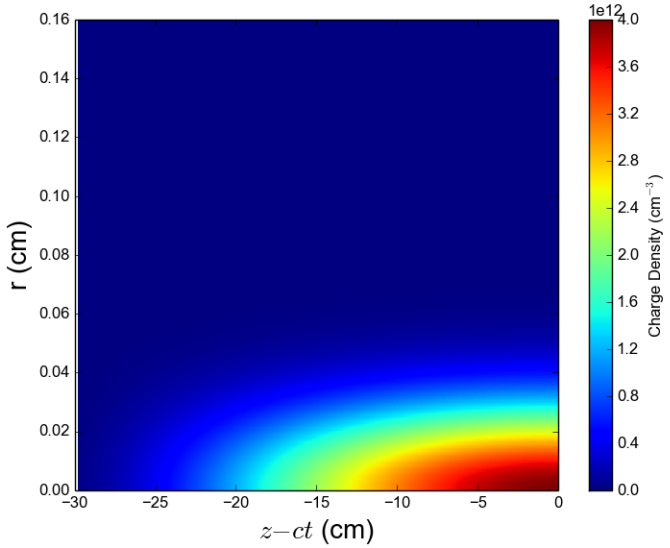

Figure A.12: Density profile of initial proton bunch before entering the plasma.

A.6 Additional OSIRIS Results

A.6.1 Initial Parameters Check

In order to check and debug any issues with the OSIRIS simulation, we look over a couple of results for an initial run, and compare to expected results. The initial proton bunch is shown in Figure A.12 within the full simulation window, which is about 30 cm in the z direction, and 0.16 cm in the radial direction. This window, and consequently mesh grid, is what moves through the plasma. The initial proton bunch is set to the parameters of Table 4.1.

As explained in chapter 2, the proton bunch should create micro-bunches along the axis (near r = 0) as its wakefield modulates the longitudinal bunch density. To show this is the case, we present the log of the proton bunch density at various propagation distances in the plasma (Figure A.13). We see from the following figure that protons are focused into micro-bunches about λ_p apart, while protons between these bunches are expelled transversely. This is the result of SMI development.

As these micro-bunches form, they start to resonantly drive the wakefield, creating larger amplitudes as it propagates through the first part of the plasma. The wakefields generated in OSIRIS are generally noisy along the axis, and so to smooth out these fields, they are averaged over a range in r. The best way to get smooth wakefields is by averaging up to r $\approx$ 0.2 mm, which is on the order of the skin depth k_p. We can see an

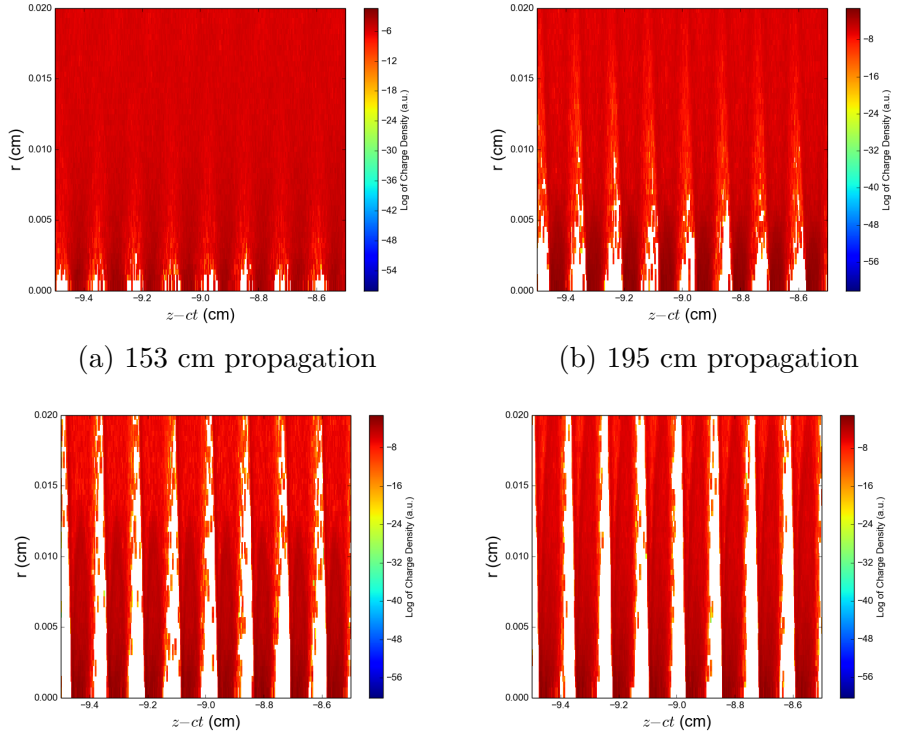

(a) 153 cm propagation

(b) 195 cm propagation

(c) 238 cm propagation

(d) 280 cm propagation

Figure A.13: Proton bunching at $z - ct$ = -9 cm over different propagation distances in the plasma.

example of the respective wakefields around $z - ct$ = -9 cm for the same propagation distances as in Figure A.12. This is shown in Figure A.14. The longitudinal wakefields (E_z) and transverse wakefields ($E_r - B_\theta$) are in units of GV/m.

We show in Figure A.15 the longitudinal and transverse wakefields after 10 m of propagation through the plasma. We see that in general, $|E_z|$ peaks in the region of $\xi = \sigma_{zb}$.

A.6.2 Phase Fits

We can compare the results of the fit $E_z = A\cos(k_p\xi + \phi)$, with one fit varying λ_p and the other keeping it as the theoretical constant. An example of the two fits applied to E_z, as well as the total phase shift using both fits at ξ = -12 cm, is shown in Figure A.16. The phase plots for both methods (Figure A.16b) are within 0.01 radians of each other; and so for our purposes, they are identical.

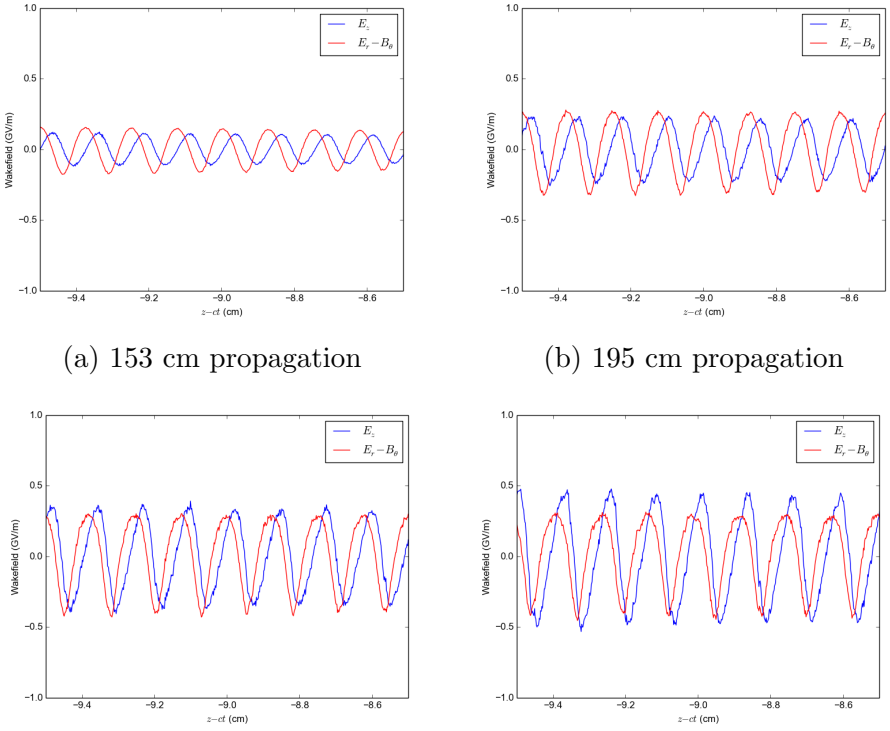

(a) 153 cm propagation

(b) 195 cm propagation

(c) 238 cm propagation

(d) 280 cm propagation

Figure A.14: Plasma wakefields at $z - ct$ = -9 cm over different propagation distances in the plasma.

A.6.3 Phase Spikes

To show that the phase spikes seen as a function of proton propagation are not a product of the fitting routine, we show E_z (not normalized) at ξ = -4 cm (where the waveforms are more sinusoidal and so easier to visualize) for various file dumps. Figure A.17 shows the phase change at file numbers 73 and 53 in a 99 dump simulation. We see that there is a clear back-shift of the waveforms in ξ at file 53 and 73. This remains true for other such files, so the fitting routine is not the issue; these phase spikes likely come from some numerical error within the simulation.

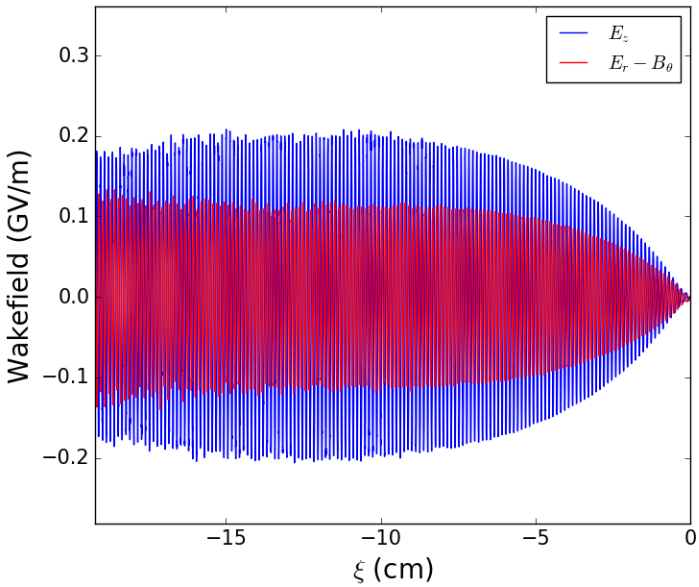

Figure A.15: Longitudinal (E_z) and transverse ($E_r - B_\theta$) wakefields along the bunch after 10 m of propagation.

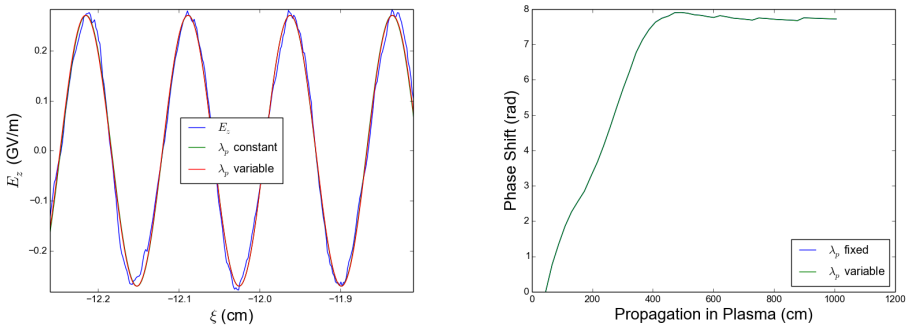

(a) Example fit to E_z (b) Phase shift derived from both fits

Figure A.16: Figures showing comparison between cosine phase fitting with λ_p constant and varying. Both done on initial parameters simulation.

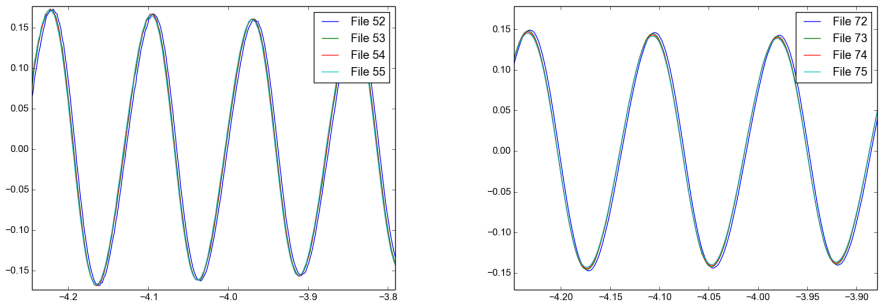

(a) From file 52 to 54 (b) From file 72 to 74

Figure A.17: E_z (non-normalized) for consecutive file dumps showing the phase spike, or back-shift in ξ, of E_z

A.7 Temperature Experiments Additional Tables and Figures

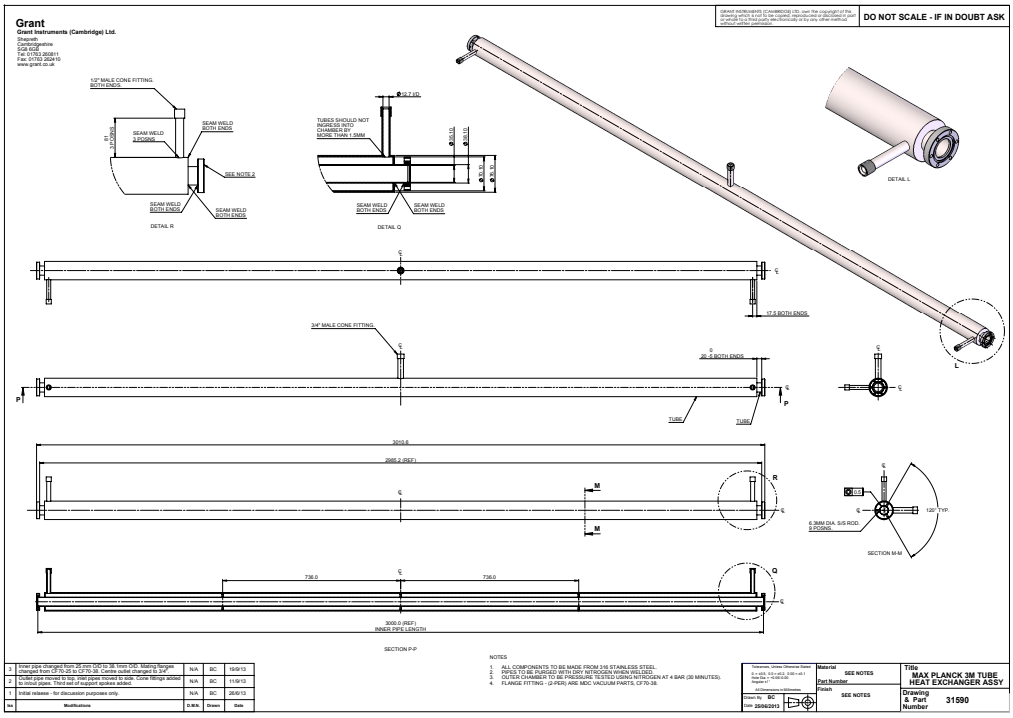

Figure A.18: General design schematic of the 3m heat exchanger (3m source).

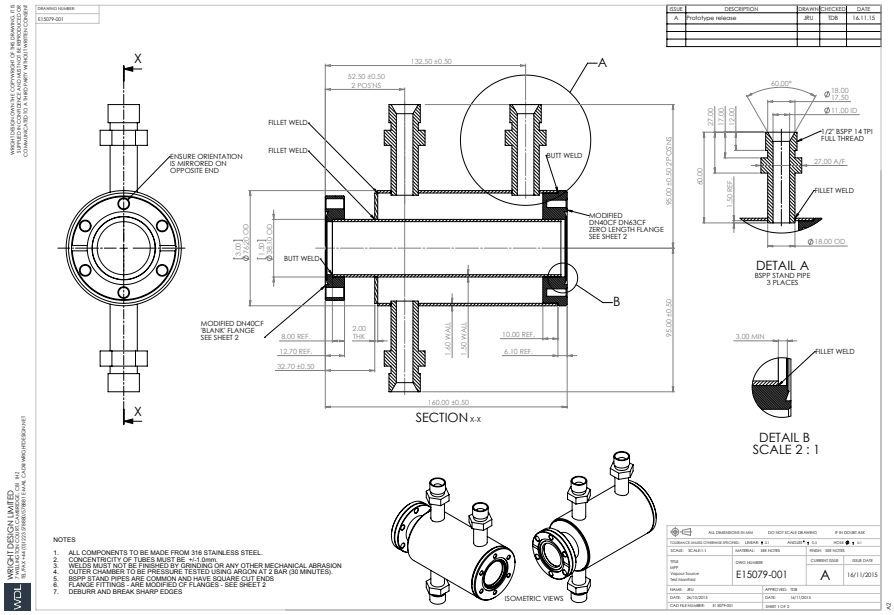

Figure A.19: Design schematic of manifold used for testing.

Table A.3: Temperature and standard deviations for each probe as a function of probe position, for 3m source tests with Galden HT270.

Probe location (cm)	**Temperature (°C)**	σ_T
-17	85.0	0.7
-8	117	2
1	164.7	0.2
10	178.00	0.09
19	180.08	0.01
28	180.44	0.01
37	180.87	0.01
46	180.88	0.01
55	180.93	0.02
64	180.91	0.01
73	180.84	0.01
82	180.81	0.01
91	180.97	0.01
100	180.93	0.01
109	180.96	0.02
118	180.92	0.01
127	181.03	0.01
136	181.00	0.01
145	180.53	0.01
154	180.49	0.006
181	180.84	0.01
190	180.79	0.01
208	180.71	0.01
217	180.82	0.01
226	180.76	0.01
235	180.77	0.01
244	180.72	0.01

Bibliography

[1] S.V. Kuzikov *et al.* Concepts for raising rf breakdown threshold by using multi-moded cavities. *Proceedings of RuPAC-2010, year=2010,*.

[2] E. Esarey, P. Sprangle, J. Krall, and A. Ting. Overview of plasma-based accelerator concepts. *IEEE Transactions on Plasma Science*, 24(2):252–288, Apr 1996.

[3] I. Blumenfeld *et al.* Energy doubling of 42 gev electrons in a metre-scale plasma wakefield accelerator. *Nature*, 445(7129):741–744, Feb 2007.

[4] A. Caldwell, K. Lotov, A. Pukhov, and F. Simon. Proton-driven plasma-wakefield acceleration. *Nat Phys*, 5(5):363–367, May 2009.

[5] Y. Fang. *Resonant Excitation of Plasma Wakefield*. PhD thesis, University Of Southern California, December 2013.

[6] A.I. Akheizer and R.V Polovin. Theory of wave motion of an electron plasma. *JETP*, 3(5):696, November 1956.

[7] W. Lu, C. Huang, M. M. Zhou, W. B. Mori, and T. Katsouleas. Limits of linear plasma wakefield theory for electron or positron beams. *Physics of Plasmas*, 12(6), 2005.

[8] J.J. Su *et al.* Stability of the driving bunch in the plasma wakefield accelerator. *IEEE Transactions on Plasma Science*, 15(2):192–198, April 1987.

[9] K. V. Lotov. Physics of beam self-modulation in plasma wakefield accelerators. 2015.

[10] J. Krall and G. Joyce. Transverse equilibrium and stability of the primary beam in the plasma wakefield accelerator. *Physics of Plasmas*, 2(4):1326–1331, 1995.

[11] A. Caldwell *el al.* Path to awake: Evolution of the concept. *Nuclear Instruments and Methods in Physics Research Section A: Accelerators, Spectrometers, Detectors and Associated Equipment*, 2016.

[12] K. V. Lotov. Simulation of proton driven plasma wakefield acceleration. *Phys. Rev. ST Accel. Beams*, 13:041301, Apr 2010.

[13] K. V. Lotov, A. Pukhov, and A. Caldwell. Effect of plasma inhomogeneity on plasma wakefield acceleration driven by long bunches. *Physics of Plasmas*, 20(1), 2013.

[14] Rubidium. NIST, 2016. http://webbook.nist.gov/cgi/inchi/InChI%3D1S/Rb.

[15] E. Oz and P. Muggli. A novel rb vapor plasma source for plasma wakefield accelerators. *Nuclear Instruments and Methods in Physics Research Section A: Accelerators, Spectrometers, Detectors and Associated Equipment*, 740:197 – 202, 2014. Proceedings of the first European Advanced Accelerator Concepts Workshop 2013.

[16] Bureau International des Poids et Mesures Sevres, The address of the publisher. *Techniques for Approximating the International Temperature Scale of 1990*, 1 edition, 1990. An optional note.

[17] E. Kindel and F. Adler. The hook method- interferometric diagnostics of gas discharges.

[18] K. V. Lotov, A. P. Sosedkin, A. V. Petrenko, L. D. Amorim, J. Vieira, R. A. Fonseca, L. O. Silva, E. Gschwendtner, and P. Muggli. Electron trapping and acceleration by the plasma wakefield of a self-modulating proton beam. *Physics of Plasmas*, 21(12), 2014.

[19] G. D. Danilatos. Direct simulation monte carlo study of orifice flow. *AIP Conference Proceedings*, 585(1):924–932, 2001.

[20] R. Fonseca. *PIC Simulation of Plasmas*. PhD thesis, DCTI/Lisbon University Institute, May 2005.

[21] Omega. *PT-100 Series*, May 2014. An optional note.

[22] Lake Shore Cryotronics, Inc., 575 McCorkle Blvd. Westerville, Ohio 43082-8888 USA. *User's Manual Model 218 Temperature Monitor*, 2 edition.

[23] Chris Long and Naser Sayma. *Heat Transfer*. Ventus Publishing ApS, 2009.

[24] Solvay, Viale Lombardia, 20 20021 Bollate (MI), Italy. *Galden HT PFPE Heat Transfer Fluids*, 2 edition.